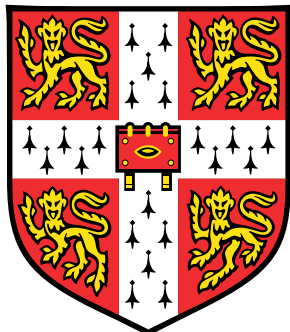


Exciton interactions in lead iodide perovskites



Wendy Niu

Department of Physics
University of Cambridge

This dissertation is submitted for the degree of

Doctor of Philosophy

Robinson College

2014

I would like to dedicate this thesis to my loving parents ...

Declaration

I hereby declare that except where specific reference is made to the work of others, the contents of this dissertation are original and have not been submitted in whole or in part for consideration for any other degree or qualification in this, or any other University. This dissertation is the result of my own work and includes nothing which is the outcome of work done in collaboration, except where specifically indicated in the text. This dissertation contains less than 65,000 words including appendices, bibliography, footnotes, tables and equations and has less than 150 figures.

Wendy Niu
2014

Acknowledgements

And I would like to acknowledge ...

Abstract

This is where you write your abstract ...

Contents

Contents	xi
List of Figures	xv
Nomenclature	xxv
1 Introduction	1
2 Excitons in lead iodide perovskites	5
2.1 Properties of excitons	5
2.2 Excitons in 2D systems	9
2.3 Properties of PbI perovskites	11
2.3.1 Structure and bonding	11
2.3.2 Fabrication and processing techniques	14
2.3.3 Electronic structure	21
2.3.4 Optical properties	23
2.3.5 Influence of organic molecules	28
2.3.6 Applications	30
2.4 Conclusions	35
3 Plasmonic nanostructures	37
3.1 Introduction	37
3.2 Surface plasmon polaritons	37
3.3 Plasmonic gratings	40
3.3.1 First order modes	41
3.3.2 Grating anomalies	42
3.3.3 Localised and guided modes	44
3.4 Localised surface plasmons	45

3.4.1	Quasi-static approximation	45
3.4.2	Size and shape effects	48
3.5	Conclusions	49
4	Thin films of lead iodide perovskites	51
4.1	Introduction	51
4.2	Spin coating theory	51
4.3	Experimental methods	53
4.4	$C_{12}PI$ thin films	54
4.4.1	Spin speed	55
4.4.2	Substrate preparation	55
4.4.3	Sample degradation	56
4.5	CHPI thin films	56
4.5.1	Spin speed	56
4.5.2	Substrate preparation	57
4.5.3	Humidity	61
4.6	Conclusions	61
5	Micromechanical exfoliation of lead iodide perovskites	63
5.1	Introduction	63
5.2	Experimental methods	63
5.3	Exfoliated CHPI samples	64
5.4	Conclusions	70
6	Perovskite-coated metal islands	71
6.1	Introduction	71
6.2	Metal island films	71
6.2.1	Experimental methods	72
6.2.2	Au metal island films	72
6.2.3	CHPI-coated Au metal island films	73
6.2.4	Ag metal island films	73
6.2.5	CHPI-coated Ag metal island films	76
6.2.6	Ag islands on CHPI films	78
6.3	Nanosphere lithography	79
6.3.1	Experimental methods	80
6.3.2	Au islands	80

6.3.3	CHPI-coated Au islands	81
6.4	Conclusions	82
7	Perovskite-coated gratings	85
7.1	Introduction	85
7.2	Experimental methods	85
7.3	Dielectric gratings	86
7.3.1	ETFE gratings	86
7.3.2	CHPI-coated ETFE gratings	88
7.4	Non-plasmonic metal gratings	89
7.4.1	Ti gratings	89
7.4.2	CHPI-coated Ti gratings	89
7.5	Plasmonic metal gratings	91
7.5.1	Ag gratings	91
7.5.2	PS-coated Ag gratings	96
7.5.3	CHPI-coated Ag gratings	98
7.6	Conclusions	105
8	Conclusions and further work	107
References		111

List of Figures

1.1	(a) Replica of first transistor built in 1946. Reproduced from Ref. [8]. (b) Schematic of process required to produce device-grade silicon from starting materials. Reproduced from Ref. [9].	2
1.2	(a) Common organic semiconductors, with p-type materials on the left and n-type on the right. Modified from Ref. [12]. (b) Samsung curved smart OLED TV. Reproduced from Ref. [13].	3
2.1	(a) (Left) Band structure of a semiconductor, showing the single-particle representation of the excitation of an electron-hole pair via photon absorption. (Right) Two-particle representation of the same system, illustrating exciton energy levels below the CB. (b) Theoretical absorption spectrum of a 3D semiconductor according to Eq. 2.4 (not to scale). The dotted line shows the expected band edge absorption without the Sommerfeld factor (see text). (c) Experimental absorption spectrum of GaAs crystal at 1.7 K, with the labelled laser power (W/cm ²). From Ref. [14].	7
2.2	(a) Schematic of quantum well band alignments. (b) Allowed transitions for electrons in a quantum well (left) and the resultant miniband structure (right). (c) Theoretical absorption spectrum of a 2D quantum well according to Eq. 2.4 (black lines). The dotted grey line shows the band edge absorption in 3D, the dashed red line the absorption in 2D, both without the Sommerfeld factor. (d) Experimental absorption spectrum of GaAs/Al _{0.2} Ga _{0.2} As quantum wells with the labelled well width L at 2 K. Only the $n = 1$ excitons are observed, but the minibands u are labelled. Adapted from Ref. [17].	10
2.3	(a) Structure of ABX ₃ perovskite. Adapted from Ref. [32]. Structure of (b) 3D perovskite (CH ₃ NH ₃)PbI ₃ , (c) 2D perovskite (RNH ₃) ₂ PbI ₄ , (d) 2D multilayered perovskite (RNH ₃) ₂ (CH ₃ NH ₃)Pb ₂ I ₇ , and (e) 2D diammonium perovskite (H ₃ NRNH ₃)PbI ₄ viewed along the crystallographic \vec{b} axis.	12

2.4 (a) Schematic of Langmuir-Blodgett setup, with (A) a bath containing (B) the monolayer of amphiphilic molecules at the gas-fluid interface, (C) the substrates being withdrawn from the bath, and (D) a balance that measures the surface pressure of the monolayer, generated by the movable barrier. (E) The moving barrier is controlled by a feedback device (F), which gets information from the pressure sensor and adjusts the barrier position using the (G) motor. (b) Absorption spectra of LB film obtained using the labelled number of depositions, and exciton absorbance intensity against the number of depositions (inset). (a) reproduced from Ref. [45], and (b) reproduced from Ref. [52].	16
2.5 Molecular dynamics for the liquid-phase intercalation of organic ammonium iodide molecules into PbI_2 film. Reproduced from Ref. [57].	17
2.6 (a) Schematic of dual-source vacuum deposition process. (b) Absorbance spectra of a vacuum deposited film, a spin coated film, and a single crystal sample of PAPI. Reproduced from Ref. [58].	18
2.7 Cross section of single source thermal ablation apparatus. The starting material is placed on the tantalum heater, sublimates and forms a thin film on the substrate above. Reproduced from Ref. [60].	19
2.8 (a) Absorption spectra of A) PAPI film spin coated using acetonitrile solution (dotted line), and B) PAPI doped PMMA annealed at 125°C for 10 minutes (solid line). (b) Absorption spectra of above films after being in a humidity controlled box for two months. Reproduced from Ref. [64].	20
2.9 (a) Schematic of MIMIC process for patterning PAPI films. (b) Fluorescent optical micrographs (A,B) and AFM images (C: planar, D: stereo) of patterned PAPI films. In all cases the black stripes represent bare substrate without PAPI. Film stripe widths are A) 50 μm wide, B) 15 μm , C) and D) 0.8 μm . Reproduced from Ref. [67].	21
2.10 (a) Calculated band structures of $\text{CH}_3\text{NH}_3\text{PbI}_3$ (left) and C_4PI (right) along high symmetry lines in the first Brillouin zone. The band gap is labelled. Bonding diagrams of (b) one PbI_6 octahedron, and (c) extension to $\text{CH}_3\text{NH}_3\text{PbI}_3$ and C_4PI . The bottom of the conduction band (BCB), top of the valence band (TVB), and Fermi energy level (E_F) are labelled. Adapted from Ref. [68].	22

- 2.11 (a) Polarised optical density of $C_{10}PI$ crystal at labelled temperatures (\vec{E} parallel to the QWs). (b) Photoluminescence spectra spectra of $C_{10}PI$. The temperature and scaling of plotted data are labelled. (c) Energies of absorption (Δ) and photoluminescence (\circ) peaks as a function of temperature. Reproduced from Ref. [41]. 24
- 2.12 Absorbance spectra for \vec{E} parallel to (a) \vec{b} , and (b) \vec{c} axes for $(H_3NC_6H_{13}NH_3)PbI_4$, calculated using Kramers-Kronig relations from reflection spectra. The $n = 1, 2$ peaks are labelled, and arrows indicate vibronic sidebands. Reproduced from Ref. [71]. 25
- 2.13 (a) Photoluminescence spectra of C_6PI film excited by 337 nm nitrogen laser at 4.2 K. The excitation intensity and data scaling are given. Exciton (ex) and biexciton (XX) bands are labeled. (b) Emission spectra of C_6PI waveguide above (24 kW/cm^2) and below (12 kW/cm^2) the lasing threshold at 4.2 K. The lasing wavelength is 543.6 nm. Reproduced from Ref. [76]. 26
- 2.14 (a) PL spectra of PAPI at different excitation intensities and energies. (a) was excited at 2.58eV, and (b)-(h) at 2.355eV. The excitation intensities are (a) 4.6×10^{10} , (b) 4.6×10^{12} , (c) 1.4×10^{13} , (d) 2.8×10^{13} , (e) 4.6×10^{13} , (f) 9.2×10^{13} , (g) 1.6×10^{14} , and (h) 3.2×10^{14} photons cm^{-2} . The dotted line shows the absorption spectrum. X is the free exciton band, X_{ph} phonon sidebands, M the biexciton band, Q_1 amplified spontaneous recombination of biexcitons, and Q_2 the $\hbar\omega_2$ triexciton process. (b) A shows the triexciton model, and B) likely dissociation mechanisms. For the meaning of symbols see the main text. Reproduced from Ref.[77]. 27
- 2.15 (a) Generalised description of quantum well (region I) and barriers (regions II and III). (b) and (c) show the positions of initial charges (white circle, Z_0) and image charges created (black circles) due to interfaces. In (b) the initial charge is in the well region, whereas in (c) it is in the barrier region. Reproduced from Ref. [81]. 29
- 2.16 Variations in exciton energy (red) and band gap (black) with Pb-I-Pb angles calculated using extended Huckel tight binding calculations. Data points given are experimentally determined for PbI perovskites, and filled in circles represent PL maxima of labelled $C_{12}PI$ phases. Reproduced from Ref. [44]. 30
- 2.17 Schematic of (a) a distributed feedback microcavity, (b) Fabry-Perot microcavity. (a) reproduced from Ref. [92], (b) from [93]. 31

2.18 (a) Structure of the silica opal infiltrated with PAPI film formed on a glass substrate. θ , the angle of incident light, is also shown. (b) Extracted mode positions from angle-dependent reflectivity spectra (black circles) for opal with PAPI filling fraction $f_{\text{PAPI}} = 0.06$. Exciton energy (dashed line) and theoretical photonic crystal stop gap (solid line) are marked. Reproduced from Ref. [98].	33
2.19 (a) Schematic of EL device with PAPI by Era <i>et al.</i> (top) and the molecular structure of OXD7 (bottom). (b) Energy level diagram of the EL device in (a). (c) Schematic of the LED made using PAPI by Matsushima <i>et al.</i> . (a-b) reproduced from Ref.[99], (c) from [100].	34
2.20 (a) EL (solid lines) and PL (dotted lines) spectra of the labelled perovskite at 110 K. EL device structure is shown in Fig. 2.19(a). (b) Integrated PL intensity of CHPI, PAPI, and PBPI thin film samples as a function of temperature. Reproduced from Ref. [101].	35
3.1 Schematic for SPP oscillations at a metal-dielectric surface, showing the evanescent nature of such plasmons.	38
3.2 Dispersion of SPPs on metal-dielectric interface for (a) free electron gas and (b) silver (solid lines), and light lines in the dielectric (dashed lines).	40
3.3 (a) Diffraction from a 1D grating structure, showing the incident light and diffracted orders. Dispersion (left) and modes as a function of incidence angle θ (right) for (b) photonic and (c) plasmonic modes for specularly reflected zeroth order mode for a $D = 500$ nm grating.	42
3.4 Wood's anomaly in the reflectivity of Ag grating, $D = 417$ nm. Schematics of the threshold and resonance anomalies are included.	43
3.5 Dependence of resonance anomaly on the grating depth h for sinusoidal grating, $D = 556$ nm at $\lambda = 647$ nm from (a) electromagnetic theory and (b) experiment. Reproduced from Ref. [122].	44
3.6 (a) E -field profiles of channel plasmon polariton modes in a V-shaped (left) and trench (right) Au groove, with width $3.75 \mu\text{m}$ and depth $3 \mu\text{m}$ filled with air. (b) Topographical (top) and near-field optical (bottom) images for V-shaped Au slit with width $0.6 \mu\text{m}$ and depth $1 \mu\text{m}$ at $\lambda = 1440$ nm. Reproduced from Refs. [124, 125].	46

3.7	(a) Geometry of homogeneous metal sphere with diameter d placed inside a electrostatic E -field. (b) E -field profile of dipole LSP. (c) Normalised extinction spectra for $d = 20$ nm Ag/Au NPs in air.	47
3.8	Absorption (dashed lines), scattering (dotted lines) and extinction (solid lines) cross sections for Ag NPs $d = 30$ and 90 nm at $\lambda = 500$ nm in air according to Eq. 3.14, normalised so that the peak extinction is 1. The $d = 90$ nm data has been shifted for clarity.	48
3.9	Extinction for NPs with labelled d in air using Mie theory, normalised to the dipole maximum and offset for clarity. The quasi-static approximation resonance is added for comparison.	49
3.10	(a) Discrete dipole approximation calculations of the extinction (black), absorption (red) and scattering (blue) of Ag nanoparticles with the geometries shown. (b) SEM images and normalised scattering spectra of individual Ag nanobar (top) nanorice (bottom) structures. Reproduced from Refs. [130, 131].	50
4.1	Schematic of optical microscopy and spectroscopy setup, including the reflection and transmission beam paths.	53
4.2	BF images at $100\times$ magnification of spin coated C ₁₂ PI films, with spin speed and substrate preparation as labelled. Note the substrate was heated for (d) only.	54
4.3	(a) Reflection and (b) transmission spectra for C ₁₂ PI films on silanised glass substrates made using a variety of spin speeds.	55
4.4	(a) Reflection and (b) transmission spectra for 4000 rpm C ₁₂ PI films made using a variety of substrate preparation techniques.	56
4.5	Degradation of 2000 rpm C ₁₂ PI thin films shown in $100\times$ magnification BF images. Images of the sample were taken as-made (left), and after one week in standard conditions (right).	57
4.6	BF images at $100\times$ magnification of spin coated CHPI films, with spin speed and substrate preparation as labelled.	58
4.7	Reflection and transmission spectra for CHPI films prepared using a variety of spin speeds on (a,b) untreated and (c,d) silanised substrates. (e) Effect of spin speed on CHPI film thickness on untreated substrates for 30 mg/ml solutions. The dashed lines represents a fit to $a\omega^{-b}$, with $b = 0.45 \pm 0.01$. .	59

4.8	Reflection and transmission spectra (collection spot diameter $\approx 20\ \mu\text{m}$) of 2000 rpm CHPI films created using a variety of substrate preparation techniques. Reflection and transmission spectra (collection spot diameter $\approx 1\ \mu\text{m}$) of 4000 rpm CHPI films prepared on (c) untreated and (d) silanised and snowjetted substrate at the positions indicated.	60
4.9	BF images at $100\times$ magnification for 4000 rpm CHPI films made on untreated substrates in (a) low, (b) high and (c) dehydrated spin coater atmospheres.	61
5.1	Preparation of exfoliated perovskite samples.	64
5.2	Intercalated and exfoliated perovskite microcrystals.	65
5.3	Images in $100\times$ magnification using (a) bright and (b) dark field on an exfoliated CHPI flake; (c) AFM image of the same area. (d) Reflectivity spectra of two regions on the flake. The exciton wavelength is indicated by the dashed line. (e) Relationship between the measured reflectivity minimum (labelled as R_{\min} in (d)) and AFM thickness. (f) Histogram of heights measured in the boxed area of (c). Multipeak fitting to the data (blue lines) gives an interlayer spacing of 1.6 nm. The inset shows the structure of 2D PbI perovskites.	66
5.4	Fitted complex refractive index of CHPI flakes for more than 200 pixels. Two regimes are found: (a) low absorption, occurring at positions of high thickness ($t \gtrsim 25\ \text{nm}$), and (b) high absorption, at lower thickness ($t \sim 10 - 25\ \text{nm}$).	67
5.5	Fitted exciton (a) amplitude, (b) wavelength, and (c) linewidth from reflectivity spectra (see Eq. 5.2). Dashed lines are guides for the eye.	68
6.1	SEM images of (a-c) as-deposited and (d-f) annealed evaporated Au metal island films. The initial deposited film thickness t is labelled.	73
6.2	AFM profiles of annealed Au metal island films. The deposited film thickness t is labelled. Insets show $100\times$ magnification DF images of the samples.	74
6.3	BF images at $100\times$ magnification for CHPI films on (a) glass, (b) $t = 8\ \text{nm}$ as-deposited and (c) $t = 8\ \text{nm}$ annealed Au metal island films. (d) Average extinction spectra for 400 pixels over $0.5.5\ \text{mm}^2$. The exciton wavelength is marked by the dashed line, and LSP resonances by arrows. The CHPI + (annealed) Au spectra are offset for clarity.	75

6.4	SEM images of (a-c) as-deposited and (d-f) annealed evaporated Ag metal island films. The initial deposited film thickness t is labelled. Dark areas/streaks are seen in (a, d, e) due to charging of the sample.	75
6.5	AFM profiles of annealed Ag metal island films. The deposited film thickness t is labelled. Insets show $100\times$ magnification DF images of the samples.	76
6.6	Average extinction spectra of 400 pixels over $0.5 \times 0.5\text{mm}^2$ for (a) as-deposited and (b) annealed Ag metal island films with the labelled thickness t . (c) Extinction peak position and linewidth for the spectra in (b).	77
6.7	BF images at $100\times$ magnification for CHPI films on (a) glass, (b) $t = 8\text{ nm}$ as-deposited and (c) $t = 8\text{ nm}$ annealed Ag metal island films. (d) Average extinction spectra for 400 pixels over $0.5 \times 0.5\text{mm}^2$. The exciton wavelength of the CHPI film on glass is marked by the dashed line. The (annealed) Ag MIF spectra are offset for clarity.	78
6.8	AFM profiles of (a) CHPI film on glass, (b) $t = 2\text{ nm}$ evaporated Ag film on glass, and (c) $t = 2\text{ nm}$ evaporated Ag film on CHPI. Insets show $100\times$ magnification BF images of the samples. (d) Average extinction spectra for 400 pixels over $0.5 \times 0.5\text{mm}^2$. The exciton wavelength of the CHPI film on glass is marked by the dashed line. The Ag MIF spectrum is offset for clarity.	79
6.9	(a) Illustration of the creation of $D = 460\text{ nm}$ PS colloidal monolayer on a water droplet. (b) SEM of colloidal monolayer formed after the evaporation of water. (c) SEM of triangular islands formed after evaporation of Au and removal of colloids.	81
6.10	Average extinction spectra (400 pixels over $50 \times 50\mu\text{m}^2$ for CHPI-coated Au islands as labelled. Arrows indicate the positions of LSP resonances, and a dashed line indicates the exciton wavelength.	82
7.1	(a) Fabrication and (b,c) setup of optical measurements on dielectric-coated metal gratings.	86
7.2	(a) AFM image and (b) schematic structure of $D = 417\text{ nm}$ ETFE grating. Reflectivity measurements of ETFE grating in (c,d) TM and (e,f) TE polarisation.	87
7.3	Reflectivity measurements of $D = 417\text{ nm}$ CHPI-coated ETFE grating in (a,b) TM and (c,d) TE polarisation.	88
7.4	(a) SEM image and (b) schematic structure of $D = 417\text{ nm}$ Ti grating. Reflectivity measurements of Ti grating in (c,d) TM and (e,f) TE polarisation.	90

7.5 (a) TM and (b) TE polarised reflectivity scans of 70 nm CHPI film on 120 nm planar Ti film compared to transfer matrix simulations.	91
7.6 (a) AFM image and (b) schematic structure of $D = 417$ nm CHPI-coated Ti grating. Reflectivity measurements of CHPI-coated Ti grating in (c,d) TM and (e,f) TE polarisation.	92
7.7 TM and TE specular reflectivity scans of uncoated Ag gratings, $D = 556$, 417 and 278 nm.	93
7.8 (a) SEM image and (b) schematic structure of $D = 417$ nm Ag grating. Reflectivity measurements of Ag grating in (c,d) TM and (e,f) TE polarisation.	94
7.9 (a) Experimental and modelled TM reflectivity spectra of $D = 417$ nm Ag grating for $\phi = 0^\circ$, $\lambda = 600$ nm. (b) Time averaged E -field intensity ($\vec{E} \cdot \vec{E}$) profile for $\lambda = 600$ nm, $\theta = 40^\circ$. (c) H_z nearfield profile at time t of the optical cycle T for $\lambda = 700$ nm, $\theta = 30^\circ$	95
7.10 Effect of grating geometry on the optical spectra of $D = 417$ nm Ag gratings.	96
7.11 (a) AFM image and (b) schematic structure of $D = 417$ nm PS-coated Ag grating. Reflectivity measurements of PS-coated Ag grating in (c,d) TM and (e,f) TE polarisation.	97
7.12 (a) Time averaged and (b) snapshots at time t in the optical cycle T of the E_y nearfield intensity for the higher energy (plasmonic) mode at $\phi = 90^\circ$, $\theta = 10^\circ$. (c,d) Same as above for the lower energy (waveguide) mode. The arrows represent the size and direction of the E -field vector.	99
7.13 Schematic structure of PS-coated $D = 417$ nm Ag gratings (top), and TM polarised reflectivity scans at $\phi = 90^\circ$ (bottom). PS thickness increases from (a) - (c). Plasmonic modes are indicated by black lines, and waveguide modes by purple lines.	100
7.14 TM specular reflectivity scans of CHPI-coated Ag gratings with the labelled D and ϕ . Photonic grating modes are marked by grey dashed lines, plasmonic grating modes by black dashed lines, and excitons indicated by red arrows.	100
7.15 Specular reflectivity scans at $\phi = 0^\circ$: CHPI-coated Ag grating with (a) TM and (b) TE polarised light, and (c) CHPI-coated 120 nm planar Ag film with TM polarised light. The electric field orientation is shown above each scan, the reflectivity spectra at $\theta = 20^\circ$ below, and positions of exciton modes are indicated by arrows.	101

7.16 (a) Change in emitted energy (top) and relative decay probabilities (bottom) of an exciton with energy 2.6 eV placed distance l from the Ag surface. The dashed line indicates the experimentally measured redshift. (b) Schematic mechanism for SPP-mediated emission of image-biexciton.	103
7.17 (a) AFM image and (b) schematic structure of $D = 417$ nm CHPI-coated Ag grating. Reflectivity measurements of CHPI-coated Ag grating in (c,d) TM and (e,f) TE polarisation.	104
7.18 (a) Extracted spectral mode positions for $\phi = 90^\circ$ reflection dips (open circles), and fit from three oscillator coupling model (dashed lines). (b,c) Time-averaged E -field intensity profiles ($\vec{E} \cdot \vec{E}$) as indicated. (d,e) Simulated reflection spectra for (d) in-plane and (e) out-of-plane exciton dipoles.	106

Nomenclature

Acronyms / Abbreviations

AFM Atomic force microscope

BF Bright field

C₁₂PI (C₁₂H₂₅NH₃)₂PbI₄

CHPI (C₆H₉C₂H₄NH₃)₂PbI₄

DF Dark field

LSP Localised surface plasmon

MQW Multiple quantum well

SEM Scanning electron microscope

SPP Surface plasmon polariton

Chapter 1

Introduction

Semiconducting behaviour was first reported in the 19th century. Michael Faraday noted in 1839 that the conductivity of silver selenide increased with temperature, opposite to what is expected in a metal [1]. In 1839 Alexandre-Edmond Becquerel reported photovoltaic behaviour in silver chloride coated platinum electrodes in an aqueous nitric acid electrolyte, where an increase in the voltage was observed when one electrode was illuminated with sunlight [2]. A photovoltaic cell was produced by Charles Fritts in 1883 using 30 μm thick selenium film with thin gold leaf contacts, with efficiency <1% [3]. Photoconductivity was first reported in selenium bars by Willoughby Smith in 1873, showing in the change in resistance as a result of exposure to sunlight [4], as well as William Grylls Adams and Richard Evans Day in 1876, who reported the production of electricity in selenium due to an exposure to sunlight [5]. Electroluminescent behaviour was first reported in SiC by Henry Joseph Round in 1907, who reported emission when a current was passed through crystals [6]. Simple principles such as these underpin the electronic devices we use today, yet it was not until Alan Wilson's work on band theory in 1931 that such behaviour could be understood and explained [7].

Throughout the 20th century research was focused on using semiconductors for devices, from the developments of rectifiers and diodes in the early part of the century to the first transistor built at Bell Laboratories in 1946 by William Shockley [Fig. 1.1(a)], John Bardeen and Walter Brattain using Ge. Much work has been undertaken to refine and improve the design of these devices to the more sophisticated designs used in our devices today, however the efficiency of such devices hinges on the quality of the semiconducting material used, and the ability to control impurities and dopants in the crystal. From the earliest devices using materials such as lead selenide, we now moved on to devices made using Si and Ge, which are still used today.

Si is the most widely used material in the semiconductor industry due to its abundance in the Earth's crust, low unit cost and simple and well-developed processing techniques. Its high band gap gives it thermal stability, allowing it to be used at high operating temperatures. Si is also highly mechanically stable with high electron mobility, and the native oxide insulating layer that spontaneously grows can be useful in electronics. Although Ge has higher conductivity than Si, its lower band gap gives devices more temperature sensitivity so it is less often used in devices. Alloys of Si and Ge may be used to combine the properties of both materials. One of the main disadvantages of Si is its indirect band gap, meaning it is a poor emitter for luminescence devices. However the GaAs has a direct band gap and can be used in luminescent devices, and its high electron mobility and band gap means it can be used in high speed devices. Other alloys, for example between Group III-V or II-VI atoms, can be used to tune the band gap and other optoelectronic properties. Alloys can also be combined to make lower-dimension structures, producing other desirable properties.

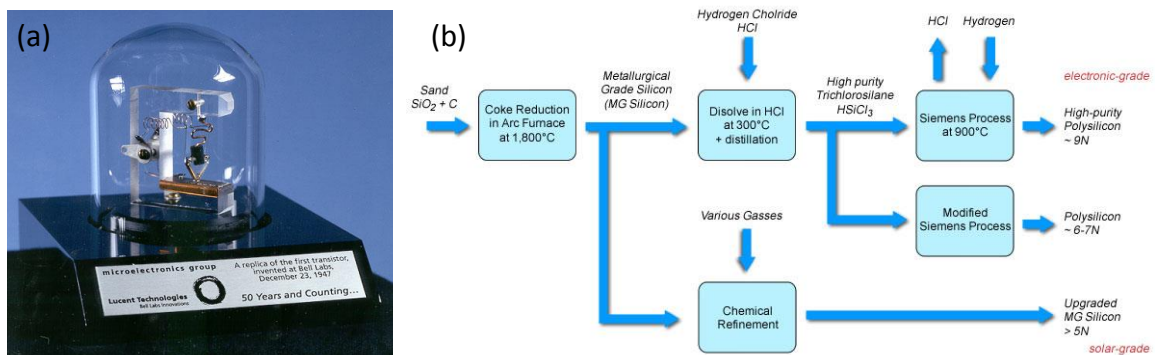


Fig. 1.1 (a) Replica of first transistor built in 1946. Reproduced from Ref. [8]. (b) Schematic of process required to produce device-grade silicon from starting materials. Reproduced from Ref. [9].

Despite the high stability and carrier mobility in inorganic semiconductors mentioned previously, one major disadvantage is with the processing of such materials. Although Si processing is well-developed, creation of device-grade material still requires many purification steps [Fig. 1.1(b)]. Alloys are often produced using vapour or electron-beam deposition, and as such the environmental parameters must be strictly controlled. Layer-by-layer growth can be used for the best quality material, however such processes are costly and time consuming. Current advances in technology require flexible, lightweight and more easily processable semiconductors.

Although conduction was noted in a mix of aniline and sulphuric acid by Henry Letherby in 1862, research on organic semiconductors began in earnest in the latter half of the 20th

century. Polycyclic aromatic compounds were found to form semiconducting charge transfer complexes with halogens in 1954 [10], and since then much work has been done on developing new molecules and polymers with desired optoelectronic properties, driven by the relative ease with which such molecules can be synthesised. Doping was developed in the 1970s to produce metallic and even superconducting complexes, for example highly conductive oxidised and iodine-doped polyacetylene in 1979 [11]. Organic semiconductors consist of conjugated molecules, whose overlapping π orbitals allow charge transport within the molecule. Given the low production cost, work has been undertaken to produce devices made of organic semiconductors, notably organic photovoltaics, thin film transistors, and light emitting diodes (OLED), probably the most mature organic electronic device as OLEDs have been used mobile phone displays and TVs, with better efficiency and brightness. However problems exist with the manufacturing of such devices, as mass production is not currently optimised for the organic electronic market. More fundamentally, organic semiconductors are less thermally, optically and electrically stable than their inorganic counterparts, leading to lower lifespan of devices. Charge mobility is also lower as hopping between adjacent molecules is required, and lower crystallinity of materials leads to scattering at grain boundaries.

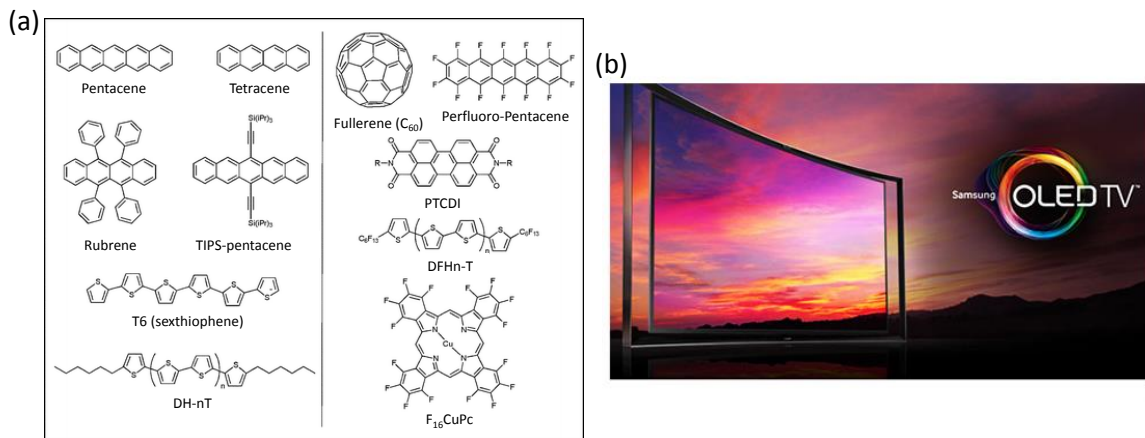


Fig. 1.2 (a) Common organic semiconductors, with p-type materials on the left and n-type on the right. Modified from Ref. [12]. (b) Samsung curved smart OLED TV. Reproduced from Ref. [13].

A new class of hybrid materials has emerged in the last 20 years. Metal halide based organic-inorganic perovskite semiconductors combine the stability of the inorganic semiconductors with the processability of organic semiconductors. A variety of inorganic frameworks can be formed, all of which are self-assembling. Charge carriers are excited in the

inorganic network, and thus share similar optical and electrical properties.

This thesis explores the optical properties of 2D lead iodide-based perovskites, particularly the interactions of perovskite excitons and collective electron oscillations in noble metal nanostructures called surface plasmons. We will first introduce the theory of excitons and review the research on lead iodide perovskites, before exploring the optical properties of surface plasmons. In Chapter 4 we will explore the fabrication of perovskite thin films via spin coating, then study the optical properties of ultra-thin perovskite samples produced via exfoliation in Chapter 5. In Chapter 6 we will explore exciton-localised surface plasmon interactions in perovskite-coated metal island structures. Finally in Chapter 7 we look at the coupling between excitons and surface plasmon polaritons in coated plasmonic gratings.

Chapter 2

Excitons in lead iodide perovskites

2.1 Properties of excitons

In a solid, electrons exist in allowed energy bands as a result of mixing and overlap between discrete atomic orbitals. If a electron does not interact with its surroundings (free electron approximation), then it has energy $E = \frac{\hbar^2 k^2}{2m_e}$ where k the wavevector of the electron wavefunction and m_e is the rest mass of a free electron. However in reality electrons interact with both positive atomic cores and other electrons, giving rise to a deviation from the free electron dispersion, and disallowed energy states (band gaps). Calculating the band structure of even the simplest systems is a complex many-body problem, and in general cannot be solved analytically.

However we can still use some basic principles to describe the behaviour of charge carriers in solids. The most important energy bands are the valence band (VB, the highest band occupied by electrons) and the conduction band (CB, the lowest non-occupied band). The difference between the highest energy point of the VB and lowest energy point of the CB is known as the band gap E_g . When this gap occurs at the same k point the material is said to have a direct band gap, and if not the band gap is indirect. The Fermi energy E_F is the energy of the highest occupied state at 0 K, and the behaviour of charge carriers depends on the relative position of E_F with respect to the conduction and valence bands. Conduction depends on the availability of free electrons in the CB, and in a semiconductor E_F lies in a band gap so there is no conduction at 0 K. However E_g is sufficiently small ($\lesssim 1$ eV) so electrons can be thermally excited to the CB, leaving behind ‘holes’ in the VB, quasiparticles used to describe an absence of electrons, with charge $+e$ [Fig. 2.1(a)]. The behaviour of electrons in response to external forces differes from the free electron value as

a result of inter-particle interactions, thus we define the effective electron mass m_e^* as

$$m_e^* = \frac{\hbar^2}{\frac{d^2E}{dk^2}}. \quad (2.1)$$

The argument also applies to holes, to m_e^* and m_h^* depend on the curvatures of the CB and VB respectively. For the rest of the Chapter the effective mass label * will be dropped for brevity, however the free carrier mass can still be used in calculations as an approximation.

The attraction between an excited electron and hole binds them together to form a hydrogen-like neutral particle in the crystal. We can therefore use results from the hydrogen atom to find the binding energy E_B and Bohr radius a_B of an exciton:

$$E_B = \frac{\mu e^4}{32\pi^2 \epsilon^2 \epsilon_0^2 \hbar^2 n^2} = \frac{R_H}{n^2} \frac{\mu}{\epsilon^2 m_e} \quad (2.2a)$$

$$a_B = \frac{4\pi \epsilon \epsilon_0 \hbar^2}{\mu e^4} = a_0 \frac{\epsilon m_e}{\mu}, \quad (2.2b)$$

where $\mu = (\frac{1}{m_e} + \frac{1}{m_h})^{-1}$ is the effective mass of the exciton, ϵ is the dielectric constant of the material, and n is the energy level of the exciton ($n = 1, 2, 3\dots$). The Rydberg constant $R_H = 13.6$ eV, and the most probable distance between a proton and electron in the ground state $a_0 = 0.5$ Å are defined for the hydrogen atom. As a result of E_B , a series of exciton energy levels are formed below the lower edge of the CB [Fig. 2.1(a)]. The energy of an exciton E_{ex} is given by

$$E_{ex} = E_g - E_B + \frac{\hbar^2}{2M}(k_x^2 + k_y^2 + k_z^2), \quad (2.3)$$

where $M = m_e + m_h$ is the total mass of the exciton, and the k_i terms describe its motion in 3D. Eq. 2.3 gives the energy of free excitons that are able to move throughout the crystal, however excitons can be bound to impurities, further lowering their energy.

In inorganic materials, high ϵ gives rise to $E_B \sim 10$ eV and $a_B \sim 100$ Å. Such Mott-Wannier excitons extend over many unit cells, however due to low E_B the effects can only be observed at low temperatures [Fig. 2.1(c)]. Conversely organic materials have lower ϵ , such that $E_B \sim 1$ eV and $a_B \sim 10$ Å. These Frenkel excitons are limited to a few unit cells, or one molecule in the case of molecular semiconductors.

Excitons can be created optically by the absorption of photons [Fig. 2.1(a)]. In bulk semiconductors, the absorption coefficient α on an exciton depends on the initial ground

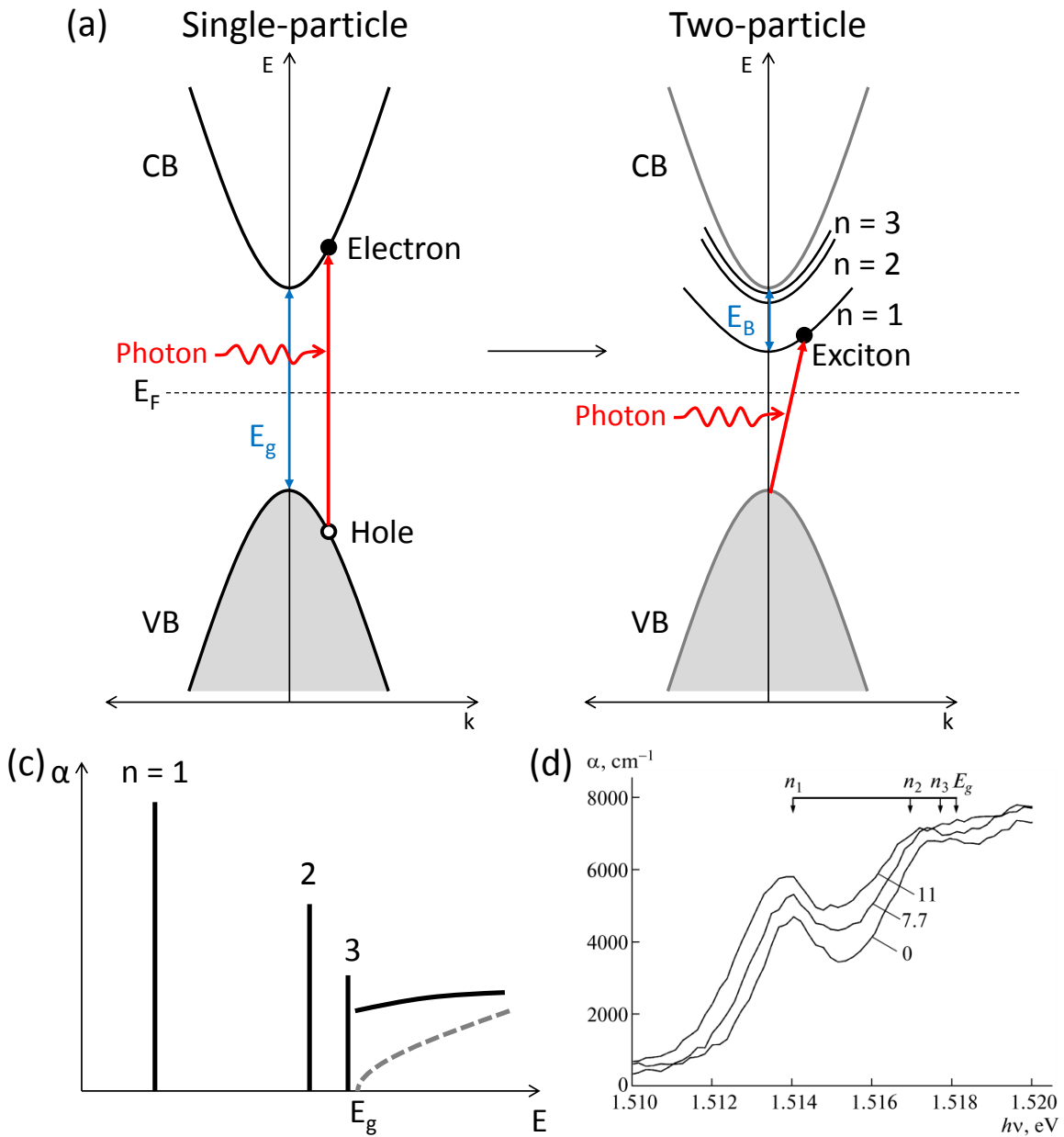


Fig. 2.1 (a) (Left) Band structure of a semiconductor, showing the single-particle representation of the excitation of an electron-hole pair via photon absorption. (Right) Two-particle representation of the same system, illustrating exciton energy levels below the CB. (b) Theoretical absorption spectrum of a 3D semiconductor according to Eq. 2.4 (not to scale). The dotted line shows the expected band edge absorption without the Sommerfeld factor (see text). (c) Experimental absorption spectrum of GaAs crystal at 1.7 K, with the labelled laser power (W/cm²). From Ref. [14].

state $|i\rangle$ (filled VB and empty CB) and final state $|f\rangle$ (one promoted electron) as

$$\alpha = |\langle f | i \rangle|^2 \rho(E), \quad (2.4)$$

where the matrix element $\langle f | i \rangle$ gives rise to selection rules of possible electronic transitions, and the joint density of states $\rho(E)$ is the number of states per unit energy range between the CB and VB at the photon energy E . In 3D $\rho(E)$ has a $\sqrt{E - E_g}$ dependence, however Coulomb interactions lead to an enhancement in the absorption by the Sommerfeld factor, and α is not discontinuous at zero at E_g as expected from Eq. 2.4 [15]. The theoretical absorption spectrum shown in Fig. 2.1(b), with discrete exciton absorption lines decreasing in intensity as n^{-3} [15], and continuous absorption at higher energy due to interband transitions. Experimental data for the absorption of a GaAs crystal at 1.7 K is shown in Fig. 2.1(c), where overlap between exciton lines and band edge absorption can be seen as a result of the exciton peak width (Γ_{ex}). The finite exciton linewidth is due to a number of factors: firstly homogeneous variables that affect each exciton equally, such as the radiative lifetime of the exciton ($\frac{1}{\Gamma_{ex}(0)}$) and collisions with phonons, secondly inhomogeneous factors such as impurities (Γ_{imp}), whose effects will be more localised. Overall this leads to a measured linewidth Γ_{ex} that varies with temperature T as

$$\Gamma_{ex}(T) = \Gamma_{ex}(0) + \Gamma_{imp}(T) + A_{ac}T + \frac{B_{op}}{\exp \frac{\hbar\omega_p}{k_B T} - 1}, \quad (2.5)$$

where the contribution to phonon collision has been further separated into coupling with acoustic phonons (A_{ac}), and interactions with polarised optical phonons of energy $\hbar\omega_p$ [16].

Once excitons are created, they can annihilate and emit energy in the form of photons. The formation of the charged constituents of excitons causes deformation of the crystal, and as a result of this structural rearrangement the exciton emission is redshifted with respect to absorption, known as the Stokes shift. In general Frenkel excitons in organic semiconductors show larger Stokes shifts as molecules are more easily deformable.

Observations of excitons in optical spectra depends on the coupling between excitons and photons, so exciton peak strength is partly determined by the oscillator strength f , given by the matrix element between the exciton and photon wavefunctions. Coupled exciton-photon states are known as exciton-polaritons. Non-propagating solutions give rise to longitudinal excitons with frequency ω_L , while travelling solutions produce transverse excitons with frequency ω_T . The longitudinal-transverse splitting $\omega_{LT} = \omega_L - \omega_T$ is again related to the coupling between excitons and photons, with $f \sim \sqrt{\varepsilon_B} \omega_{LT}$, where ε_B is the background dielectric constant of the material without excitonic contributions.

2.2 Excitons in 2D systems

Exciton motion can be confined to 2D in quantum well (QW) systems, where a material (well) is sandwiched between layers with higher E_g (barriers). If the well and barrier layers are periodically arranged then a multiple quantum well (MQW) or superlattice is formed. Four types of band alignment can be achieved [Fig. 2.2(a)]: in type I structures potential steps appear in both the VB and CB, thus confining both electrons and holes to the well region. In type II QWs band edges of the barrier layers are shifted in one direction with respect to the well, creating a staggered band alignment where the electrons are confined to the well and holes to the barrier region. In the most extreme case the barrier VB is above the well CB, creating a type II broken-gap arrangement. Type III QWs occur when a semimetal (with a small overlap between the VB and CB) is used as the well. For the rest of this section only type I QWs will be considered.

Type I QWs can be formed from many III-V materials, for example GaAs/AlGaAs, GaAs/AlAs or GaAs/GaP. In general these inorganic QWs are grown atomically layer-by-layer, either using molecular beam epitaxy (MBE) or metalorganic chemical vapour deposition (MOCVD), where the relevant atoms are deposited onto the substrate either in the gas phase or via a molecular beam. The stoichiometric mix of relevant atoms must be carefully controlled during fabrication to create the correct structures. In designing a QW system, one must also consider the lattice constants of the materials in question. A large lattice mismatch will cause strain in the layers, and the growth will not be epitaxial, i. e. there will not be a well-defined crystal structure throughout the layer. The AlAs/GaAs system has good lattice matching, or alternatively a adjustment of atomic proportions with a ternary alloy can be used to reach the lattice constant needed. It is also possible to use materials that can adapt to the local lattice constant up to a critical thickness despite strain.

The layered structure of a QW confines carrier motion in the direction of layer growth, thus creating a 2D system. If the width of the well layer L is on the order of the electron de Broglie wavelength (~ 10 nm), then carriers are trapped in a finite potential well, and we observe wave-like effects such as the creation of discrete energy levels in which electrons/holes can reside. Using the results for a particle in an infinite well for simplicity, the allowed states have energy

$$E_u = \frac{\hbar^2}{2m} \left(\frac{u\pi}{L} \right)^2, \quad (2.6)$$

where E_u is the energy of the state, m the mass of the carrier, and the index u labels the energy level. Instead of the VB/CB, we find instead a series of minibands with different energies [Fig. 2.2(b)]. The absorption spectrum of QW systems can still be calculated using

Eq. 2.4, however the orthogonality of eigenstates means that transitions from state $|u_1\rangle$ in the VB to $|u_2\rangle$ in the CB are only allowed if $u_2 - u_1 = 0$. The joint density of states $\rho(E)$ is step-like in 2D, again with the Sommerfeld factor enhancing absorption [Fig. 2.2(c)].

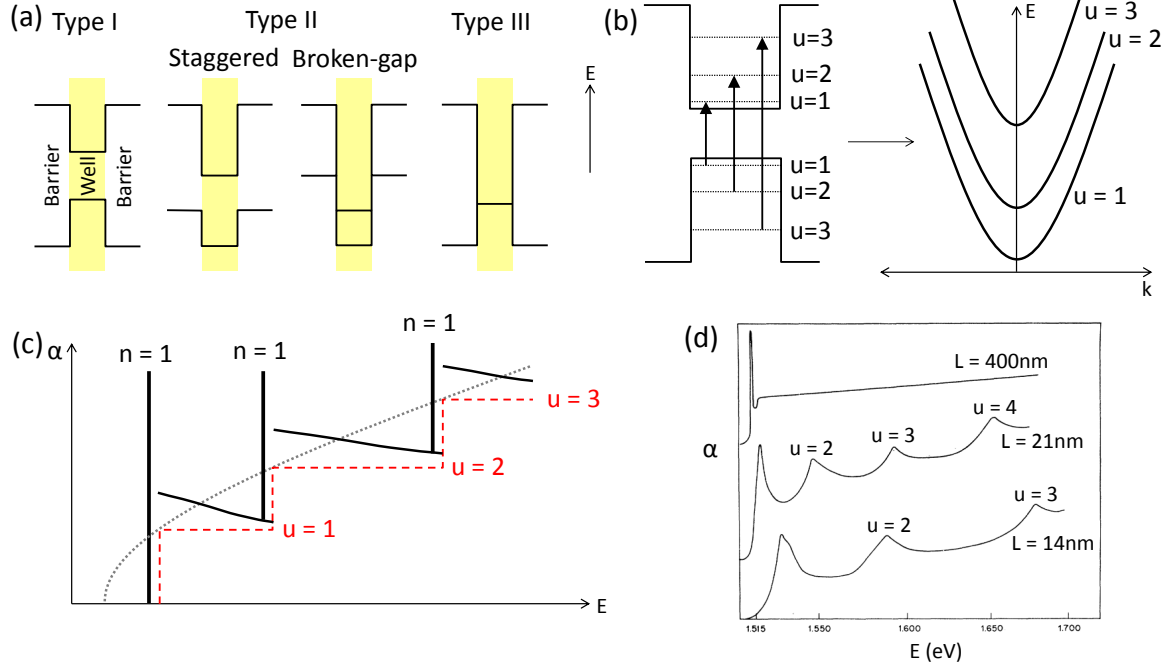


Fig. 2.2 (a) Schematic of quantum well band alignments. (b) Allowed transitions for electrons in a quantum well (left) and the resultant miniband structure (right). (c) Theoretical absorption spectrum of a 2D quantum well according to Eq. 2.4 (black lines). The dotted grey line shows the band edge absorption in 3D, the dashed red line the absorption in 2D, both without the Sommerfeld factor. (d) Experimental absorption spectrum of GaAs/Al_{0.2}Ga_{0.2}As quantum wells with the labelled well width L at 2 K. Only the $n = 1$ excitons are observed, but the minibands u are labelled. Adapted from Ref. [17].

Exciton bands exist below each of the minibands, and in order to find E_B we use the results for a hydrogen atom in 2D, such that

$$E_B = \frac{\mu e^4}{32\pi^2 \epsilon^2 \epsilon_0^2 \hbar^2 \left(n + \frac{1}{2}\right)^2} = \frac{R_H}{\left(n + \frac{1}{2}\right)^2} \frac{\mu}{\epsilon^2 m_e}. \quad (2.7)$$

Therefore the energy of the exciton bands E_{ex} can be described by

$$E_{ex} = \Delta E_u - E_B + \frac{\hbar^2}{2M} (k_x^2 + k_y^2), \quad (2.8)$$

where ΔE_u describes the transition between energy levels u in the CB and VB. The expected absorption spectrum of a QW structure is shown in Fig. 2.2(c), while experimentally mea-

sured spectra for GaAs/Al_{0.2}Ga_{0.8}As QWs are shown in Fig. 2.2(d). Note the change in L affects the allowed ΔE_u , with $L = 400$ nm essentially appearing as a 3D system.

We can see from Eq. 2.7 that the reduction in dimensionality leads to a factor of 4 enhancement in E_B for the $n = 1$ state, so exciton effects should be observable at higher temperatures in QWs. Similarly a_B is reduced by a factor of 2 in QWs as a result of confinement. For this reason it is often said that excitonic effects are stronger in QWs, with increased overlap between the electron and hole wavefunctions.

2.3 Properties of PbI perovskites

2.3.1 Structure and bonding

Metal halide RNH_3MZ_3 organic-inorganic semiconductors are based on the ABX_3 perovskite crystal structure [Fig. 2.3(a)], consisting of a corner-sharing octahedra network of halogen atoms Z (most commonly I, Br or Cl) with a metal atom M in the centre of each octahedron (+ 2 valence metals such as Pb, Sn, Cd, Zn, Cu, Co). Organic mono-ammonium molecules RNH_3 hydrogen bond to halogen atoms and reside in the interstices between octahedra [Fig. 2.3(b)], and as a result very short molecules are used, the most common of which is CH_3NH_3 . The band gaps of such semiconductors can be engineered by changing the metal and halogen composition, and recently lead halide-based semiconductors have been used as a light absorbing layer in solar cells, producing efficiencies of up to 16%, and there is currently a drive to find lead-free alternatives for wider use [18–21]. A change in the stoichiometric mix of organic and inorganic constituents results in the formation of lower dimension structures, for example 2D layered systems, or 1D inorganic wires [22–25]. From here we will focus on <100> oriented 2D lead iodide (PbI) perovskites [26].

The self-assembled structure of 2D hybrid PbI perovskites with formula $(\text{RNH}_3)_2\text{PbI}_4$ are shown in Fig. 2.3(c), and consist of alternating layers of corner-sharing PbI_6 octahedra and interdigitating RNH_3 molecules (where R is an organic moiety). The organic molecules have larger E_g (~ 6 eV) than the inorganic layers (~ 3 eV), and form a type I MQW structure [27, 28]. The bonding in inorganic layers is primarily ionic as Pb-I distances are more comparable to the sum of ionic radii [29]. The width of the PbI octahedra is ~ 6.5 Å [30]. Inorganic sheets are sandwiched between layers of organic molecules via hydrogen bonding between NH₃ groups and I atoms. The van der Waals or aromatic-aromatic interactions that bind organic molecules together can (de)stabilise the perovskite structure [31]. Like other layered materials such as graphene or transition metal dichalcogenides, it is possible to break

these van der Waals bonds and cleave the structure and produce thinner samples.

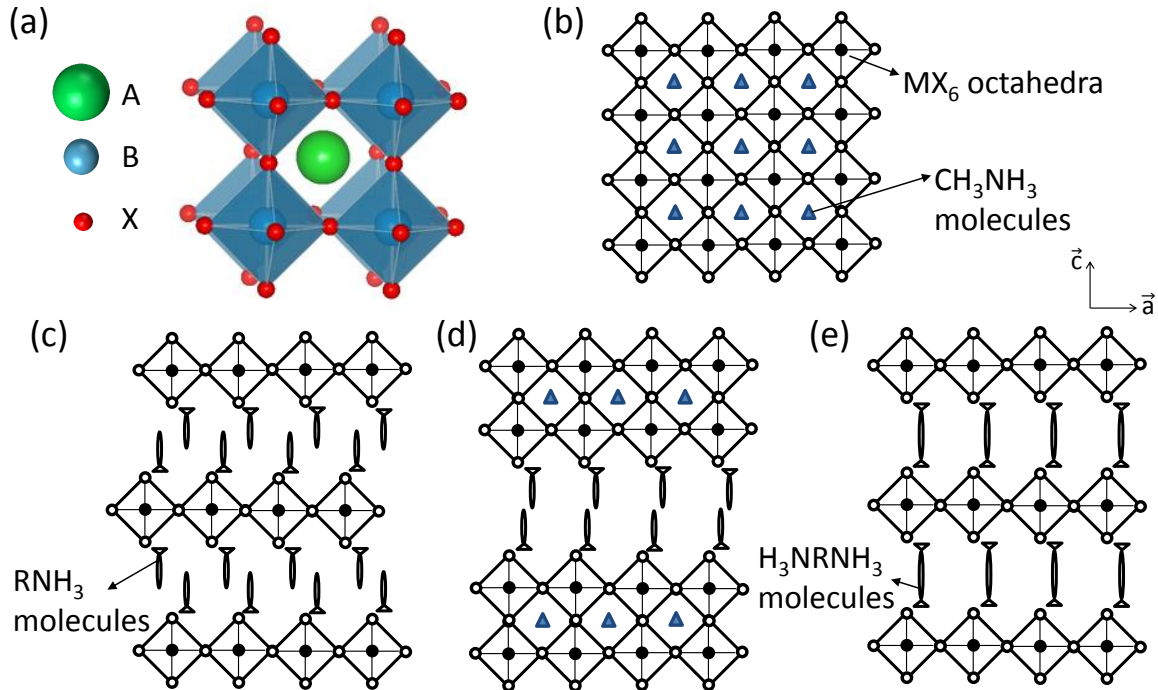


Fig. 2.3 (a) Structure of ABX_3 perovskite. Adapted from Ref. [32]. Structure of (b) 3D perovskite $(\text{CH}_3\text{NH}_3)\text{PbI}_3$, (c) 2D perovskite $(\text{RNH}_3)_2\text{PbI}_4$, (d) 2D multilayered perovskite $(\text{RNH}_3)_2(\text{CH}_3\text{NH}_3)\text{Pb}_2\text{I}_7$, and (e) 2D diammonium perovskite $(\text{H}_3\text{NRNH}_3)\text{PbI}_4$ viewed along the crystallographic \vec{b} axis.

There are two main orientations for consecutive inorganic layers: eclipsed layers produce a monoclinic structure, while staggered layers produce an orthorhombic structure [33]. The orientation is chosen to accommodate organic molecules in the structure. Phase transitions from the orthorhombic phase to the monoclinic phase will lead to a halving of the c lattice parameter due to increased symmetry [34].

There are only a few limits on the organic molecule R in the structure. The cross section of the molecule should be small enough to fit into the interlayer space between four adjacent octahedra ($\lesssim 40 \text{ \AA}^2$) [31]. However their lengths are not constrained so long as the intermolecular forces are strong enough to hold the structure together. Systems with aromatic molecules tend to be better organised with more crystallinity since such molecules allow for self-assembly using stronger aromatic-aromatic interactions [35], conversely large organic groups will hinder self assembly and reduce crystallinity [35]. In general very simple organic molecules are used, for example those based on simple alkane chains ($(\text{C}_n\text{H}_{2n+1}\text{NH}_3)_2\text{PbI}_4$, C_nPI hereafter), ring structures ($(\text{C}_6\text{H}_9\text{NH}_3)_2\text{PbI}_4$, CHPI), or aromatic molecules ($(\text{C}_6\text{H}_5\text{C}_2\text{H}_4\text{NH}_3)_2\text{PbI}_4$, PAPI). However more complex organic molecules

can be incorporated, for example optically active ligands [33, 36] and fullerene derivatives [37, 38].

The basic 2D layered structure can be varied in a series of ways. For instance the width of QWs can be varied by extending the inorganic sheets to contain multiple layers of PbI_6 octahedra ($(\text{RNH}_3)_2(\text{CH}_3\text{NH}_3)_{n-1}\text{Pb}_n\text{I}_{3n+1}$) [Fig. 2.3(d)] [39]. Another is with the use of diammonium organic molecules, which can hydrogen bond to two consecutive inorganic layers, therefore eliminating the need for van der Waals interactions between the interweaving molecules ($(\text{H}_3\text{NRNH}_3)\text{PbI}_4$) [Fig. 2.3(e)].

Phase transitions in C_nPI

Four main phases of C_nPI perovskites have been identified. For temperatures $< -30^\circ\text{C}$ (phase I), the crystal exhibits twinning so atomic positions cannot be determined. Between -30 and 15°C (phase II), organic chains are ordered with uniform tilting angle. The structure then undergoes a pre-melting transition, leading to dynamic rotational disorder of NH_3 groups and a small decrease in the \bar{c} lattice parameter [40]. Between ~ 15 and 65°C (phase III), organic chains show much more conformational disorder and become tilted at different angles, leading to a large increase in c , and thus an increase in volume since no lateral motion occurs [40]. Above 65°C (phase IV), organic chains appear to be ‘melting’ [30, 41, 42]. Simulations show that after the melting transition alkyl chains are no longer all-trans, and the introduction of gauche defects leads to a shortening of the chain and an increase in its effective cross-sectional area. Conflicting demands of close packing that optimise dispersive interactions and the larger area required by conformationally disordered chains can no longer be met by a uniformly tilting arrangement, and the non-uniform tilt allows for increased space for individual chains [43]. Changes in conformation during phase transitions also cause a spatial shift in the coupling between NH_3 groups and inorganic octahedra [44]. In order to accommodate the changes in alkyl chains, PbI_6 octahedra can undergo two types of structural change: they can tilt perpendicular or parallel to the inorganic sheets. During perpendicular tilting octahedra are tilted with respect to each other, whereas parallel tilting leads to an overall corrugation of inorganic layers [34]. For $\text{C}_{12}\text{-}$, $\text{C}_{14}\text{-}$, $\text{C}_{16}\text{-}$, and C_{18}PI phase III is orthorhombic with staggered inorganic sheets, and phase IV is monoclinic with eclipsed inorganic sheets [34].

The switching between orthorhombic and monoclinic phases is not only controlled by temperature changes. Pradeesh *et al.* showed that the phases present in spin coated films of C_{12}PI depend on the thickness of the sample, as well as aging effects. They postulated that this is due to strain effects, where high strain in thicker samples favours the flatter or

orthorhombic phase. Aging effects, where a sample in the monoclinic phase gradually shifted to the orthorhombic phase, could be stopped by annealing or capping with poly(methyl methacrylate) (PMMA) [44].

2.3.2 Fabrication and processing techniques

Silica-gel method

An aqueous solution of $\text{Pb}(\text{CH}_3\text{COO})_2$, $\text{C}_n\text{H}_{2n+1}\text{NH}_2$, CH_3COOH , and Na_2SiO_3 is prepared in a test tube, and becomes a gel after approximately one week. At this point an aqueous solution of KI is poured into the gel and the I^- ions diffuse slowly into the gel to form C_nPI single crystals. About a month after the introduction of KI, platelet-like crystals form, approximately $2 \times 2 \times 0.1$ mm in size. However crystals for perovskites where $n = 4, 6$ cannot be produced using this method [41].

The silica-gel method allows multiple components to be mixed in solution on a nanometer scale, which can produce very homogeneous materials. The technique can also be used to make thin films by dissolving the raw ingredients in a suitable solvent (e. g. an alcohol) that is fast gelling and drying. The necessary condensation reaction and solvent evaporation will take place after the solution is applied to a substrate, leaving behind a wet gel film that can be heated to produce a dry film, but in order to avoid cracking the wet film should generally be less than $1 \mu\text{m}$ thick. Thin gel films are usually amorphous, but surfactants on the substrate can help with assembly and annealed films are generally crystalline [45].

Solution crystal growth

The silica-gel method is time intensive, therefore crystals of a similar or larger size are more commonly produced from solution. PbI_2 , RNH_2 and HI are usually mixed in stoichiometry (e.g. [46, 47]) and left for solvent evaporation [27]. The basic reaction scheme is $2 \text{RNH}_3 + 2 \text{HI} + \text{PbI}_2 \longrightarrow (\text{RNH}_3)_2\text{PbI}_4$. After around one week single crystals form, although the rate of evaporation can be controlled to change the morphology of crystals [48]. The difficulty lies in finding solvents that will dissolve both the inorganic and organic parts of the perovskites, and examples include acetone [49], dimethylformamide (DMF) [46], and HI [40]. If the evaporation is less controlled, this method can be used to create perovskite powder, which can later be dissolved in a suitable solvent and used in spin coating.

Spray pyrolysis/drying

Spray pyrolysis produces particles when misted streams of precursor solution are introduced to a furnace. Multicomponent particles can be prepared due to microscale reactions inside the μm -sized droplets, and new phases with narrow size distributions and non-agglomeration can be obtained rapidly after solvent evaporation and as a result of high temperature and inert gas streams inside the furnace reactor [50].

A precursor solution of stoichiometric quantities of PbI_2 and $\text{C}_6\text{H}_5\text{C}_2\text{H}_4\text{NH}_3 \cdot \text{HI}$ in tetrahydrofuran (THF) is used to prepare a PAPI powder. From scanning electron microscope (SEM) images the powder particles appear to be $\sim 1 \mu\text{m}$ in size, however XRD data indicate the structure is less organised than PAPI prepared by other methods, e. g. spin coating,. The photoluminescence (PL) spectrum of PAPI powder shows a strong exciton peak, indicating the formation of the required layered structure, however the wavelength is shifted by around 5 nm, likely due to distortion of PbI sheets [50].

A similar technique of spray drying can be used to produce perovskite nanoparticles. The precursor solution is prepared by bubbling a flow of dry HI into a dry ethereal solution of organic amine. Drying droplets (initial mean diameter $\sim 35 \mu\text{m}$) are carried from the aerosol generator by dry air into an evaporation chamber at 250°C . Dried nanoparticles created using this method are mostly spherical, but with a large size distribution (50 – 500 nm diameter; average $60 \pm 10 \text{ nm}$). The perovskite crystallises at the edge of the particle while the centre is depleted, therefore larger nanoparticles are hollow, while smaller particles are denser due to their fast drying rate. XRD data indicate the nanoparticles are crystalline, with a small redshift of a few nm in exciton PL caused by strain. The nanoparticles are also fairly photo-stable, with a drop in PL intensity of around 30-50% after illumination of 1 hour [51].

Langmuir-Blodgett technique

The Langmuir-Blodgett (LB) technique uses a movable barrier to apply pressure to a monolayer of molecules at a liquid-gas interface. When molecules are close enough van der Waals forces can create close packing, thus forming a thin film [Fig. 2.4(a)] [45]. Era *et al.* used LB to create thin films of $(\text{C}_{22}\text{H}_{45}\text{NH}_3)_2\text{PbBr}_4$. The long chain ammonium bromide ($\text{C}_{22}\text{H}_{45}\text{NH}_3\text{Br}$) is spread on an aqueous subphase containing PbBr_2 and $\text{CH}_3\text{NH}_3\text{Br}$ from a chloroform and DMF solution. The monolayer is then pressed to a surface pressure of 30 mNm^{-1} , then deposited on a hydrophobicised fused quartz substrate. Layer-by-layer deposition of LB films allows control over the film thickness. Films shows strong exciton absorption peaks, with linear increase in the absorption intensity for each additional layer

[Fig. 2.4(b)] [52].

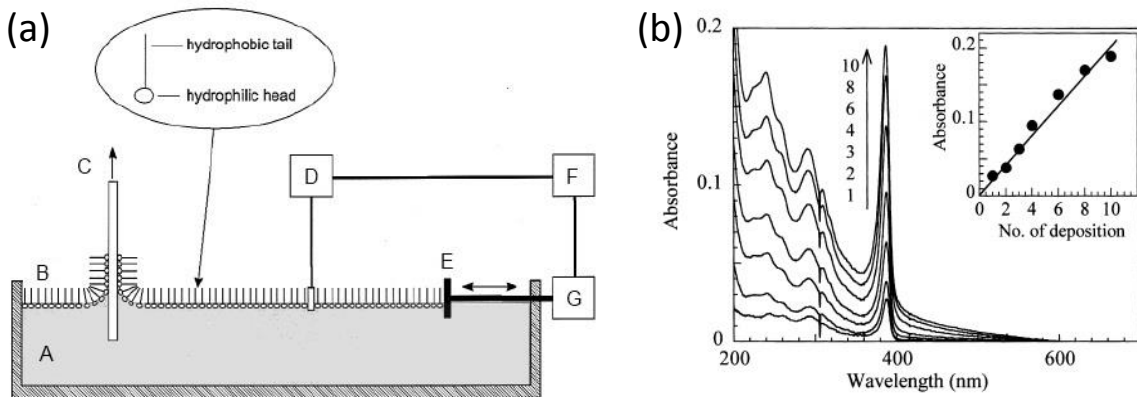


Fig. 2.4 (a) Schematic of Langmuir-Blodgett setup, with (A) a bath containing (B) the monolayer of amphiphilic molecules at the gas-fluid interface, (C) the substrates being withdrawn from the bath, and (D) a balance that measures the surface pressure of the monolayer, generated by the movable barrier. (E) The moving barrier is controlled by a feedback device (F), which gets information from the pressure sensor and adjusts the barrier position using the (G) motor. (b) Absorption spectra of LB film obtained using the labelled number of depositions, and exciton absorbance intensity against the number of depositions (inset). (a) reproduced from Ref. [45], and (b) reproduced from Ref. [52].

Intercalation

Perovskite films can be formed by the intercalation of organic molecules into the inorganic framework. PbI_2 films are deposited onto substrates by vacuum deposition or spin coating, and a solution of organic ammonium iodide prepared. The PbI_2 covered substrates are dipped in the iodide solution then dried. The resulting films have the same properties as films created using other methods [53]. The film thickness is controlled by the initial PbI_2 thickness, and in the case of $(\text{C}_6\text{H}_9\text{C}_2\text{H}_4\text{NH}_3)_2\text{PbI}_4$ (CHPI) only 10 s is needed to complete intercalation [54].

A similar dipping method has been used to make thin films of diammonium ($\text{H}_3\text{NC}_{12}\text{H}_{25}\text{NH}_3$) PbI_4 . Hydrophilic quartz substrates are alternately dipped in organic diammonium iodide and PbI_2 solutions for 20/15 mins respectively, with care taken to remove excess reactants after each step. The procedure can be repeated as needed to create multilayers of self-assembled quantum wells and control the film thickness [55].

Gaseous intercalation has also been demonstrated by Era *et al.*. A 20 nm thick film of PbI_2 is vacuum deposited on a quartz substrate, then exposed to vaporised organic ammonium iodide ($\text{C}_6\text{H}_5\text{C}_2\text{H}_4\text{NH}_3\text{I}$). Both XRD and absorption confirm the formation of PAPI,

although in XRD signatures of PbI_2 can still be seen [56].

Recently in-situ measurements on liquid-phase intercalation has shown that the process begins from the top surface of the PbI_2 film, and proceeds parallel to the \vec{c} axis. Organic molecules attach to the top PbI_2 layer as terminal groups, and transform the edge-sharing PbI octahedra into a corner-sharing network. Interstices are opened for the diffusion of organic molecules, which interact with the bottom surface of the same layer, thus converting the PbI_2 layer into full 2D perovskite monolayer. Further diffusion continues intercalation for subsequent layers [Fig. 2.5]. This process requires a non-polar solvent that will not compete with the hydrogen bonding between the inorganic and organic constituents. An optimum organic iodide concentration exists due to steric hindrance of neighbouring molecules [57].

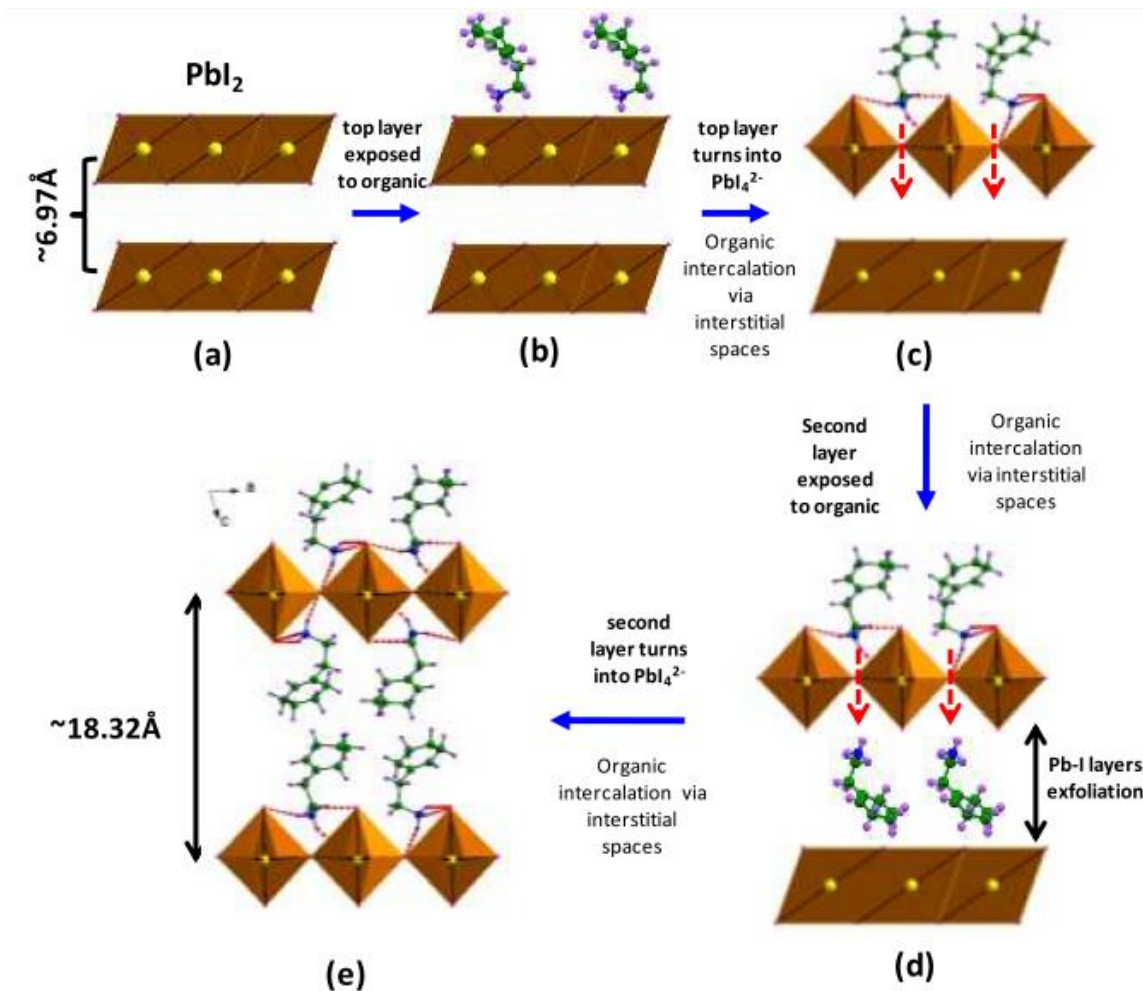


Fig. 2.5 Molecular dynamics for the liquid-phase intercalation of organic ammonium iodide molecules into PbI_2 film. Reproduced from Ref. [57].

Dual-source vacuum deposition

PAPI films can be created using a dual-source vacuum deposition method, where both PbI_2 and $(\text{C}_6\text{H}_9\text{C}_2\text{H}_4\text{NH}_3)\text{I}$ are deposited simultaneously on a quartz substrate [Fig. 2.6(a)]. The created films show the same sharp exciton absorbance peaks as films created by other methods, however XRD data show no peaks at high θ , so the films are disordered defective. The growth of the layered perovskite structure appears to occur in the solid phase on the substrate [58]. As the organic ammonium halide may dissociate into an amine and HI, care needs to be taken with choice of evaporation rates, or else films can be multiphasic, disordered or defective [59].

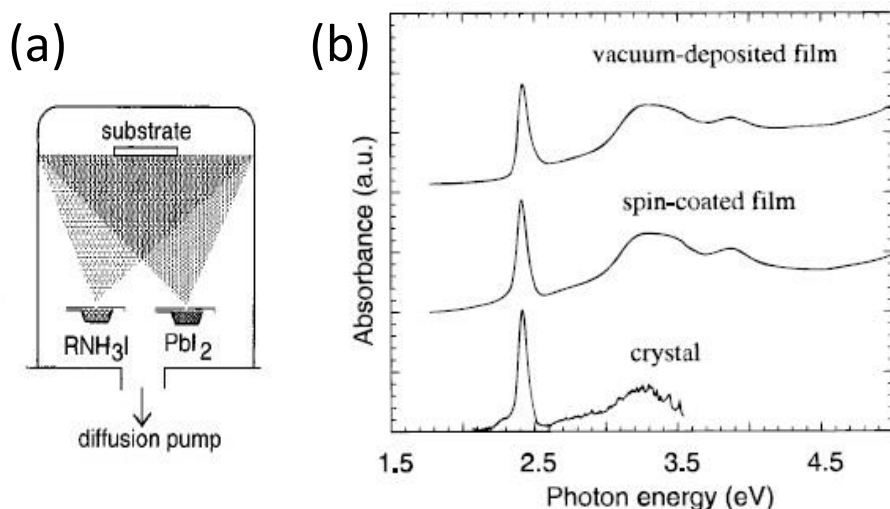


Fig. 2.6 (a) Schematic of dual-source vacuum deposition process. (b) Absorbance spectra of a vacuum deposited film, a spin coated film, and a single crystal sample of PAPI. Reproduced from Ref. [58].

Single source thermal ablation

Single source thermal ablation involves the vaporisation of a material onto a substrate in order to form a film [Fig. 2.7]. A powder of the material is placed on a tantalum heater as a powder, the chamber is then pumped to vacuum, and a current passed through the heater. The starting material is vaporised from the heater surface and reassembles on the substrate above. The important control variable is the rate at which the heater reaches its final temperature, as a low rate may lead to multiphasic or defective films. Substrates can undergo multiple ablations, and the mass of material on the heater can also be used to control film thickness [59]. AETHPI (AETH = $\text{C}_{18}\text{H}_{28}\text{N}_2\text{S}_2$) films have been created using

this method. Luminescence spectra show that as-formed films have only traces of a small exciton peak, however quantum well quality is improved by annealing as the exciton peak intensity increases [60].

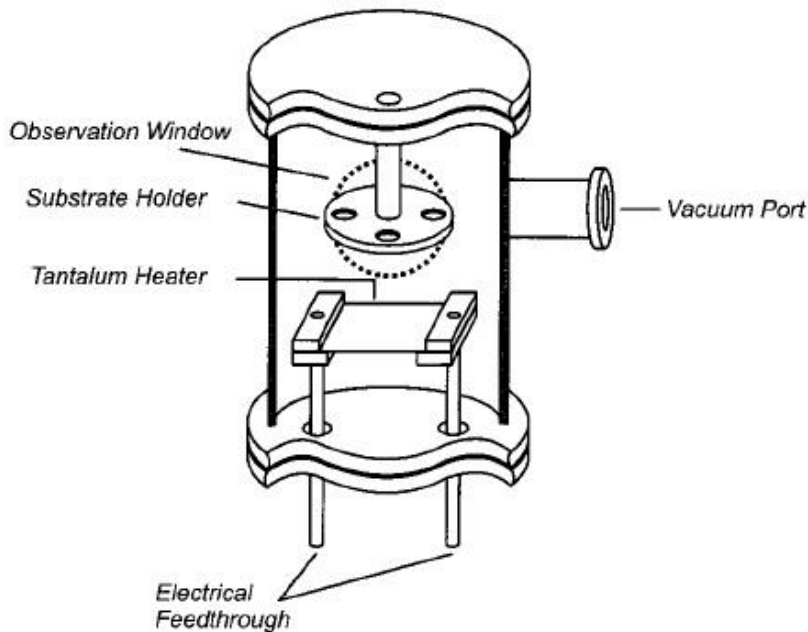


Fig. 2.7 Cross section of single source thermal ablation apparatus. The starting material is placed on the tantalum heater, sublimates and forms a thin film on the substrate above. Reproduced from Ref. [60].

Spin coating

Thin films can easily be produced by spin coating a perovskite solution on a substrate. Drops of solution are added to spinning substrates, and as the solvent evaporates a polycrystalline film is left behind. Suitable solvents include DMF [37], THF [61], and acetonitrile [62]. The films produced have the same optical and electronic properties as single crystals, and the crystallographic \vec{c} axis perpendicular to the surface of the films [63]. The films are generally smooth and can have a roughness of 1-2 nm, although the solvent, substrate preparation, perovskite solution concentration, substrate temperature and spin speed may all affect the thickness and morphology of films [45]. In thicker films, strain and uneven crystal planes lead to stacking imperfections, which may give distorted quantum wells of differing widths and a decrease in the intensity of exciton absorption/luminescence [62].

PbI perovskite samples tend to degrade over time due to moisture in the air, so a PMMA matrix doped with nanocrystalline PAPI can be created in order to suppress degradation

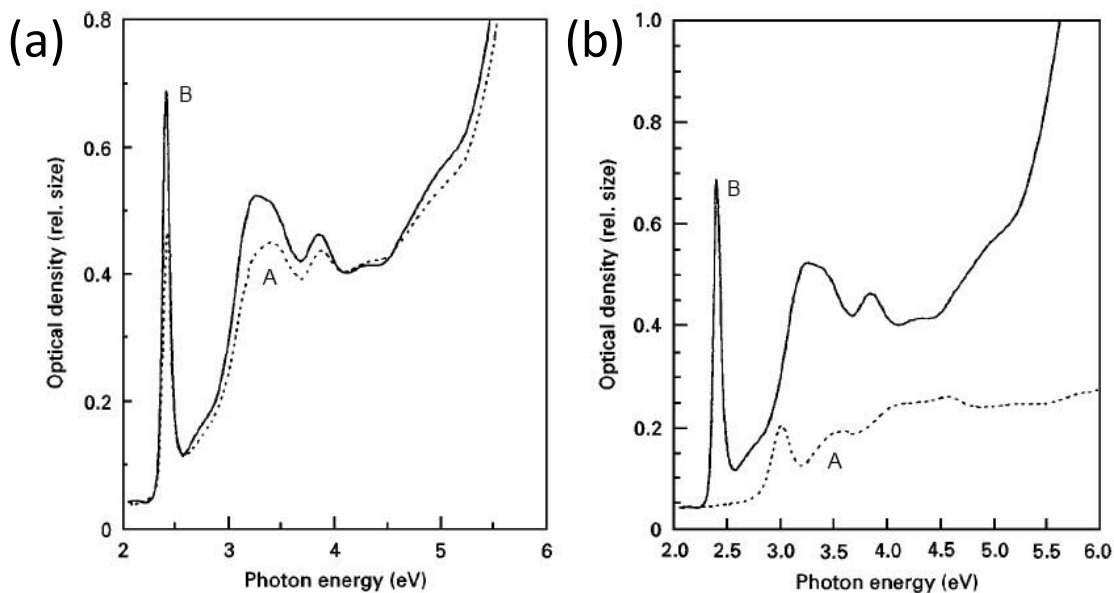


Fig. 2.8 (a) Absorption spectra of A) PAPI film spin coated using acetonitrile solution (dotted line), and B) PAPI doped PMMA annealed at 125°C for 10 minutes (solid line). (b) Absorption spectra of above films after being in a humidity controlled box for two months. Reproduced from Ref. [64].

[64]. PPMA, PbI₂, and C₆H₉C₂H₄NH₃I are dissolved in DMF then spin coated onto a glass substrate, and the resulting film annealed (thickness \approx 200 nm). The \vec{c} axis of PAPI crystals are perpendicular to the surface of the film, and a strong exciton absorption at 2.4 eV is seen as well as a step-like feature at 2.7 eV due to interband transitions [Fig. 2.8(a)]. The binding energy of excitons in PMMA doped films is around 300 meV, larger than in pure PAPI samples (250 meV) due to dielectric confinement of PMMA. After two months in a humidity controlled box, absorption of the PAPI-doped PMMA sample is almost unchanged, however the spin coated PAPI film is degraded and no exciton peak can be seen [Fig. 2.8(b)].

The degradation of perovskite films is partly caused by the production of halide radicals, which can form halogen gases or compound degradation by reacting with organic moieties. Structures with more electron-rich organic molecules are therefore less resistant to attach from electrophilic halide radicals [65]. Kondo *et al.* reported oxygen(1s) signatures in the photoelectron spectrum of photo-irradiated PAPI films, so photo-induced oxidation is another likely mechanism for photo-degradation [66].

Patterning

Patterned PAPI films have been produced using a micromoulding in capillaries method (MIMIC). Polydimethylsiloxane (PDMS) moulds are created by casting on silicon master moulds, then placed in conformal contact with pre-cleaned silicon substrates so the channels of the mould formed capillaries. A solution of PAPI dissolved in DMF is dropped on one end, and the channels are spontaneously filled by capillary force [Fig. 2.9(a)]. The mould and solution are then cured for 2 hours at 65°C. In general the film stripes in Fig. 2.9(b) are defect free, however some edge defects are seen in C (channel width 0.8 μm) since the channels are more difficult to fill when the width decreases. The width of film stripes also tend to be a little smaller than the width of mould channels, and a shrinkage of around 25% was seen after solvent evaporation. The patterned films have same the optical properties as unpatterened films [67].

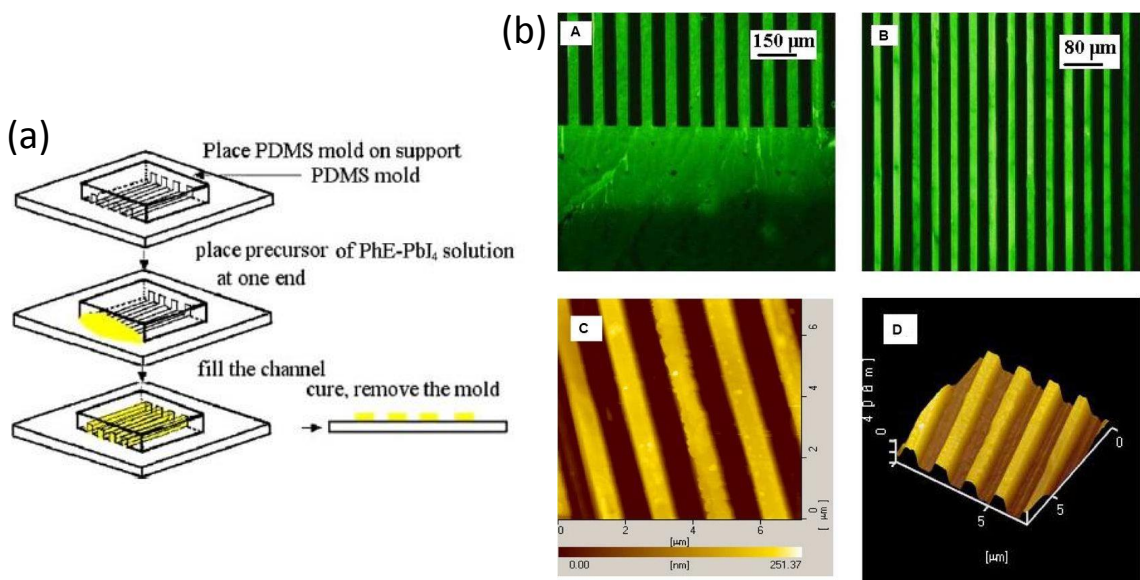


Fig. 2.9 (a) Schematic of MIMIC process for patterning PAPI films. (b) Fluorescent optical micrographs (A,B) and AFM images (C: planar, D: stereo) of patterned PAPI films. In all cases the black stripes represent bare substrate without PAPI. Film stripe widths are A) 50 μm wide, B) 15 μm, C) and D) 0.8 μm. Reproduced from Ref. [67].

2.3.3 Electronic structure

Umebayashi *et al.* calculated the electronic structure of C₄PI and its 3D extension CH₃NH₃PbI₃ using linear combination of atomic orbitals (LCAO) within density functional theory (DFT) [Fig. 2.10(a)] [68]. Both are direct gap semiconductors, but the 2D compound has a higher

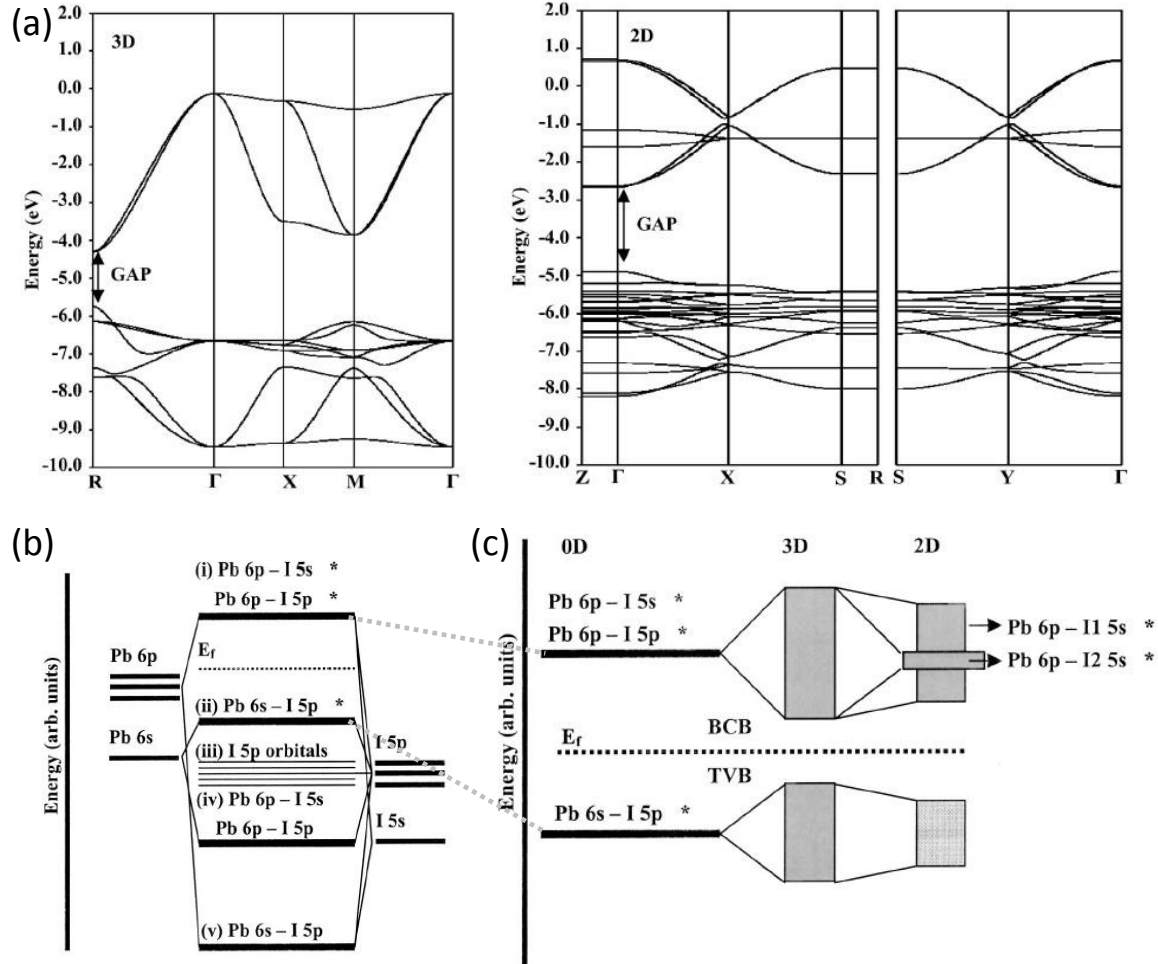


Fig. 2.10 (a) Calculated band structures of $\text{CH}_3\text{NH}_3\text{PbI}_3$ (left) and C_4PI (right) along high symmetry lines in the first Brillouin zone. The band gap is labelled. Bonding diagrams of (b) one PbI_6 octahedron, and (c) extension to $\text{CH}_3\text{NH}_3\text{PbI}_3$ and C_4PI . The bottom of the conduction band (BCB), top of the valence band (TVB), and Fermi energy level (E_F) are labelled. Adapted from Ref. [68].

band gap and narrower bandwidths due to the decreased dimensionality. The 2D band structure also has flatter dispersions at the top of the valence band (TVB) and the bottom of the conduction band (BCB), leading to a larger carrier effective mass, and thus larger binding energy for excitons.

Fig. 2.10(b) shows the bonding diagrams for a single PbI_6 octahedron, as well as the 3D and 2D compounds above. In the 2D crystal the TVB consists of $\text{Pb}(6s)$ and $\text{I}(5p)$ σ -antibonding orbitals, whereas the BCB consists of $\text{Pb}(6p)$ and $\text{I}(5s)$ σ -antibonding orbitals and $\text{Pb}(6p)$ and $\text{I}(5p)$ π -antibonding orbitals (not labelled on figure). The crystal field also lifts the degeneracy between different iodine atoms, so the conduction band with bridging

iodine atoms (I_1) is wider than that with terminal iodine atoms (I_2). In Ref. [69] the BCB was labelled non-bonding from first principles pseudopotential total-energy calculations with the local density approximation, although it still consisted of $Pb(6p)$ and $I(5p)$ orbitals.

2.3.4 Optical properties

Excitons

Excitons are formed due to transitions between the TVB and BCB in the inorganic layers of PbI perovskites. Excitons in $C_{10}PI$ have an energy of around 2.4 eV above 275 K, and the value changes to around 2.55 eV at below 268 K due to a phase transition of the alkylammonium molecules [Fig. 2.11]. The binding energy E_B is calculated from the difference between the exciton peak and the step-like structure (interband transitions) in absorption spectra, and the value of 320 ± 10 meV explains the presence of excitons even at room temperature. Excitons also have a large oscillator strength of around 0.7 ± 0.1 [41]. The above values were for the lowest energy ($n = 1$) free exciton, but bound excitons can also be seen, for example in Fig. 2.11(b) the peak at 2.55 eV is assigned to the lowest free exciton in the inorganic layers, whereas the peak at 2.53 eV decreases in intensity with temperature and is assigned to a shallowly bound exciton. The peaks seen at low temperature at 2.45 eV is sample dependent, and thus assigned to deeply impurity-bound excitons [41]. The Stokes shift for $C_{10}PI$ is less than 5 meV [Fig. 2.11(c)], and this is generally true for PbI-based perovskites (e.g. for $C_{12}PI$ in Ref. [44]). In Refs. [30, 41] both longitudinal and transverse exciton-polaritons are observed in reflection spectra of $C_{10}PI$ at 1.6 K, with a splitting of around 60 meV [41]. The exciton radiative lifetime is 7 ps at 8 K [70].

Polarisation-dependent excitons are seen in the Kramers-Kronig calculated absorption spectra of diammonium ($H_3NC_6H_{13}NH_3$)PbI [Fig. 2.12]. When the incoming light is polarised parallel to the crystallographic \vec{b} axis, the lowest exciton has an energy of 2.5272 eV. Two shoulders seen at 2.566 and 2.718 eV (indicated by small arrows) are due to vibronic bands. The very small peak at 2.819 eV is attributed to $n = 2$ excitons, as determined using exciton activation energies calculated from PL spectra. Due to the monoclinic crystal symmetry, light polarised parallel to \vec{c} can generate excitons polarised to both the \vec{a} and \vec{c} , and as the \vec{a} and \vec{b} directions are very nearly isotropic, the peak at 2.5272 eV (also seen in Fig. 2.12(a)), is attributed to excitons polarised parallel to \vec{a} . The narrow peak at 2.559 eV is due to excitons polarised parallel to \vec{c} , but only appears at very low temperatures as the peak width normally makes the two exciton peaks indistinguishable. The $n = 2$ peak is observed at the same position as in Fig. 2.12(a). The binding energy for the material is calculated to

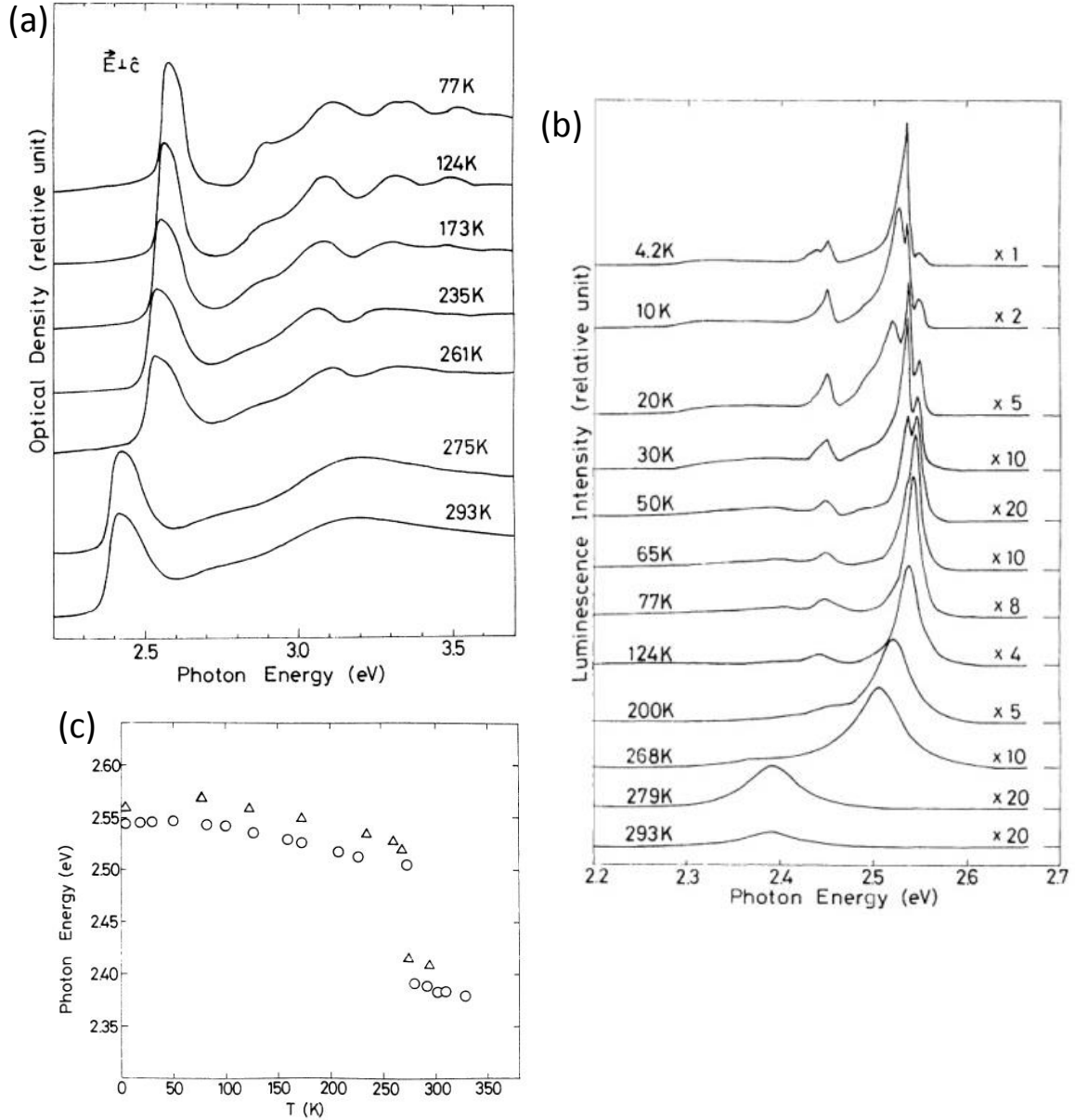


Fig. 2.11 (a) Polarised optical density of $C_{10}PI$ crystal at labelled temperatures (\vec{E} parallel to the QWs). (b) Photoluminescence spectra spectra of $C_{10}PI$. The temperature and scaling of plotted data are labelled. (c) Energies of absorption (Δ) and photoluminescence (\circ) peaks as a function of temperature. Reproduced from Ref. [41].

be 330 meV, and the Bohr radius 8.2 Å[71].

There has been some discussion regarding whether the excitons are Wannier- or Frenkel-like in nature. Xu *et al.* used magneto-optical measurements on polycrystalline $C_{10}PI$ thin films and found that exciton peaks are not shifted when a magnetic field B is applied in the

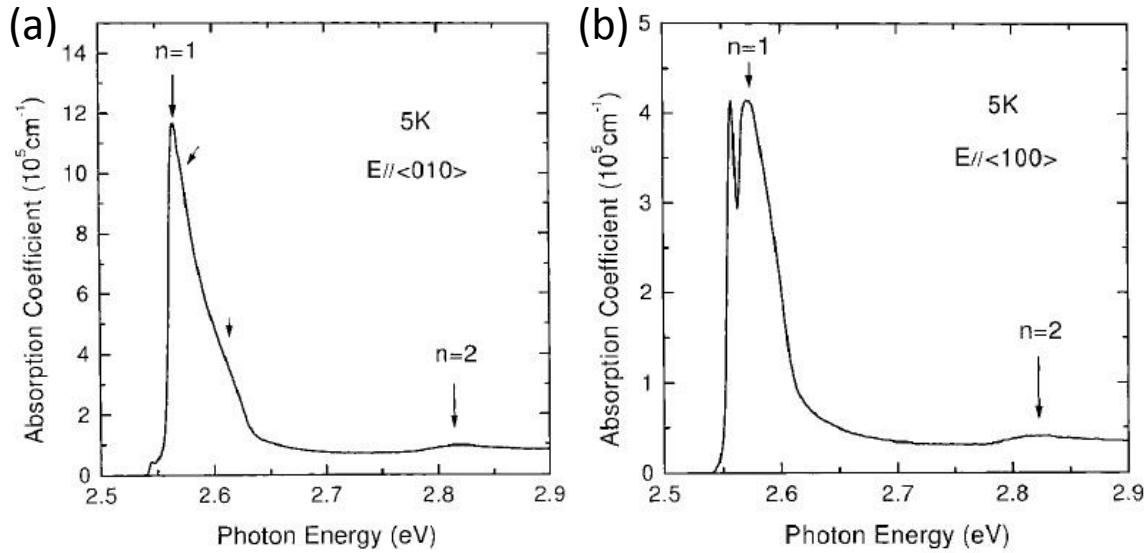


Fig. 2.12 Absorbance spectra for \vec{E} parallel to (a) \vec{b} , and (b) \vec{c} axes for $(\text{H}_3\text{NC}_6\text{H}_{13}\text{NH}_3)\text{PbI}_4$, calculated using Kramers-Kronig relations from reflection spectra. The $n = 1, 2$ peaks are labelled, and arrows indicate vibronic sidebands. Reproduced from Ref. [71].

plane of the QWs, but when the field is applied perpendicular to the QWs the energy of the exciton E changes according to

$$E = E_0 \pm \frac{1}{2}g_{\perp}\mu_BB + c_0B^2, \quad (2.9)$$

where E_0 is the energy of the exciton at zero field, g_{\perp} is the Landé g factor perpendicular to the plane of the film, μ_B is the Bohr magneton, and c_0 is the diamagnetic constant. The sign of the energy shift depends on the polarisation of the magnetic field, and from the data $g_{\perp} \sim 1$, and $c_0 \sim 10^{-7} \text{ eV/T}^2$ for C₁₀PI. From the magneto-absorption measurements the Bohr radius $a_B \sim 12 \text{ \AA}$ of C₁₀PI. The peak shifts indicate C₁₀PI excitons are Wannier-like, since Frenkel excitons would have no extended motion and thus show no energy shift at all. However as the size of each PbI₆ octahedron is around 6 Å [41], excitonic motion extends over only a few octahedra [72].

Magneto-optical measurements on C₆PI produces g_{\perp} and c_0 values similar to those in C₁₀PI, however the authors believed that as the exciton Bohr radius is on the order of Pb-Pb distances in the crystal, the exciton may be better described by a cationic Frenkel model involving orbitals of Pb²⁺. The calculated g_{\perp} and c_0 agrees well with experiment [63]. On the other hand Tanaka *et al.* used electroabsorption and two-photon absorption studies and showed that excitons in thin film C₆PI samples were Wannier-like in nature, with 1s, 2s, 2p, and 3p energies at 2.34, 2.60, 2.61, and 2.64 eV respectively. The Wannier excitons

exhibited strong 2D behaviour, with 1s exciton $E_B = 310$ meV [73].

The band gap of perovskites can be engineered by altering the halogen and metal atoms in the structure. The exciton energy ranges from 2.5 eV for PbI perovskites, to 3.1 eV for PbBr and 3.6 eV for PbCl. Indeed mixed-halide perovskites of the form $(\text{RNH}_3)_2\text{PbA}_x\text{B}_{1-x}$ allow variation within this range [46, 74]. It has been shown that while the change in absorption wavelength generally varies linearly with the halogen concentration x as the process is averaged over excitons at all possible sites, the excitons formed then preferentially diffuse over 10s nm to lower energy halogen atomic sites so emission wavelength does not show the same linear variation with x [75].

Biexcitons and triexcitons

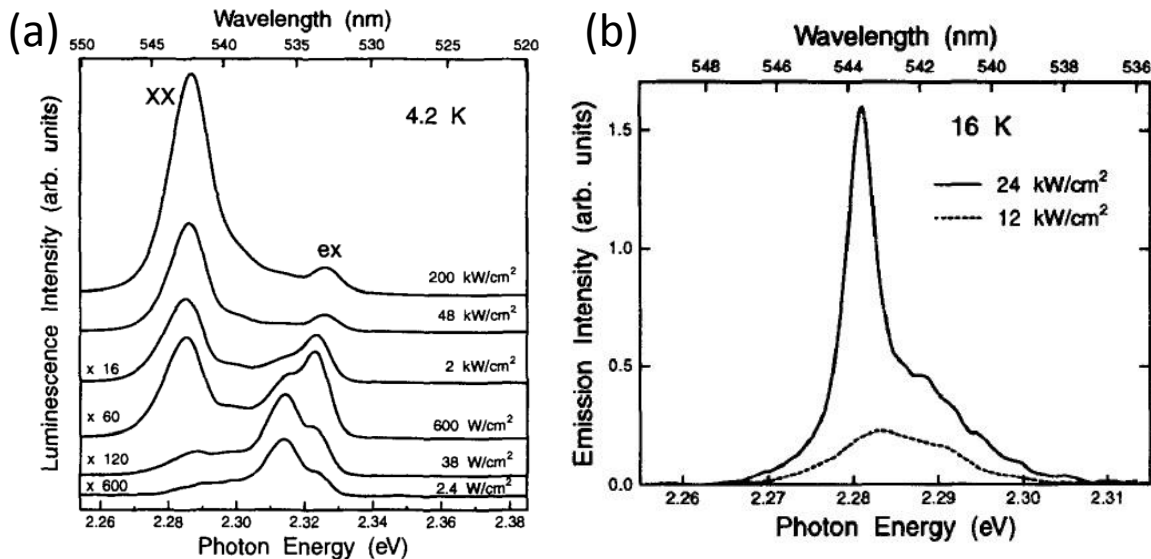


Fig. 2.13 (a) Photoluminescence spectra of C_6PI film excited by 337 nm nitrogen laser at 4.2 K. The excitation intensity and data scaling are given. Exciton (ex) and biexciton (XX) bands are labeled. (b) Emission spectra of C_6PI waveguide above (24 kW/cm^2) and below (12 kW/cm^2) the lasing threshold at 4.2 K. The lasing wavelength is 543.6 nm. Reproduced from Ref. [76].

An increase in excitation power can lead to the formation of bi- or tri-exciton complexes, where two or three free excitons are bound together. Induced photo-carriers screen Coulomb interactions, so strong coupling between carriers is needed to observe triexcitons. Low dimensionality is an advantage as screening has a more limited effect [77]. The radiative decay of biexcitons to transverse excitons has been observed in C_{10}PI , with biexciton binding energy of 50 meV [Fig. 2.13(a)] [78]. By creating a waveguide configuration with

transverse pumping (200 nm C₆PI film spin coated on Ti-containing SiO₂ with Al-mirrors formed on the output faces of the substrate), biexciton lasing was observed in C₆PI. The lasing threshold is 20 kW/cm² at 16 K. Fig. 2.13(b) shows emission spectra above and below the lasing threshold: a broad biexciton band is seen below the threshold, but a sharp peak at 2.281 V is seen above the threshold. The biexciton band is probably isotropic as the emission is not polarised [76].

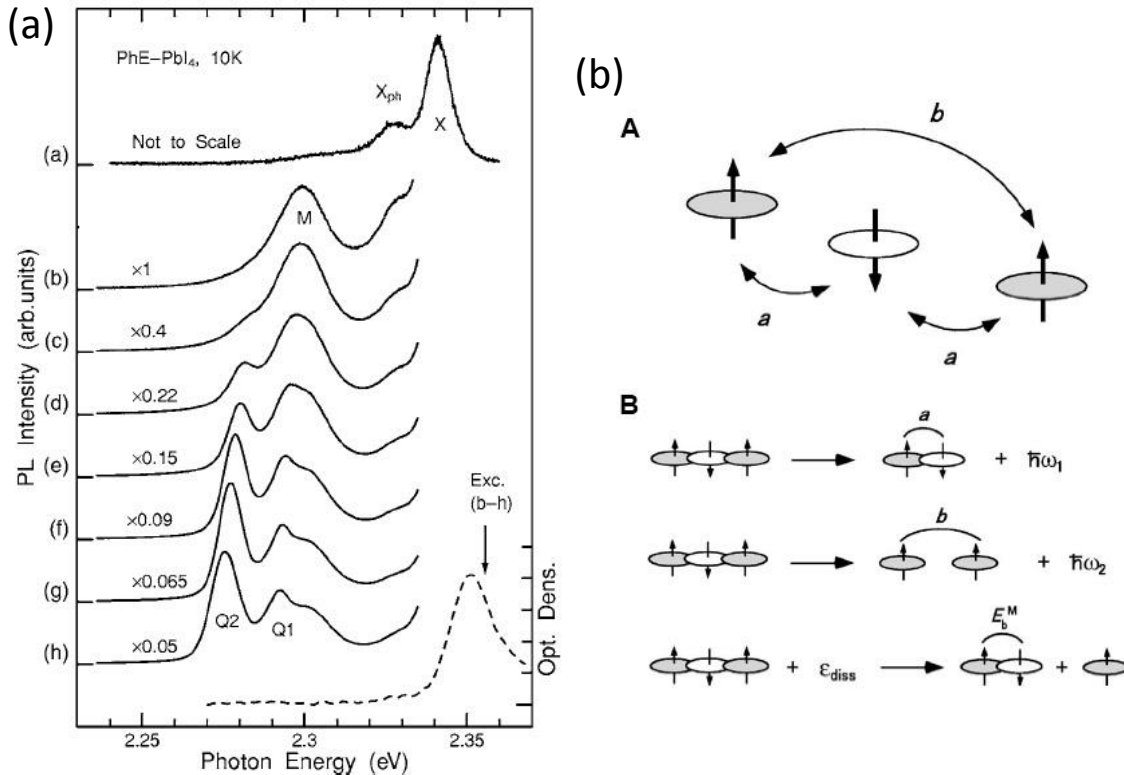


Fig. 2.14 (a) PL spectra of PAPI at different excitation intensities and energies. (a) was excited at 2.58 eV, and (b)-(h) at 2.355 eV. The excitation intensities are (a) 4.6×10^{10} , (b) 4.6×10^{12} , (c) 1.4×10^{13} , (d) 2.8×10^{13} , (e) 4.6×10^{13} , (f) 9.2×10^{13} , (g) 1.6×10^{14} , and (h) 3.2×10^{14} photons cm⁻². The dotted line shows the absorption spectrum. X is the free exciton band, X_{ph} phonon sidebands, M the biexciton band, Q₁ amplified spontaneous recombination of biexcitons, and Q₂ the $\hbar\omega_2$ triexciton process. (b) A) shows the triexciton model, and B) likely dissociation mechanisms. For the meaning of symbols see the main text. Reproduced from Ref.[77].

Shimizu *et al.* observed triexciton formation in the PL spectra of PAPI. In Fig. 2.14(a), the free exciton band is labelled X, phonon sidebands X_{ph}, and the biexciton band M. At higher excitation intensities, two other bands can be seen, labelled Q₁ and Q₂. Q₁ is assigned to the amplified spontaneous emission due biexciton recombination, and Q₂ to a triexciton process. Triexcitons consist of bound states of three spin singlet excitons, with

interaction energy a between opposite spin excitons (< 0), and interaction energy b between same spin excitons (> 0). Likely radiative triexciton dissociation mechanisms are dissociation into a biexciton and photon ω_1 , or two excitons and photon ω_2 . However non-radiative dissociation (energy ϵ_{diss}) into a biexciton (binding energy E_b^M) and an exciton is also possible [Fig. 2.14(b)]. As Q_2 is at a lower energy than M, it can only be due to the ω_2 process, although it is unclear why the ω_1 process is not observed. From the data collected, $a = -37.5 \text{ meV}$, $b = 11 \text{ meV}$, $\epsilon_{\text{diss}} = 14 \text{ meV}$, and $E_b^M = 50 \text{ meV}$ [77].

Dielectric confinement and the image charge effect

Both the binding energy and oscillator strength of (transverse) excitons in 2D PbI perovskites are much larger than those in the inorganic 3D equivalent, PbI₂ [79]. In materials where a QW is sandwiched between barrier layers with lower dielectric constant ϵ_b , three types of confinement affect excitons. Firstly quantum confinement, where the reduction in dimensionality to 2D gives a binding energy four times larger than expected in bulk 3D material [80]. Secondly dielectric confinement, where the lower barrier ϵ_b reduces the effective dielectric constant of the entire structure, thus providing less shielding and giving a higher binding energy E_B . Thirdly mass confinement, where carrier wavefunctions extending into the barrier region lead to a larger effective mass, thus increasing the binding energy. Mass confinement depends on quantum confinement in order to determine how much of the carrier wavefunction is leaked into the barrier region, and generally only has a small effect [81]. The interfaces between layers also act as mirrors which create an infinite series of image charges [Fig. 2.15]. Using carrier wavefunctions which fit the boundary conditions of the well, as well as self and image-charge Hamiltonians, exciton properties can be calculated. The results show that E_B increases if the barrier height decreases, the excitons have larger effective mass in carrier region, or the barrier regions have a smaller dielectric constant [81]. Muljarov *et al.* found that the potentials created due to the image charge effect causes charges in the inorganic layers to be repelled from the interface, whereas charges in the organic layers are attracted to the interface [82].

2.3.5 Influence of organic molecules

How organic molecules fit into the perovskite structure can change the conformation of PbI₆ octahedra, the Pb-I bond angle or the interlayer I-I coupling, all of which lead to a change in the electronic structure [83]. Pb-I-Pb bond angles have the greatest effect on the band gap E_g of perovskites. Experimental results show that bond angles closer to 180°

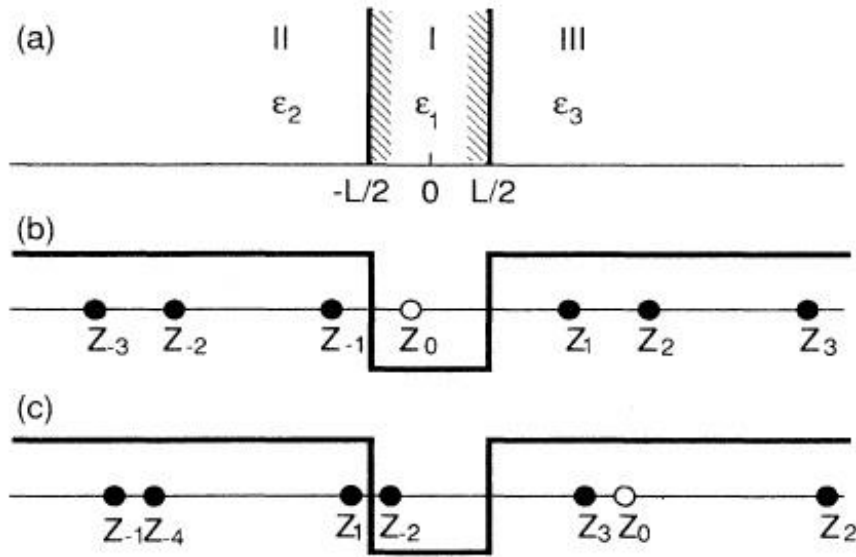


Fig. 2.15 (a) Generalised description of quantum well (region I) and barriers (regions II and III). (b) and (c) show the positions of initial charges (white circle, Z_0) and image charges created (black circles) due to interfaces. In (b) the initial charge is in the well region, whereas in (c) it is in the barrier region. Reproduced from Ref. [81].

(undistorted octahedra) lead to smaller E_g , which agrees with extended Huckel tight-binding calculations used to evaluate band structures of PbI perovskites [Fig. 2.16]. Although E_g is underestimated using this model, the overall correlation between I-Pb-I angle and electronic energy levels are correct [44]. Calculations for Sn-based perovskites show that bond angle distortions in the QW plane have a larger impact on E_g than purely out-of-plane distortions [84]. For this reason, pressure can be used as an external parameter to tune to exciton energy [85].

2,2'-biimidazole ($C_6H_6N_4$) can be incorporated into the perovskite structure to form $(C_6H_8N_4)PbI_4$. The loss of NH_3 groups, as well as the ability to delocalise charge across the organic molecule, leads to weaker hydrogen bonding with inorganic octahedra. Thus the reduced corrugation of QWs produces smaller E_g compared to C_nPI [47]. Similarly in $(HO(CH_2)_2NH_3)_2PbI_4$, the OH group is able to hydrogen bond with neighbouring NH_3 groups or I atoms. The extra interactions weaken the NH_3 -I hydrogen bonds, and also provide a channel for stronger electronic coupling between inorganic layers, leading to smaller E_g [86].

In general perovskites have better PL efficiencies if the QWs are flat. Therefore as well as bonding with functional groups of the organic molecule, the most emissive compounds

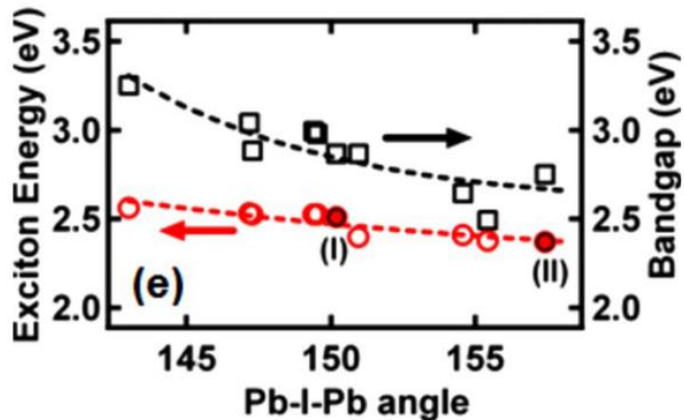


Fig. 2.16 Variations in exciton energy (red) and band gap (black) with Pb-I-Pb angles calculated using extended Huckel tight binding calculations. Data points given are experimentally determined for PbI perovskites, and filled in circles represent PL maxima of labelled C₁₂PI phases. Reproduced from Ref. [44].

are created using relatively flexible molecules whose size allows the formation of the MQW structure without too much deformation of inorganic sheets [35].

As well as structural effects, notable properties of the organic ligand can be incorporated into the perovskite. For example perovskites with chiral molecules also exhibit optical activity [36], while inclusion of chromophores into the structure can lead to charge and energy transfer between the organic and inorganic layers [38, 87, 88].

2.3.6 Applications

Microcavities and photonic crystals

The dynamics of interactions between quasiparticles can be described in two limiting regimes. In the weak coupling limit the system can still be described by the original quasiparticle wavefunctions, albeit with some perturbations. In the strong coupling limit, coherent interactions between quasiparticles lead to the formation of mixed states that oscillate between the original eigenstates with frequency Ω_R (Rabi frequency, also a measure of the interaction strength). The new mixed states can combine properties of both the original particles. For example, strong coupling between excitons and cavity photon modes create exciton-polaritons, quasiparticles with small effective mass but capable of nonlinear interactions, have shown great promise in producing Bose-Einstein condensates [89], low-threshold lasers [90] and ultrafast switches [91].

Strong coupling has been observed between PAPI excitons and cavity modes in a dis-

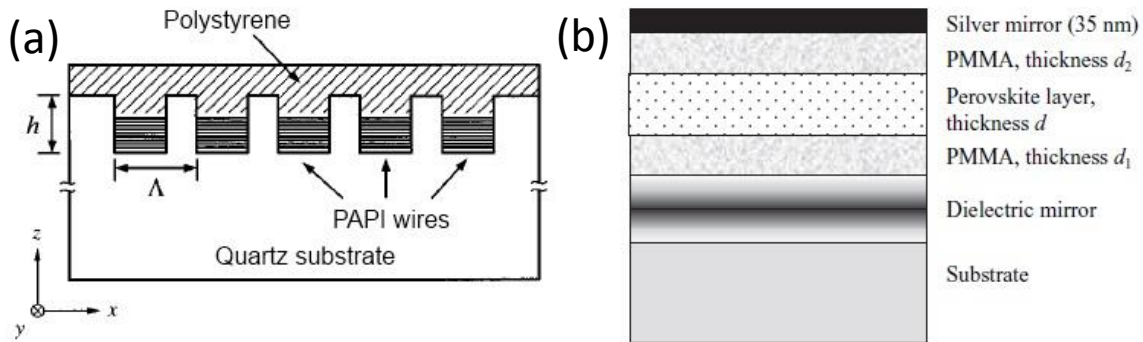


Fig. 2.17 Schematic of (a) a distributed feedback microcavity, (b) Fabry-Perot microcavity. (a) reproduced from Ref. [92], (b) from [93].

tributed feedback microcavity at room temperature [92, 94, 95]. The cavity consists of a structured quartz substrate with PAPI spin coated into the spaces to form parallel wires, and an overcoat of polystyrene added to prevent the degradation of PAPI films [Fig. 2.17(a)]. Samples are formed over $1.5 \times 1.5 \text{ mm}^2$ with cavity height $h = 300 \text{ nm}$ and PAPI thickness 30 nm [94]. When the incident beam is at normal incidence, PAPI excitons and fourth order cavity resonance become resonant, couple strongly and form new eigenstates (cavity polaritons). Using a variety of grating pitches Γ from 0.62 to $0.72 \mu\text{m}$, transmission spectra showed that the upper and lower polariton branches exhibit anticrossing behaviour, as expected for strongly coupled modes. Due to the large exciton oscillator strength, the mode splitting is around 100 meV , an order of magnitude larger than the 9 meV observed in GaAs systems in Fabry-Perot microcavities [92]. A strong enhancement of PL intensity of the lower branch polariton is seen if the standing wave cavity mode is in resonance with PAPI excitons, in this case when $\Gamma = 0.68 \mu\text{m}$ [94]. No signature of the upper polariton branch is seen as in thermodynamic equilibrium the upper branch would expect to be less populated, however the polariton lifetime may not be long enough for equilibrium to occur. Other suggestions have included a relaxation of the upper branch polaritons towards uncoupled excitonic states, or fast emission of photons between the upper and lower polariton branches [93]. It is thought that PAPI rods oscillating in phase due to strong coupling with cavity modes at resonance would lead to a macroscopic polarisation and ultrafast resonance, however the polariton lifetime is actually 8 ps longer with a grating structure at 40 K . It is possible that this is due to excitons with large wave vectors that cannot couple to the outside without the help of the grating reciprocal lattice vector [95]. Strong coupling between excitons and 2D grating modes has also been observed in PAPI with Rabi splitting 100 meV [96].

Strong coupling between cavity and PAPI exciton modes are also observed in the Fabry-Perot microcavities [Fig. 2.17(b)] [93, 97]. By adjusting the position of the perovskite layer in the microcavity, the coupling between exciton and photon modes can be controlled, and the splittings seen were between 130-190 nm. Similar CHPI microcavities constructed produce splittings of 130 meV for a $5\lambda/4$ metal-air microcavity, and of 160 meV for a $7\lambda/4$ metal-metal microcavity [28].

Strong exciton-photon coupling has also been observed in a photonic crystal of 256 nm diameter microspheres infiltrated with PAPI (silica opal) [98]. A face centred cubic lattice of silica microspheres with 3D channel voids is created, and a solution of PAPI and DMF introduced into continuous spaces through capillary forces [Fig. 2.18(a)]. Angle-dependent reflectivity spectra of the structure with PAPI filling fraction $f_{\text{PAPI}} = 0.06$ clearly demonstrates anticrossing behaviour, indicating strong coupling between the stop band (photon mode) of the photonic crystal and the exciton mode of PAPI, with Rabi splitting 240 meV [Fig. 2.18(b)]. However there is an uncoupled exciton mode that seems largely unaffected by the photon mode, possibly due to some of the bulk PAPI on the surface of the silica opal remaining, or an open photonic gap in the silica opal that leads to insufficient photon confinement and limits exciton-photon coupling.

Optoelectronic devices

The processability of perovskites from solution and their high PL efficiencies make perovskites attractive for optoelectronic devices, particularly electroluminescent (EL) devices. Era *et al.* used a layered structure consisting of PAPI, an indium-tin-oxide (ITO) anode, MgAg cathode, and oxadiazole (OXD7) electron transport layer [Fig. 2.19(a)]. When the device is driven, electrons in OXD7 are injected smoothly into the PAPI layer as there is no energy barrier, but holes injected into PAPI will remain at the PAPI/OXD7 interface due to the barrier potential [Fig. 2.19(b)]. Electrons and holes are therefore trapped in the PAPI layer, and recombine to provide luminescence. When driven at liquid nitrogen temperatures, the EL intensity reaches a luminescence of more than 10000 cdm^{-2} at a current density of 2 Acm^{-2} and voltage of 24 V. The emission peak at 520 nm has narrow bandwidth, and is very similar to the PL spectrum. However the EL efficiency at room temperature is much smaller than that at liquid nitrogen temperatures, and is mainly caused by thermal ionisation of excitons [99]. Similar devices made by Matsushima *et al.* [Fig. 2.19(c)] show that an additional buffer layer (OTS=octadecyltrichlorosilane, CuPc=Cu phthalocyanine) can reduce the hole-injection barrier between ITO and PAPI, leading to an increase in EL efficiency. Buffer layers that decrease PAPI film roughness will also reduce leakage current [100].

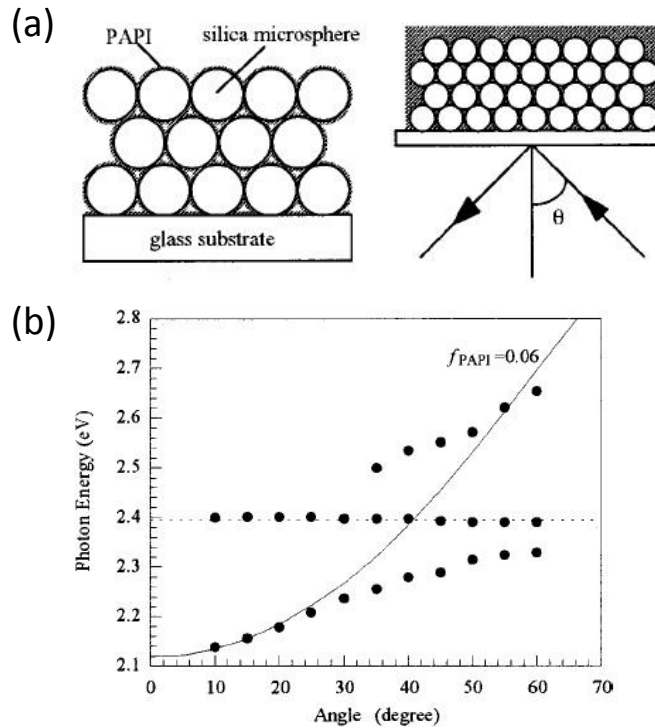


Fig. 2.18 (a) Structure of the silica opal infiltrated with PAPI film formed on a glass substrate. θ , the angle of incident light, is also shown. (b) Extracted mode positions from angle-dependent reflectivity spectra (black circles) for opal with PAPI filling fraction $f_{\text{PAPI}} = 0.06$. Exciton energy (dashed line) and theoretical photonic crystal stop gap (solid line) are marked. Reproduced from Ref. [98].

Hattori *et al.* made EL devices shown in Fig. 2.19(a) using PAPI, PBPI ($(\text{C}_6\text{H}_5\text{C}_4\text{H}_8\text{NH}_3)_2\text{PbI}_4$) and CHPI. As before the EL and PL of all three compounds are almost identical [Fig. 2.20(a)], however despite PBPI and CHPI having higher PL efficiencies than PAPI [Fig. 2.20(b)], the PBPI device had the lowest external quantum efficiency η_{ext} (number of emitted photons/number of electrons) and CHPI the highest. The PBPI device is also much more resistive than the others, with current density around two orders of magnitude less than other devices at same voltage. Both the resistance and the low EL efficiency are likely due to the longer alkyl chain preventing carrier transport. The external efficiency of the CHPI device is comparable to the highest efficiency reported in EL devices reported at the time [101].

Although there have not been many studies on the transport properties of 2D PbI perovskites, 2D SnI structures are semiconducting, while the 3D SnI perovskite is a low-carrier density p-type metal [102]. Thin film transistors have also been produced from 2D SnI perovskites, with carrier mobilities of up to $1.4 \text{ cm}^2/\text{Vs}$, better than that of amorphous silicon, with on-off ratio > 1000 and current densities $> 400 \text{ A/cm}^2$ [103–105].

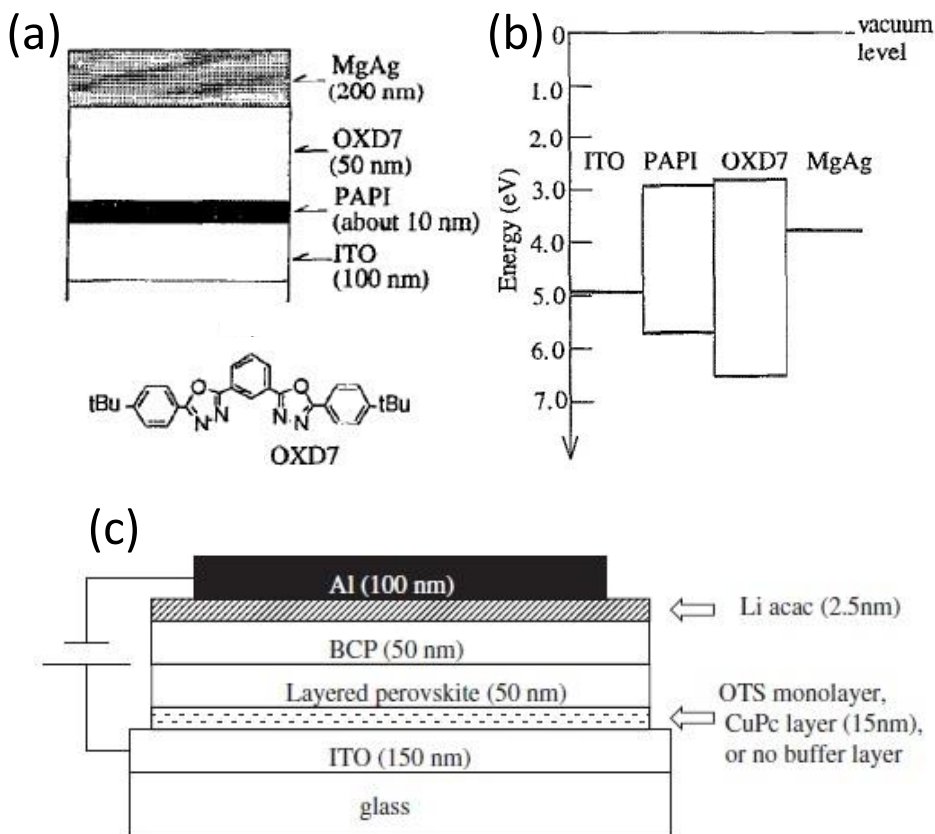


Fig. 2.19 (a) Schematic of EL device with PAPI by Era *et al.* (top) and the molecular structure of OXD7 (bottom). (b) Energy level diagram of the EL device in (a). (c) Schematic of the LED made using PAPI by Matsushima *et al.*. (a-b) reproduced from Ref.[99], (c) from [100].

Scintillators

Scintillators convert radiation energy into photo-emission for the purpose of detecting ionising radiation. They need to have a short luminescence decay time constant in order to react quickly, high resistance to radiation damage, and high efficiency so that a suitable number of photons are created per unit radiation energy of absorbed [106]. Many efficient scintillators (e.g. NaI:TI, CsI:Na) have decay times of 200 ns or more, whereas fast scintillators (e.g. BaF₂, CsF) have low light yields of less than 2000 photons per MeV [107]. C₆PI crystals are bombarded by an ultra-short electron beam with pulse width of 1-2 ps, generated by a 35MeV linear accelerator, and produced a decay constant of 45 ps at room temperature [107]. Investigations show 2D perovskites have faster decay times than their 3D counterparts as quantum confinement provides carrier wavefunction overlap and higher likelihood of decay.

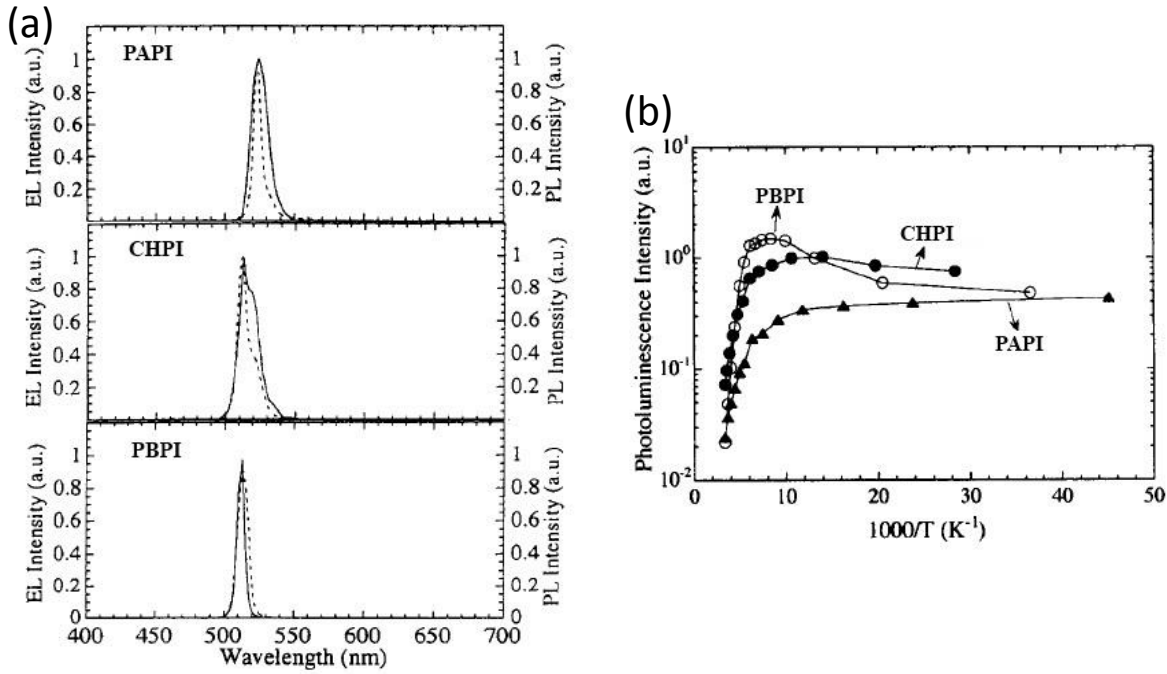


Fig. 2.20 (a) EL (solid lines) and PL (dotted lines) spectra of the labelled perovskite at 110 K. EL device structure is shown in Fig. 2.19(a). (b) Integrated PL intensity of CHPI, PAPI, and PBPI thin film samples as a function of temperature. Reproduced from Ref. [101].

Shibuya *et al.* used different dosages of 2 MeV protons to test $\approx 250\text{nm}$ thick C₆PI thin films [106]. Radiation-induced emission spectra show no shift in the exciton peak position during bombardment, and no additional peaks appeared at any radiation dosage. Three decay components are found: one with decay constant 0.39 ns due to free exciton recombination, then two defect density dependent components with constants of 3.8 and 16 ns due to trapped excitons, with decay constants depending on defect density. Emission intensities of C₆PI excitons attenuated with increased radiation, but the radiation hardness is still enough for practical use. From these results, C₆PI is a good candidate for scintillator use due to the stability of excitons at room temperature, ease of processing, fast response time, spectrum stability to radiation, and inclusion of high atomic number element (Pb) in order to detect low energy transfer radiation such as X-rays [108].

2.4 Conclusions

Excitons, bound hydrogen atom-like systems of electrons and holes, produce strong optical signatures in semiconductors, and many exciton effects are enhanced by a reduction

in dimensionality. 2D hybrid organic-inorganic perovskites are naturally self-assembling materials that create a MQW structure, whose room temperature optical properties are dominated by the excitons produced in the inorganic layers. Their band gaps can be tuned across the visible and near-UV by substitution of inorganic elements. PbI perovskite excitons have wavelength ~ 500 nm, and binding energy in excess of 200 meV as a result of quantum and dielectric confinement. The perovskite structure is very flexible and can accommodate a range of organic molecules that influence the optical and electronic properties of the material. High exciton oscillator strength make such systems ideal for the creation of new stages at room temperature via strong coupling, while their processability from solution make these materials of interest for optoelectronic devices.

Chapter 3

Plasmonic nanostructures

3.1 Introduction

Surface plasmons are collective electron oscillations in a metal. The form of such oscillations can be found by solving Maxwell's equations, and depends on the geometry of the problem. Such movement of electrons causes large field enhancement, and the resonance frequency is very sensitive to the dielectric environment around the metal. In this Chapter we will solve Maxwell's equations to find the form of plasmon oscillations at a metal-dielectric interface, before exploring how the solution is affected by modifying the metal surface to form a grating. Finally we will explore plasmon oscillations in small metal islands.

3.2 Surface plasmon polaritons

In order to describe the behaviour of electrons in a metal, we can use Maxwell's equations to describe the behaviour of electromagnetic fields:

$$\nabla \cdot \vec{D} = \rho \quad (3.1a)$$

$$\nabla \cdot \vec{B} = 0 \quad (3.1b)$$

$$\nabla \times \vec{E} = -\frac{\partial \vec{B}}{\partial t} \quad (3.1c)$$

$$\nabla \times \vec{H} = \vec{J} + \frac{\partial \vec{D}}{\partial t}. \quad (3.1d)$$

These equations link the fields \vec{D} (dielectric displacement), \vec{E} (electric field), \vec{H} (magnetic field) and \vec{B} (magnetic flux density). The electric charge density is given by ρ , and electric

current density by \vec{J} . For linear, isotropic and non-magnetic materials we have the relationships

$$\vec{D} = \epsilon \epsilon_0 \vec{E} \quad (3.2a)$$

$$\vec{B} = \mu \mu_0 \vec{H}, \quad (3.2b)$$

where ϵ_0, μ_0 are the permittivity and permeability of free space respectively, and ϵ, μ are the relative permittivity and permeability of the material in question. In the case of a non-magnetic medium $\mu = 1$, and the refractive index n is given by $\sqrt{\epsilon}$.

By combining Eqs. (3.1c, 3.1d) and assuming a harmonic time dependence to the electric field with frequency ω such that $\vec{E}(\vec{r}, t) = \vec{E}(\vec{r})e^{-i\omega t}$, we find the Helmholtz equation

$$\nabla^2 \vec{E} + k_0^2 \epsilon \vec{E} = 0, \quad (3.3)$$

where $k_0 = \frac{\omega}{c}$ is the wavevector of the wave in vacuum.

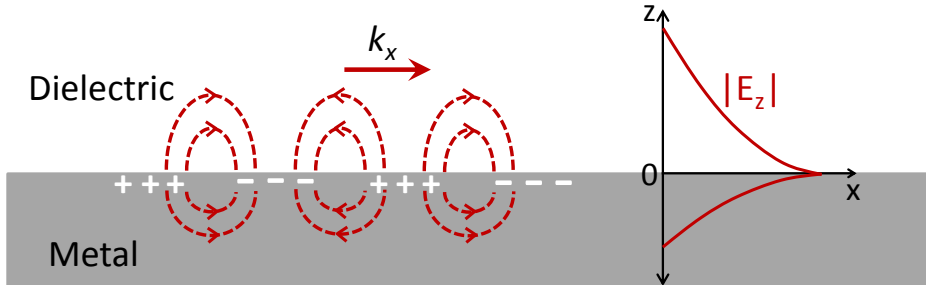


Fig. 3.1 Schematic for SPP oscillations at a metal-dielectric surface, showing the evanescent nature of such plasmons.

Using the geometry of a metal-dielectric interface shown in Fig. 3.1, we look for solutions of waves propagation in the x direction but confined to the interface with evanescent decay in the z direction, such that $\vec{E}(x, y, z, t) = \vec{E}(z) e^{ik_x x}$ where k_x is the propagation constant of the wave. We find one set of solutions that is transverse electric (TE) polarised, with the \vec{E} -field component perpendicular to the direction of travel:

$$H_x = i \frac{1}{\omega \mu_0} \frac{\partial E_y}{\partial z} \quad (3.4a)$$

$$H_z = \frac{k_x}{\omega \mu_0} E_y \quad (3.4b)$$

$$\frac{\partial^2 E_y}{\partial z^2} + (k_0^2 \epsilon_i - k_x^2) E_y = 0. \quad (3.4c)$$

For both solution the subscript i refers to the material the wave is travelling in, d or m for the dielectric and metal respectively. The solutions are waves of the form $e^{ik_xx}e^{k_iz}$, i. e. a wave travelling in x direction that evanescently decays in the z direction. Applying the boundary conditions of E_y and H_x continuity across the metal-dielectric interface, we find the condition

$$A(k_m + k_d) = 0, \quad (3.4)$$

where A is the amplitude of wave in the metal halfspace. Since confinement requires $\text{Re}(k_m, k_d) > 0$, Eq. 3.4 is only fulfilled if $A = 0$ when no wave can be sustained in the metal. The boundary condition indicate similarly the amplitude of the wave must be 0 in the dielectric as well, thus no SPPs exist in TE polarisation.

The transverse magnetic (TM) polarised solution, with the \vec{H} -field component perpendicular to the direction of travel, is:

$$E_x = -i \frac{1}{\omega \epsilon_i \epsilon_0} \frac{\partial H_y}{\partial z} \quad (3.5a)$$

$$E_z = -\frac{k_x}{\omega \epsilon_i \epsilon_0} H_y \quad (3.5b)$$

$$\frac{\partial^2 H_y}{\partial z^2} + (k_0^2 \epsilon_i - k_x^2) H_y = 0. \quad (3.5c)$$

Here continuity of H_y and $\epsilon_i E_z$ across the interface requires

$$\frac{k_d}{k_m} = -\frac{\epsilon_2}{\epsilon_1}, \quad (3.4)$$

so we require $\text{Re}[\epsilon_1]$ and ϵ_2 to be of opposite signs, thus SPPs can only be sustained on a metal-insulator interface. Fulfillment of Eq. 3.5c leads to

$$k_m^2 = k_x^2 - k_0^2 \epsilon_m \quad (3.5a)$$

$$k_d^2 = k_x^2 - k_0^2 \epsilon_d. \quad (3.5b)$$

Combining this with Eq. 3.4 produces

$$k_x = k_0 \sqrt{\frac{\epsilon_m \epsilon_d}{\epsilon_m + \epsilon_d}}, \quad (3.6)$$

the dispersion relation of an SPP on a metal-dielectric interface. Fig. 3.2(a) shows the calculated dispersion using a free electron gas model for the metal-air SPP, with values taken from Ref. [109]). In this model there is no damping in the metal, i. e. $\text{Im}(\epsilon_m) = 0$. Note three

regions in the graph: at high frequencies above the plasma frequency of the electron gas ω_p we have the transparent region (k_x, k_i real) where radiation can penetrate into the metal and excite plasmon polaritons. At low frequencies we have bound surface modes (k_x real, k_i imaginary), and at large k_x the frequency tends to $\omega_{sp} = \frac{\omega_p}{1+\epsilon_d}$. In this limit the plasmons are stationary surface plasmons, and $\epsilon_m + \epsilon_d = 0$. For $\omega_{sp} < \omega < \omega_p$ no propagating modes exist (k_x imaginary). If damping is included in the metal model, then quasi-bound modes can exist in this intermediate region [Fig. 3.2(b), calculated using values for Ag from ?]. Note also damping introduced a finite maximum k_x for the SPP, leading to a finite propagation length $L_x = \frac{1}{2\text{Im}(k_x)}$, typically on the order 10-100 μm at visible wavelengths for Au/Ag [110]. The limit in k_x also produces an upper limit in k_i [Eq. 3.5], thus limiting the skin depth $L_z = \frac{1}{\text{Im}(k_i)}$ to order 10 nm in metals.

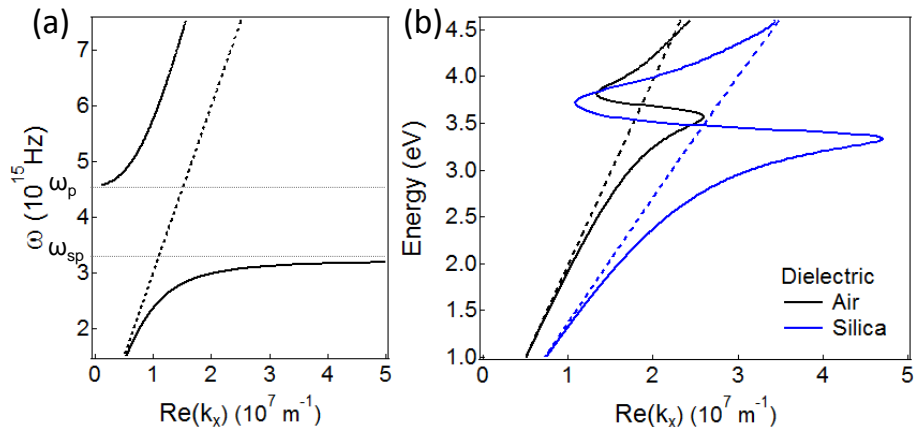


Fig. 3.2 Dispersion of SPPs on metal-dielectric interface for (a) free electron gas and (b) silver (solid lines), and light lines in the dielectric (dashed lines).

3.3 Plasmonic gratings

From Fig. 3.2 we can see that the SPP dispersion always lies on the right of the light line in the dielectric, and this momentum mismatch means that it is not possible to directly excite SPPs using photons. Instead we must use a phase matching technique, for example prism or grating coupling. In prism coupling a three-layer system is employed, so that photons reflected at the higher refractive index interface has sufficient momentum to excite SPPs on the interface between the metal and the lower refractive index material. In grating coupling, due to its periodicity D the grating structure can provide momenta of $G_m = \frac{2\pi m}{D}$, thereby allowing photons to couple to SPPs. However other types of modes can be observed in the

optical spectra of plasmonic gratings.

3.3.1 First order modes

Using Huygens' construction and considering each point on the grating as a wave scatterer, we reach the well-known grating equation for constructive interference

$$D(\sin \alpha - \sin \beta) = l\lambda, \quad (3.7)$$

where α is the angle of incidence and β the diffracted angle with respect to the grating normal, λ is the wavelength of light and l the order of the diffracted light [Fig. 3.3(a)]. From here we only consider the zeroth diffraction order (i. e. specular reflection) with incidence angle θ and azimuthal angle ϕ . In the order approximation, where we assume different types of diffracted light do not interact, we can distinguish between two types of gratings modes: ‘photonic’ modes caused purely by interference of light due to the periodic structure, and ‘plasmonic’ modes where SPPs are excited on the surface of the grating. We can find the dispersion of such grating modes by considering momentum and energy conservation of incoming/outgoing photons, and thus find

$$k_m = k_i^2 \sin^2 \theta + G_m^2 \pm 2k_i G_m \sin \theta \cos \phi, \quad (3.8)$$

where the label m indicates the order of grating vector G_m needed for matching. Here the wavevector of the incident light

$$k_i = \frac{\omega}{c} \sqrt{\epsilon_d}, \quad (3.9a)$$

for photons

$$k_m = \frac{\omega}{c}, \quad (3.9b)$$

and for SPPs

$$k_m = \frac{\omega}{c} \sqrt{\frac{\epsilon_m \epsilon_d}{\epsilon_m + \epsilon_d}}. \quad (3.9c)$$

In this case the grating can be thought of as a 1D photonic grating, where the photon/SPP dispersions are displaced by multiples of the grating vector. Although in the first order photonic and plasmonic modes do not interact with each other, SPP modes can strongly couple and create anticrossings in the spectra [111].

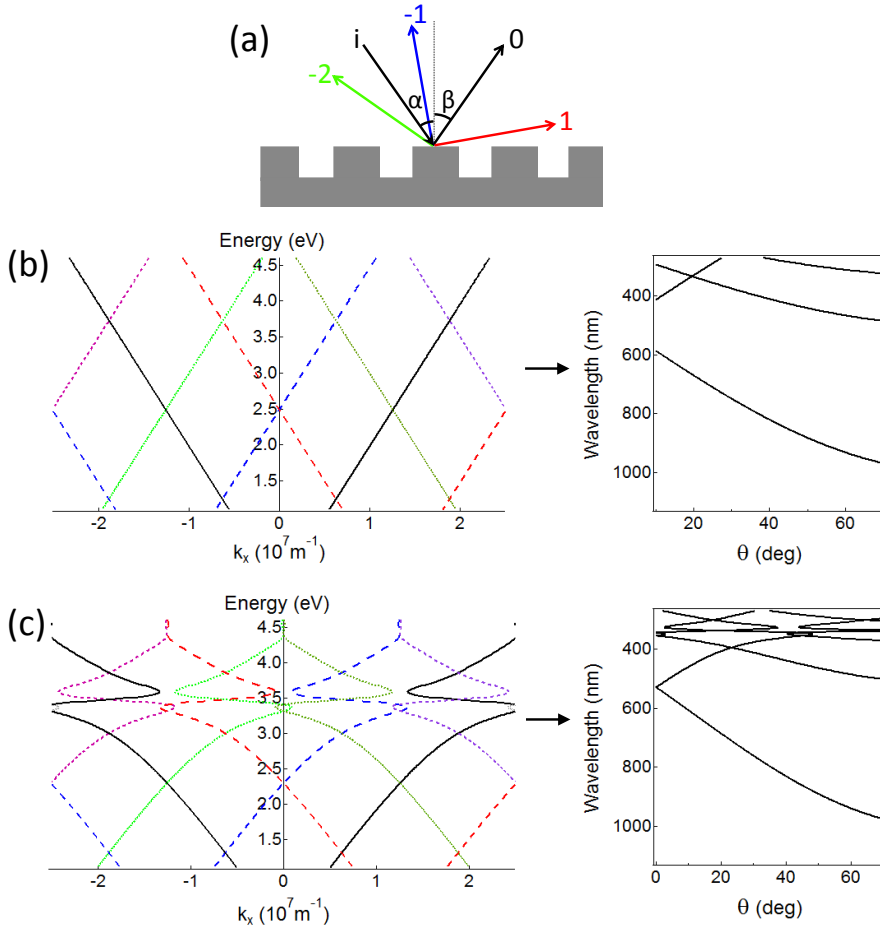


Fig. 3.3 (a) Diffraction from a 1D grating structure, showing the incident light and diffracted orders. Dispersion (left) and modes as a function of incidence angle θ (right) for (b) photonic and (c) plasmonic modes for specularly reflected zeroth order mode for a $D = 500$ nm grating.

3.3.2 Grating anomalies

Anomalies are sharp changes in the response of a grating, and first observed by Wood, who noted “that under certain conditions the drop from maximum illumination to maximum...occurred within a range of wave-lengths not greater than the distance between sodium lines” [112]. Anomalies are second order effects, where different diffracted modes interact with each other. The effect is named after Wood, and in plasmonic gratings occurs as a sharp increase in intensity followed by a dip [Fig. 3.4]. Although overall the Wood’s anomaly is one physical phenomenon, it is possible to separate into two parts for a more intuitive understanding: the threshold (sharp change in intensity) and resonance (dip) anomalies.

The threshold anomaly is a photonic effect, and comes about when an order is diffracted

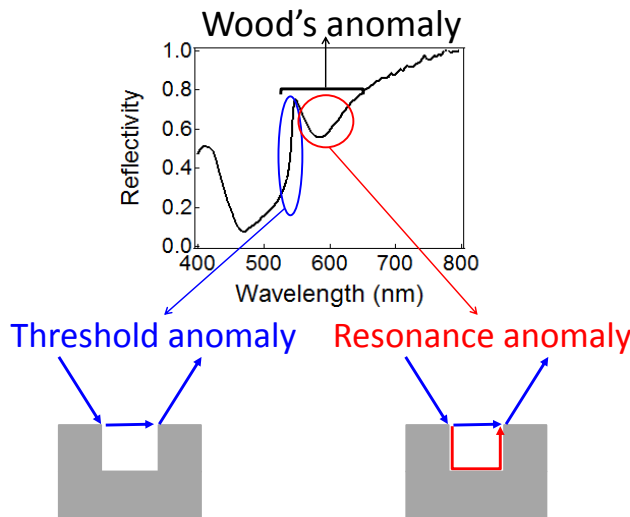


Fig. 3.4 Wood's anomaly in the reflectivity of Ag grating, $D = 417$ nm. Schematics of the threshold and resonance anomalies are included.

along the surface of the grating ($\beta = 90^\circ$). If an order becomes evanescent then the energy available will be redistributed to the other diffractive orders, thus this ‘passing’ order on the edge between diffraction and evanescence leads to a sharp change in the diffraction intensity. These effects are still due to interference from grating structure, and thus occur at the predicted first order photonic modes [Eq. 3.7]. The threshold anomaly can be observed in both polarisation, but generally the strength of the anomaly (i. e. the change from maximum to minimum intensity) is smaller in TE polarisation, particularly in metals, as the E -field is parallel to the grating lines in this case and thus cannot be sustained. The reduction in field intensity leads to less energy to redistribute, hence the effect is less pronounced.

The resonance anomaly is a plasmonic effect, and comes from the excitation of surface waves on the grating. The excited SPPs can interact with the diffractive light, and the addition of the SPP oscillator and background photonic diffracton leads to a Fano resonance, giving the typical peak-trough feature seen. Clearly the resonance anomaly can only be observed when SPPs are excited, e. g. for $\phi = 0$ in TM polarisation, but not TE. Unlike the threshold anomaly, the position and linewidth of the resonance anomaly dip cannot be predicted by Eq. 3.7 as it depends on the nature of the SPP, and is thus sensitive to the geometry of the grating and any surface roughness in the material [Fig. 3.5]. However it is possible to calculate the position of the resonance anomaly by using electromagnetic theory to model the grating (see Refs. [113, 114] and references therein).

Grating anomalies have been observed in both reflection and transmission gratings, and are responsible for the extraordinary transmission observed for some 1D and 2D arrays

[115–121]. Overcoating of a metallic grating affects the strengths and positions of anomalies, in particular the resonance anomaly, where the SPP is very sensitive to the local dielectric environment. In addition, light can excite modes in the coating material, and thus change the direction of the E -field so that anomalies can be excited when they’re not predicted to, e.g. $\phi = 0^\circ$ in TE polarisation [113, 114].

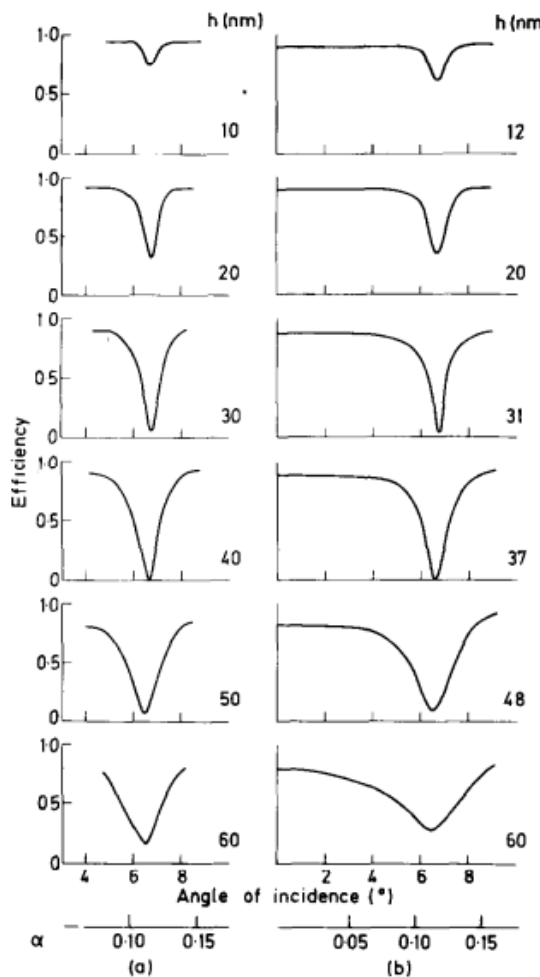


Fig. 3.5 Dependence of resonance anomaly on the grating depth h for sinusoidal grating, $D = 556$ nm at $\lambda = 647$ nm from (a) electromagnetic theory and (b) experiment. Reproduced from Ref. [122].

3.3.3 Localised and guided modes

Gratings can also give rise to optical modes that do not rely on the periodicity of the structure. In particular the grating slits can be thought of as independent, sustaining modes that

do not couple to modes in nearby slits. We can think of the slits as hollow electromagnetic waveguides, and thus support modes that fit the equation [123] [CHECK JACKSON]

$$\frac{\omega^2}{c^2}(n_{eff}^2 - \sin^2 \theta) = \pi^2 \left(\frac{\mu^2}{a_{eff}^2} + \frac{v^2}{b_{eff}^2} \right), \quad (3.10)$$

where n_{eff} is the effective refractive index experienced by the mode in the grating slit, a_{eff} is the effective width and b_{eff} half the effective height for the mode, and μ, v are indices used to label the waveguide mode. Due to the penetration depth of the electromagnetic field in metals, a_{eff} is not the same as the geometric width of the grating slit, and particularly if there is a coating on the metal then a_{eff} and b_{eff} both have some dependence on n_{eff} .

Surface plasmons travelling down the grating slits can interact, particularly if the slit is narrow. In this case we can form symmetric and antisymmetric combinations of the SPP oscillations, essentially forming a metal/insulator/metal waveguide [110]. For rectangular shaped slits, often known as trench waveguide, the highest E -field intensity is often at the top corners of the slits [Fig. 3.6(a)] and thus more extended outside the groove [124–126]. If the groove is V-shaped, the change in effective refractive index due to the change in width leads to reflections, and the highest E -field is localised at the bottom of the grooves [Fig. 3.6(a)] and such oscillations are called channel plasmon polaritons [124, 125, 127? , 128]. Due to their localised nature, the dispersion of such modes is often flat with respect to the angle of incidence θ . Such channel plasmon polaritons can be observed in near-field optical microscopy [Fig. 3.6(b)], and show interference with the light scattered by the structure.

3.4 Localised surface plasmons

3.4.1 Quasi-static approximation

For spherical nanoparticles (NPs), if the diameter $d \ll$, the phase of the E -field is approximately constant across the particle, and we can solve the simplified problem of a sphere in an electrostatic field and include the harmonic time dependence of the field at the end. The geometry is shown in Fig. 3.7(a), with a homogeneous metal particle of diameter d at the origin inside a dielectric medium, and $\vec{E}_0 = E_0 \vec{z}$. Solving the Laplace equation for the

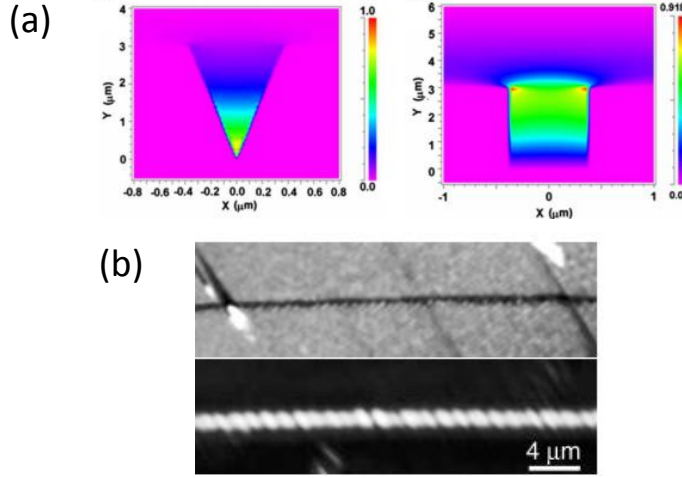


Fig. 3.6 (a) E -field profiles of channel plasmon polariton modes in a V-shaped (left) and trench (right) Au groove, with width $3.75 \mu\text{m}$ and depth $3 \mu\text{m}$ filled with air. (b) Topographical (top) and near-field optical (bottom) images for V-shaped Au slit with width $0.6 \mu\text{m}$ and depth $1 \mu\text{m}$ at $\lambda = 1440 \text{ nm}$. Reproduced from Refs. [124, 125].

potential Φ ($\vec{E} = -\nabla\Phi$), we find

$$\Phi_{in} = -\frac{3\epsilon_d}{\epsilon_m + 2\epsilon_d} E_0 r \cos \theta \quad (3.11a)$$

$$\Phi_{out} = -E_0 r \cos \theta + \frac{\epsilon_m - \epsilon_d}{\epsilon_m + 2\epsilon_d} E_0 \left(\frac{d}{2}\right)^3 \frac{\cos \theta}{r^2} \quad (3.11b)$$

at a distance r from the centre of the sphere, where Φ_{in} and Φ_{out} represent the potentials inside and outside the sphere respectively. Note Eq. 3.11b appears to be the superposition of the applied field E_0 and that of a dipole located at the origin. In this case we can see that the applied field induces a dipole moment \vec{p} in the NP, and also introduce the polarisability α such that

$$\vec{p} = 4\pi\epsilon_0\epsilon_d \left(\frac{d}{2}\right)^3 \frac{\epsilon_m - \epsilon_d}{\epsilon_m + 2\epsilon_d} \vec{E}_0 \quad (3.12a)$$

$$\alpha = 4\pi \left(\frac{d}{2}\right)^3 \frac{\epsilon_m - \epsilon_d}{\epsilon_m + 2\epsilon_d}. \quad (3.12b)$$

A resonance in α is achieved when

$$\epsilon_m(\omega) = -2\epsilon_d(\omega), \quad (3.13)$$

known as the Frölich condition, and provides the resonance frequency of the dipole LSP for a metallic NP. For a free electron gas in air, this condition is achieved at $\omega = \frac{\omega_0}{\sqrt{3}}$, but as can be seen from Eq. 3.13 the position is very sensitive to the dielectric environment around the particle. If harmonic time independence is included, we can see the resonance is caused by an oscillation of electrons in the NP, and as such causes a large field enhancement around the vicinity of the particle [Fig. 3.7(b)]. The LSP resonance also depends on the dielectric function of the metal, and for the same d the Ag resonance is always higher in energy than Au [Fig. 3.7(c)]. Note also the asymmetric shape of the Au Np extinction, which is due to the onset of interband transitions in Au. For arrays of NPs, the resonance frequency in optical spectra is the same as single NPs if the particles are separated by more than $\approx 2d$ [129].

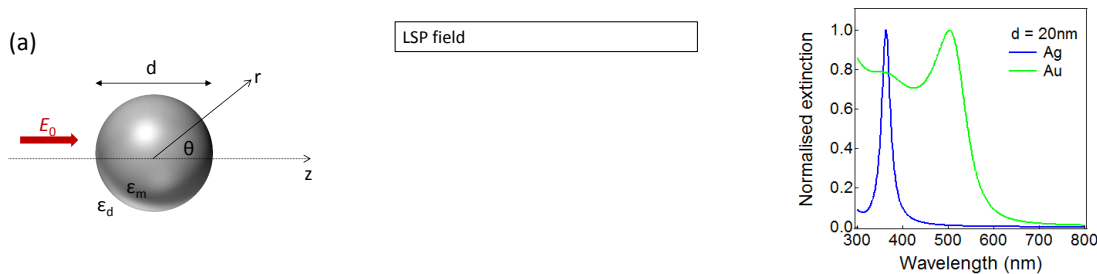


Fig. 3.7 (a) Geometry of homogeneous metal sphere with diameter d placed inside an electrostatic E -field. (b) E -field profile of dipole LSP. (c) Normalised extinction spectra for $d = 20$ nm Ag/Au NPs in air.

The oscillating NP dipole leads to radiation, and can be seen as the scattering of light from the NP. The maximum in polarisability also leads to a resonant enhancement of the scattering C_{scat} and absorption C_{abs} cross section of the particle

$$C_{scat} = \frac{k^4}{6\pi} |\alpha|^2 = \frac{8\pi}{3} k^4 \left(\frac{d}{2}\right)^6 \left| \frac{\epsilon_m - \epsilon_d}{\epsilon_m + 2\epsilon_d} \right|^2 \quad (3.14a)$$

$$C_{abs} = k \text{Im}[\alpha] = 4 \left(\frac{d}{2}\right)^3 \text{Im} \left[\frac{\epsilon_m - \epsilon_d}{\epsilon_m + 2\epsilon_d} \right], \quad (3.14b)$$

and we define extinction $C_{ext} = C_{scat} + C_{abs}$. For very small NPs absorption dominates over scattering due to its d^3 dependence, for example for $d = 30$ nm Ag NPs the extinction is almost entirely due to absorption [Fig. 3.8], while the reverse is true for $d = 90$ nm.

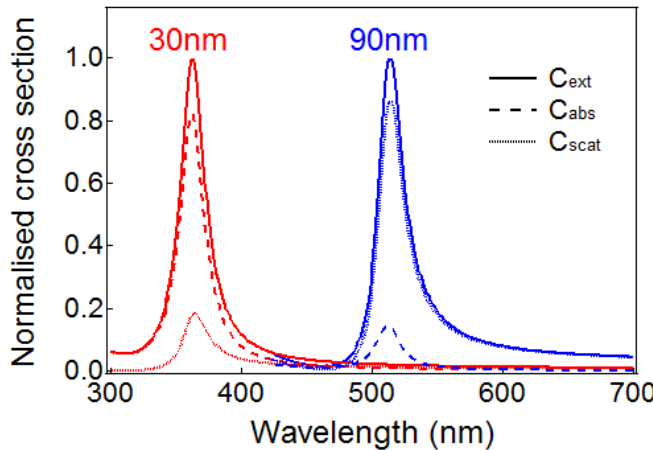


Fig. 3.8 Absorption (dashed lines), scattering (dotted lines) and extinction (solid lines) cross sections for Ag NPs $d = 30$ and 90 nm at $\lambda = 500$ nm in air according to Eq. 3.14, normalised so that the peak extinction is 1. The $d = 90$ nm data has been shifted for clarity.

3.4.2 Size and shape effects

The quasi-static approximation models the NP as an electric dipole whose resonance frequency depends purely on the relative dielectric functions of the metal and surrounding medium. The underlying assumption that the phase of the E -field across the particle is constant is only true for very small particles, and works well for $d < 50$ nm Ag particles [Fig. 3.9]. For larger particles an electrodynamic must be used, for example Mie theory [110?] [CHECK BORN WOLF], where the E -field waves are expanded into a superposition of partial waves (normal modes) that are spherical harmonics/radial components of Hertz vectors, and boundary conditions are used to find the absorption and scattering coefficients required. The normal modes are used in order to solve Maxwell's equations for a sphere interacting with an incoming plane wave. This method produces the redshift in LSP dipole resonance with d as seen in experiment [Fig. 3.9], and also shows the emergence of higher order multipole modes for large particles. For example in Ag particles, a quadrupole mode can be excited and is first observed as a shoulder in the extinction spectrum for $d = 90$ nm.

The resonance of NPs is also very sensitive to the shape of the particle, and both quasi-static and Mie theory calculations can be adapted to the boundary conditions of non-spherical geometry. This provides great tunability to the LSP resonances via controlling of particle shape. Deviations from spherical geometry leads to the production of multiple redshifted peaks [Fig. 3.10(a)]. In the case of nanorods, we observe two LSP resonance in the spectra for unpolarised light: a transverse mode associated with electron oscillations along

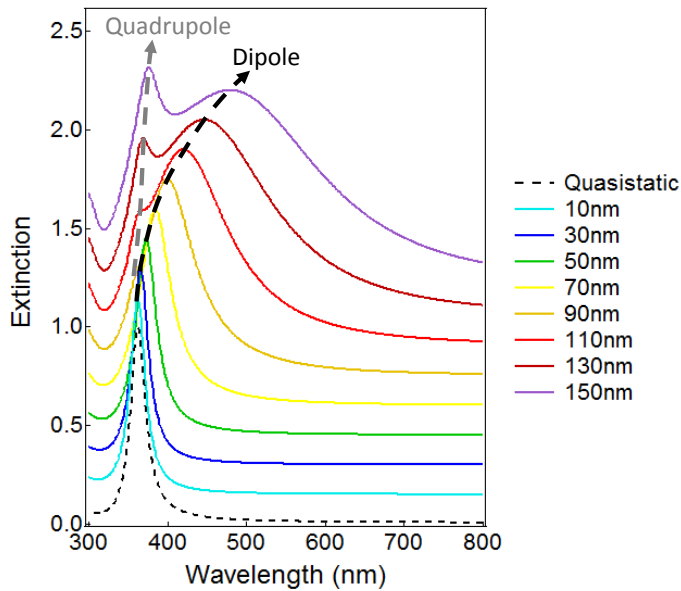


Fig. 3.9 Extinction for NPs with labelled d in air using Mie theory, normalised to the dipole maximum and offset for clarity. The quasi-static approximation resonance is added for comparison.

the short axis, and a longitudinal mode related to electron oscillations along the long axis, the resonance of which depends on the aspect ratio of the nanorod [Fig. 3.10(b)]. Therefore the longitudinal resonance can be tuned through a large range of the electromagnetic spectrum via the growth and assembly of such nanorods [130–132].

3.5 Conclusions

Surface plasmons are collective oscillations of electrons in a metal. Such oscillations show resonant in many geometries, either guided in 2D structure such as planar metal films, or localised 0D nanoparticles. The resonance frequency depends on the relative dielectric functions of the metal and surrounding dielectric, and is very sensitive to the geometry of the nanostructure. Surface plasmons cause large electric field enhancement around the vicinity of the metal, and can thus be used as a sensor. In periodic nanostructures, zone-folding allows incoming/outgoing light to reach parts of the plasmonic dispersion that may not be accessible otherwise, and the interaction between electrons and photons gives rise to many possible modes.

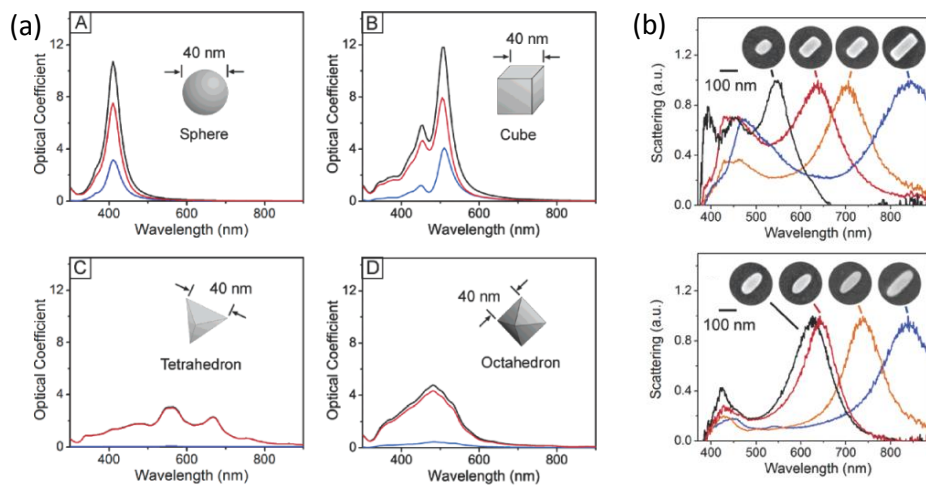


Fig. 3.10 (a) Discrete dipole approximation calculations of the extinction (black), absorption (red) and scattering (blue) of Ag nanoparticles with the geometries shown. (b) SEM images and normalised scattering spectra of individual Ag nanobar (top) nanorice (bottom) structures. Reproduced from Refs. [130, 131].

Chapter 4

Thin films of lead iodide perovskites

4.1 Introduction

Spin coating is a simple process which can be used to fabricate thin films on relatively flat substrates. After a solution is deposited, the substrate is accelerated to its desired final spin speed and continues rotating to remove excess solution. As the solvent evaporates the material self-assembles to form a solid film. The process is commonly used in industry as it can controllably produce films from nm to μm thickness, covering areas with diameter $\sim 10\text{ cm}$, while the thickness and morphology of films depend on solution concentration, spin speed and substrate preparation. In this Chapter I will explore the formation of spin coated C₁₂PI and CHPI thin films.

4.2 Spin coating theory

Although spin coating is experimentally simple, it is complicated to model due to the large number of factors involved. Initially, fluid inertia and surface tension are important as the fluid front spreads out in spiral waves. Evaporation also begins at this point, and a small boundary layer is formed at the liquid-gas interface. At the end of this step a thin and even film forms on the substrate, and fluid inertia is no longer important. In the next phase a balance between viscous and centrifugal forces causes fluid flow and thinning. The boundary layer in the solution gradually gets thicker, so that the solute concentration varies throughout the film thickness. Viscosity rises throughout as a result of solvent evaporation, eventually inhibiting further flow. Further fluid loss is caused by solvent evaporation, which dominates thinning in the latter stages, and eventually solute concentration becomes uniform through-

out the film. There is also a small atmospheric boundary layer above the solution that can influence heat and mass transfer, as well as exert shear forces at the interface [133–135]. The initial acceleration may also affect final film thickness, as too slow an acceleration can lead to complete solvent evaporation before the final spin speed is reached [136].

Meyerhofer used a model where the solvent evaporation was negligible until the mass loss due to rotational forces fell to the level of the evaporation rate, and calculated that

$$h_f \sim C_0(1 - C_0)^{-1/3} \omega^{-2/3} \left(\frac{\eta_0}{\rho_0} \right)^{1/3} e^{-1/3}, \quad (4.1)$$

where h_f is the final film thickness, C_0 the initial solution concentration, ω the spin speed, η_0 the initial viscosity, ρ_0 the initial solution density, and e the evaporation rate [133]. van Hardeveld used a similar model, except the evaporation was modelled more rigorously in terms of rate of mass transfer at the interface, and calculated that the amount of material deposited was

$$m = C_0 \sqrt[3]{\frac{3\eta e}{2\rho \omega^2}}, \quad (4.2)$$

where m is the amount of material deposited in the final film [134]. The rate determining step for solvent evaporation is found to be mass transfer in the vapour phase, when the evaporation rate is proportional to $\omega^{1/2}$. This relationship was verified experimentally by both Meyerhofer and van Hardeveld [133, 134] such that $h_f \sim \omega^{-1/2}$. The dependence of the final film thickness on initial solution concentration is more complicated as η_0 and ρ_0 will also depend on concentration. Lawrence's model considered both the solvent and atmospheric boundary layers, and found that

$$h_f \sim C_0 \left(\frac{\eta_0}{\rho_0} D_0 \right)^{1/4} \omega^{-1/2}, \quad (4.3)$$

where D_0 is the initial solvent diffusivity [135].

Taking into account evaporation, all three models above agree that $h_f \sim \omega^{-1/2}$, but experimentally other values have been found (for example -0.68 and -0.8, see Ref. [135]). Lawrence indicated that an exponent of ω less than -0.5 could be due to films that had not completed the full spinning process, and was thus thicker than the calculations indicated. Shear thinning, where the viscosity of the solution decreases with an increased shear stress, may also be responsible [135].

4.3 Experimental methods

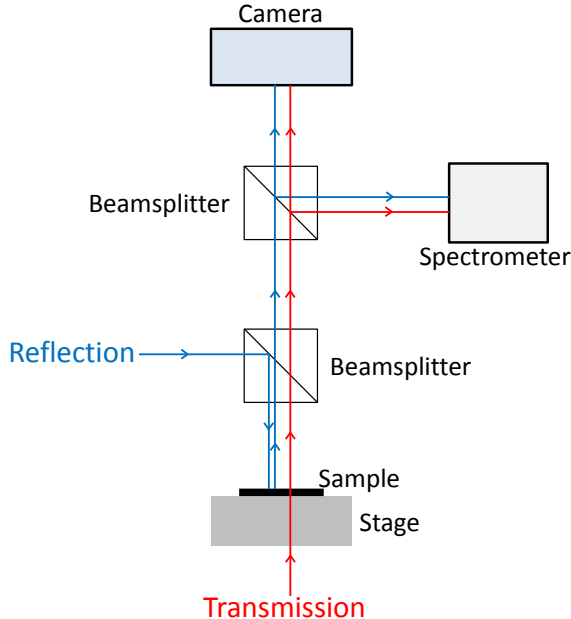


Fig. 4.1 Schematic of optical microscopy and spectroscopy setup, including the reflection and transmission beam paths.

Spin coating solutions are prepared by dissolving a chemically synthesised perovskite powder [Sec. 2.3.2] in tetrahydrofuran (THF) with a concentration of 20mg/ml. Silica substrates are sonicated in a four-step process for approximately 15 minutes per step: firstly a deionised water and detergent solution, then deionised water, acetone, and finally isopropanol. Three additional substrate preparation techniques are investigated in order to create the most uniform films: (1) CO₂ snowjetting, where a high velocity mix of gaseous and solid carbon dioxide is focused on and substrate, cleaning the surface as a result of the momentum transfer and solvent action of CO₂ [137]. (2) Silanisation, where substrates are dipped in a 2 vol% solution of aminopropyltriethoxy silane (APTES) in dry acetone for approximately 90 minutes. A self-assembled monolayer of silane molecules forms on the substrate, and in the case of APTES the surface is functionalised with amine groups. (3) Plasma etching, where substrates are treated using a Diener Electronic Femto plasma system for 5 minutes, using an oxygen plasma to clean contaminants on the substrate. The surface is then functionalised with hydroxyl groups and becomes more hydrophilic. Perovskite films are characterised using optical microscopy and spectroscopy (collection spot diameter $\approx 20\ \mu\text{m}$ unless otherwise specified) [Fig. 4.1], and the film thickness determined by AFM measurements on a scratched area of the film.

4.4 C₁₂PI thin films

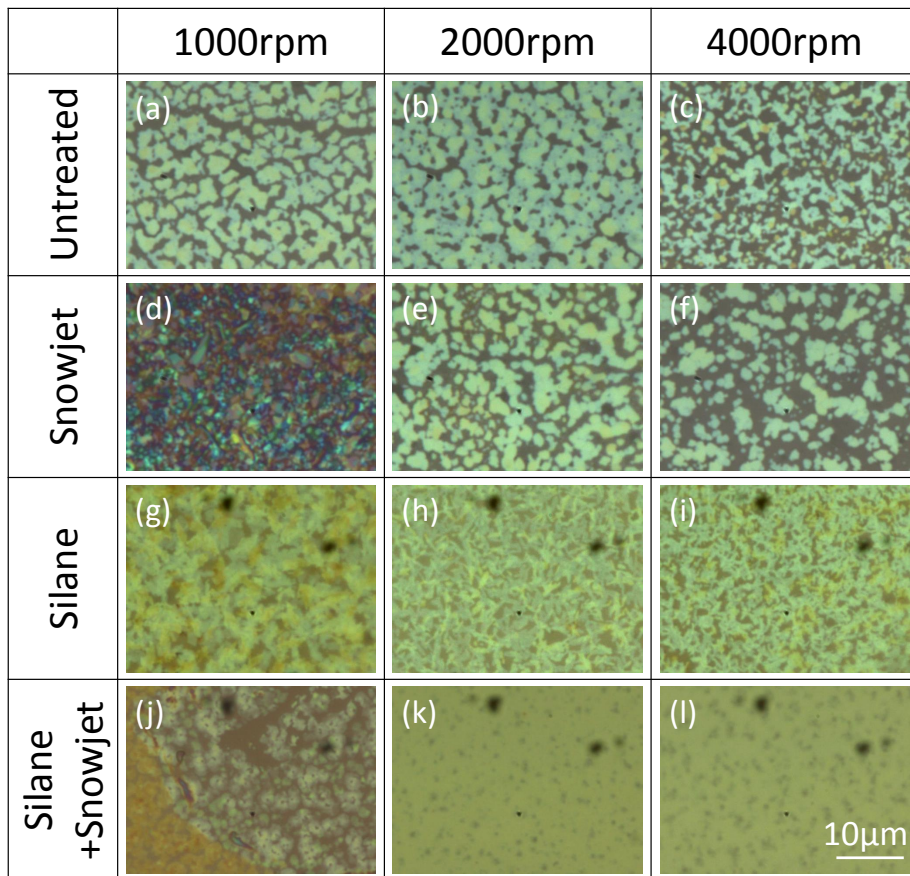


Fig. 4.2 BF images at 100× magnification of spin coated C₁₂PI films, with spin speed and substrate preparation as labelled. Note the substrate was heated for (d) only.

Bright field (BF) images of C₁₂PI films at 100× magnification are shown in Fig. 4.2. Due to the hydrophobic nature of the organic molecule, C₁₂PI films show significant dewetting without functionalisation of the substrate [Figs. 4.2(a-f)], and for this reason no films are formed on plasma etched substrates. The non-uniform film in Fig. 4.2(d) does not exhibit such dewetting as the substrate was heated before application of the C₁₂PI solution, thus the solvent evaporated before excess fluid could be removed by the centrifugal force. Silanisation increases interactions between the constituents of C₁₂PI and the substrate, thereby improving film coverage [Figs. 4.2(g-i)]. Indeed a further snowjet step removes excess APTES that may have remained after silanisation, reducing roughness and producing the most uniform C₁₂PI samples [Figs. 4.2(j-l)].

4.4.1 Spin speed

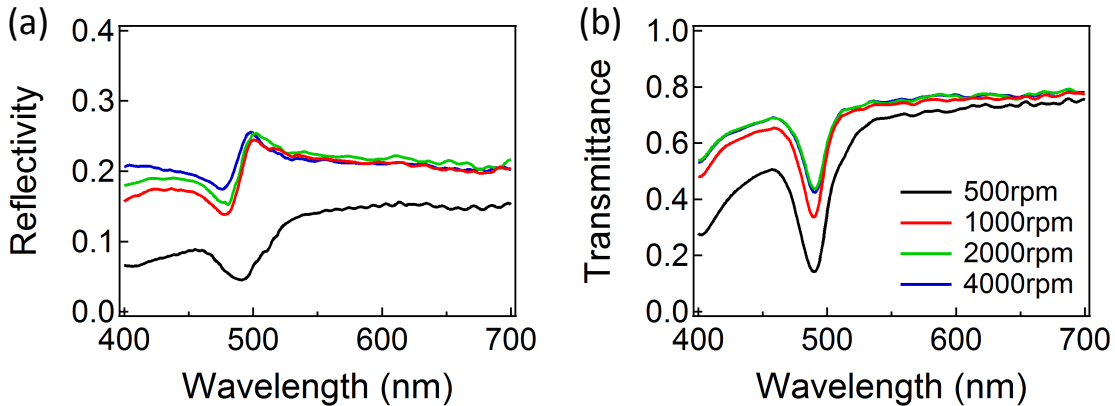


Fig. 4.3 (a) Reflection and (b) transmission spectra for C₁₂PI films on silanised glass substrates made using a variety of spin speeds.

Optical spectra of C₁₂PI films created on silanised substrates illustrate the general trends seen for all substrate preparations [Fig. 4.3]. The exciton appears as a Fano resonance at 490 nm in reflectivity due to interference between its narrow resonance and the continuum background, while a dip appears in the transmittance spectra. Although both phases of C₁₂PI are observed for films below 2000 rpm, here we consider only the high energy exciton. Spectra can be directly correlated to the images taken, hence increased roughness observed in 500 rpm films translates to a lowering of the overall reflectivity. In the same way, comparable morphologies of films made above 1000 rpm [Figs. 4.2(g-i)] lead to almost identical spectra. As C₁₂PI is a multilayer system, the size of the exciton dip in transmission spectra can be used as a gauge of the film thickness, and from Fig. 4.3(b) we see that the film thickness decreases with spin speed as expected.

4.4.2 Substrate preparation

Optical spectra of 4000 rpm C₁₂PI films made using a variety of substrate preparation techniques are shown in Fig. 4.4. The reflectivity spectra are almost identical for all substrate preparations [Fig. 4.4(a)], with the exception of the silanised substrate where excess APTES molecules led to increased surface roughness, thus favouring the more crumpled and higher energy C₁₂PI phase. Removal of the excess silane via snowjetting removes such roughness, creates flatter inorganic sheets and the lower energy exciton. Dewetting of C₁₂PI films on non-functionalised substrates produces an increase in the film transmittance away from the exciton resonance [Fig. 4.4(b)].

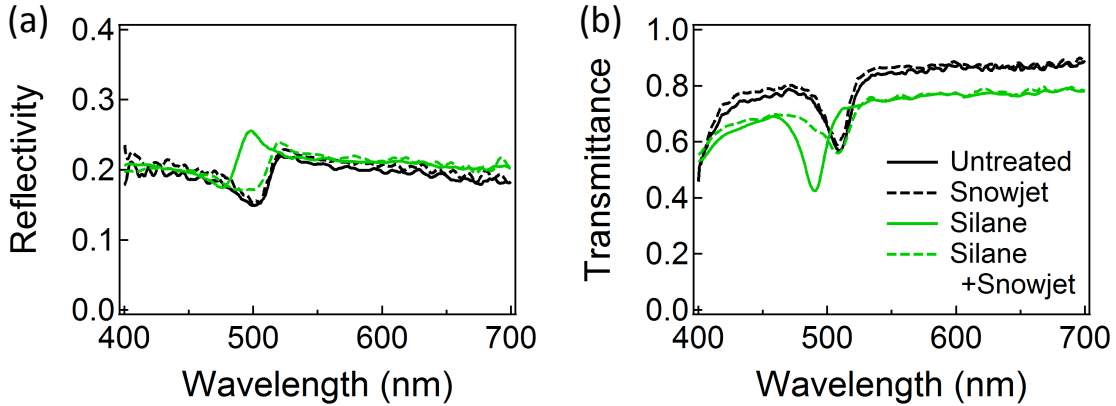


Fig. 4.4 (a) Reflection and (b) transmission spectra for 4000 rpm $C_{12}PI$ films made using a variety of substrate preparation techniques.

4.4.3 Sample degradation

BF images at $100\times$ magnification of 2000 rpm $C_{12}PI$ films as-made (left) and after one week in standard conditions (right) are shown in Fig. 4.5. All films show signs of dewetting or diffusion, highlighting the importance of placing C_nPI films in a low humidity atmosphere or capping with a polymer layer (e. g. Ref. [44]) to prevent sample degradation due to humidity.

4.5 CHPI thin films

BF images of CHPI films at $100\times$ magnification are shown in Fig. 4.6. No dewetting was observed with CHPI due to increased hydrophilicity of the organic molecule. Both snowjetting and high spin speeds improved the uniformity of samples [Figs. 4.6(a-f)], however the best films were produced with silanised substrates, regardless of spin speed [Figs. 4.6(g-l)]. A similar effect was seen in plasma etched substrates [Figs. 4.6(m-r)].

4.5.1 Spin speed

Optical spectra of CHPI films created on untreated or silanised substrates are shown in Fig. 4.7, with the exciton resonance at 506 nm. For untreated substrates, a noticeable difference in the spectra between 2000 and 4000 rpm indicates a change in morphology: at low spin speeds increased film roughness produces lower overall reflectivity, and the appearance of a higher energy exciton in reflectivity leads to an increase in the linewidth of the transmission dip [Figs. 4.7(a,b)]. Such extra resonances have been observed in thick perovskite films (> 120 nm), attributed to stacking faults, strain and structural misalignment in

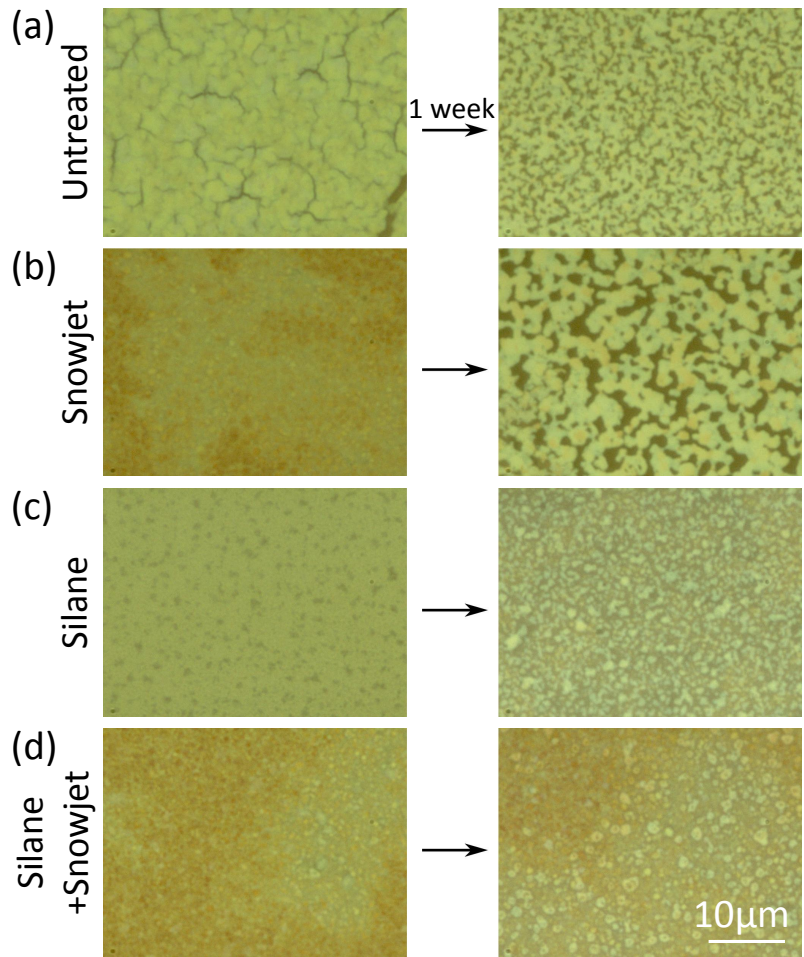


Fig. 4.5 Degradation of 2000 rpm C₁₂PI thin films shown in 100× magnification BF images. Images of the sample were taken as-made (left), and after one week in standard conditions (right).

the structure [62]. In contrast, as expected from their BF images [Fig. 4.6(g-i)] the spectra for silanised substrates exhibit the same features at all spin speeds [Figs. 4.7(c,d)], the main difference being a change in the amplitude of the exciton resonance as a result of the film thickness. Film thickness measurements for around 10 films made using untreated substrates give $b = 0.45 \pm 0.01$ when fit to $a\omega^{-b}$ [Fig. 4.7(e)], close to the $\omega^{-0.5}$ relationship predicted by theory.

4.5.2 Substrate preparation

Optical spectra of 2000 rpm CHPI films made using a variety of substrate preparation techniques are shown in Fig. 4.8. The appearance of a second exciton due to structural mis-

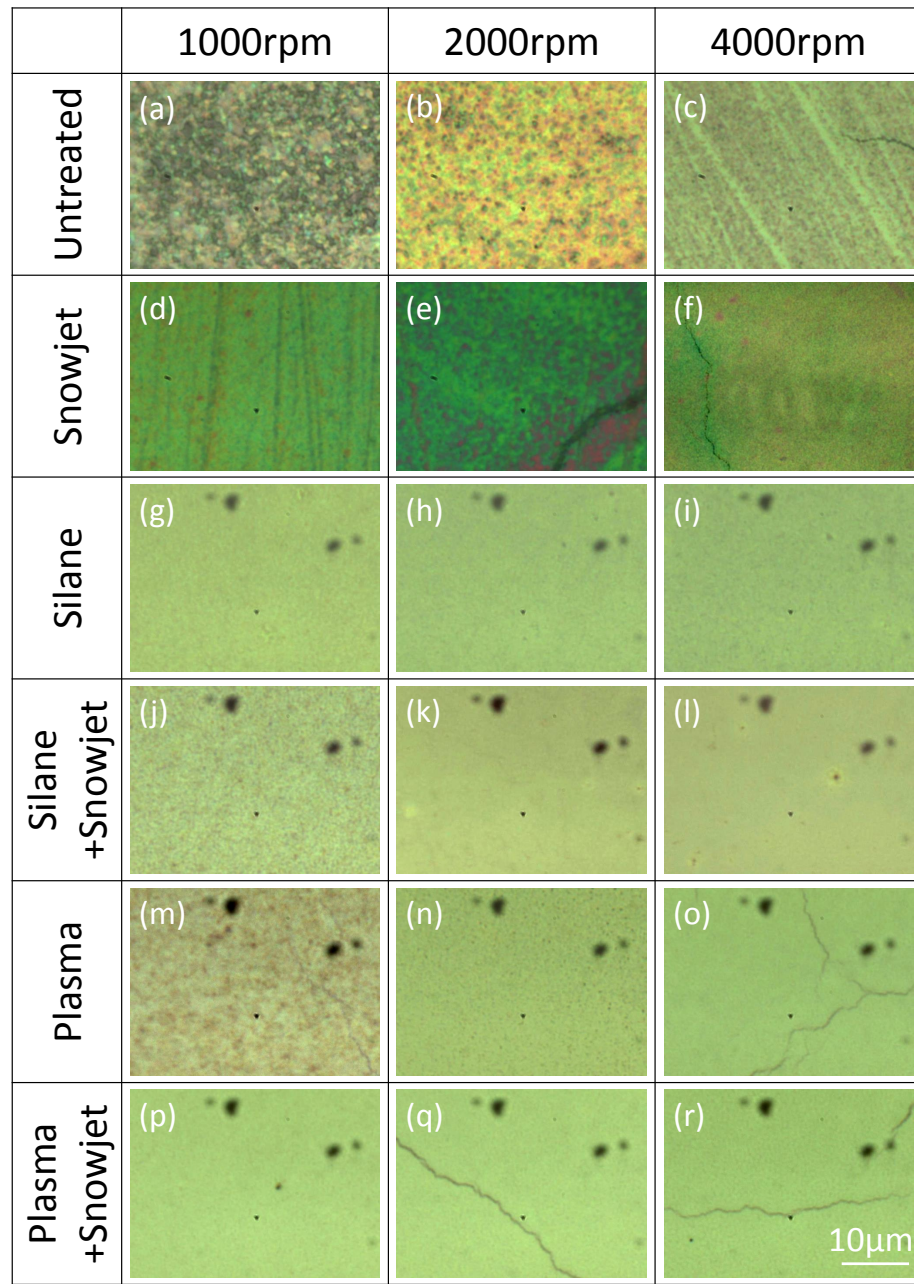


Fig. 4.6 BF images at 100 \times magnification of spin coated CHPI films, with spin speed and substrate preparation as labelled.

alignment is seen in both untreated and snowjetted films. As indicated by their BF images [Fig. 4.6(h,k,n,q)], the spectra and morphologies of films made using other substrate preparations are very similar, and the uniformity is greatly improved by functionalisation of the substrate via silanisation or plasma etching. As an indication of the sample uniformity, line scans are made on a 4000 rpm films made using untreated [Fig. 4.8(c)] and silanised and

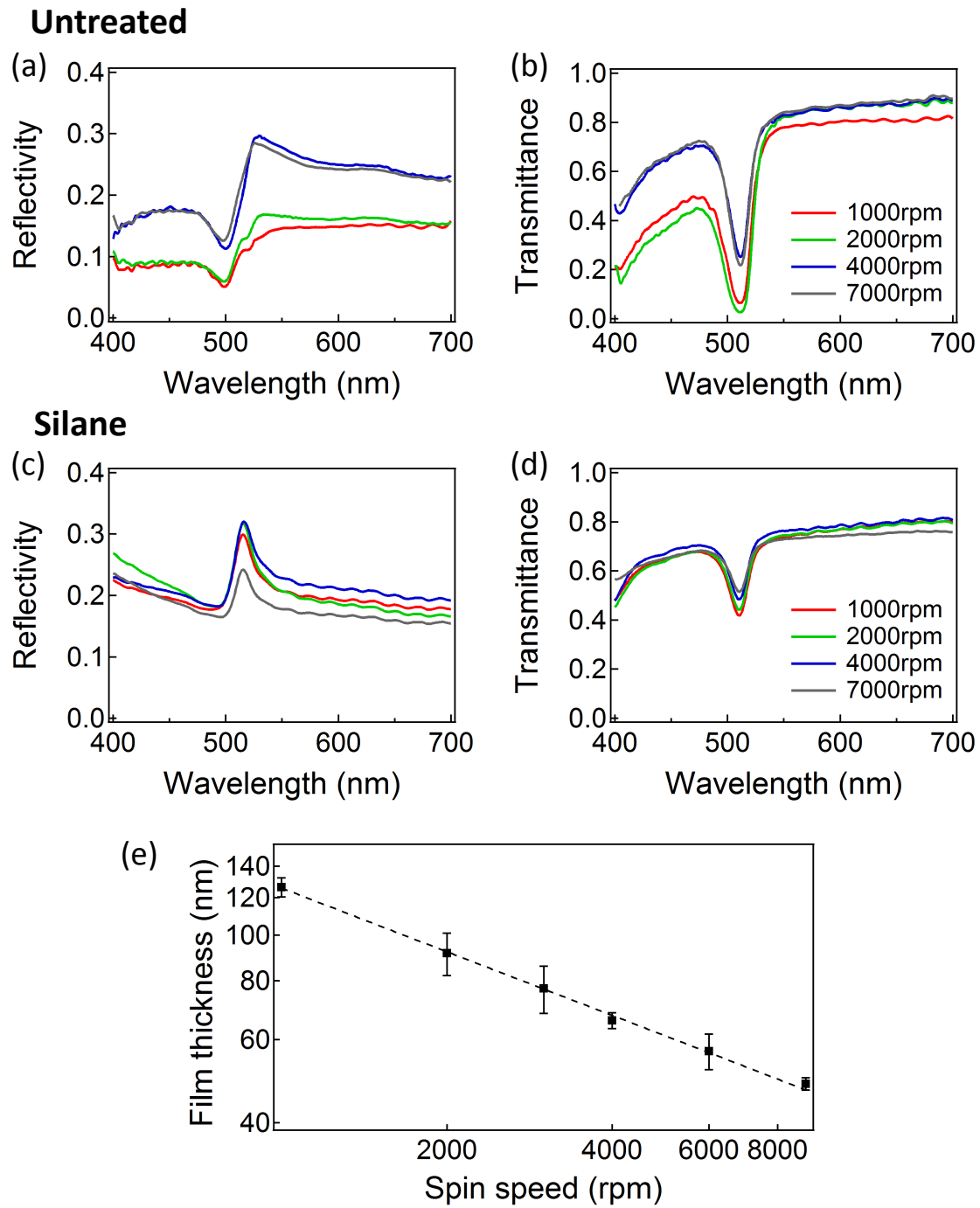


Fig. 4.7 Reflection and transmission spectra for CHPI films prepared using a variety of spin speeds on (a,b) untreated and (c,d) silanised substrates. (e) Effect of spin speed on CHPI film thickness on untreated substrates for 30 mg/ml solutions. The dashed lines represents a fit to $a\omega^{-b}$, with $b = 0.45 \pm 0.01$.

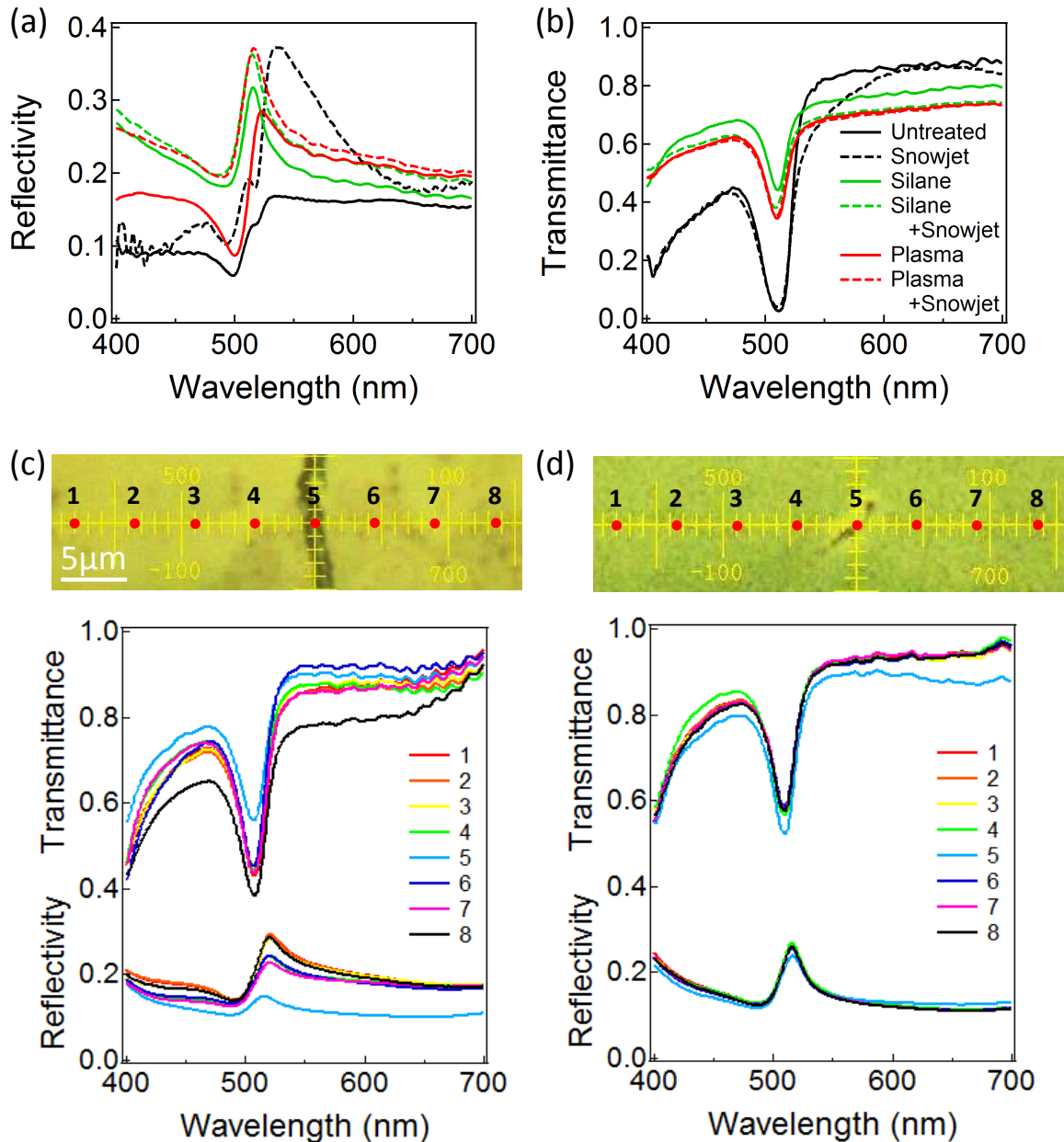


Fig. 4.8 Reflection and transmission spectra (collection spot diameter $\approx 20 \mu\text{m}$) of 2000 rpm CHPI films created using a variety of substrate preparation techniques. Reflection and transmission spectra (collection spot diameter $\approx 1 \mu\text{m}$) of 4000 rpm CHPI films prepared on (c) untreated and (d) silanised and snowjetted substrate at the positions indicated.

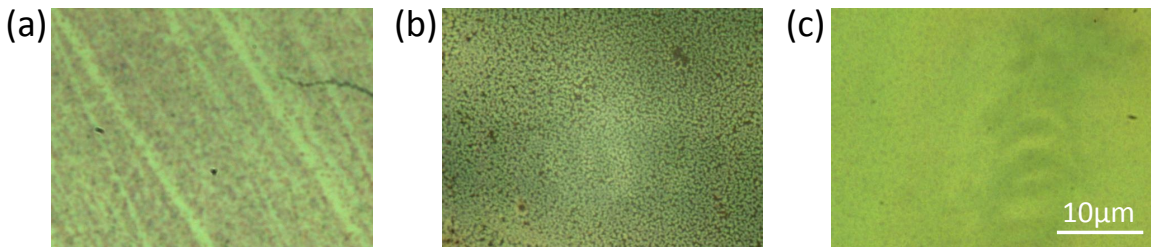


Fig. 4.9 BF images at 100 \times magnification for 4000 rpm CHPI films made on untreated substrates in (a) low, (b) high and (c) dehydrated spin coater atmospheres.

snowjetted [Fig. 4.8(d)] substrates (collection spot diameter $\approx 1\text{ }\mu\text{m}$). The near-identical spectra of all areas on the functionalised substrate is further proof of the film uniformity observed in BF images.

4.5.3 Humidity

Hydrogen bonding between the organic and inorganic constituents is essential to the assembly of the perovskite structure, therefore unwanted bonding or screening due to water molecules in the atmosphere can disrupt this process. A continuous CHPI film is formed at 4000 rpm on an untreated substrate in a low humidity atmosphere [Fig. 4.9(a)], however the same spin coating conditions leads to dewetting in high humidity despite the hydrophilic organic group [Fig. 4.9(b)]. Clearly the spin coater should desiccated as much as possible, and in order to achieve this the dehydration agent CaCl_2 is placed in the spin coater roughly one hour before film production. The spin coater is also pumped with N_2 gas just before spinning, and the resulting film is very uniform even without the use of substrate functionalisation [Fig. 4.9(c)].

4.6 Conclusions

Thin films of PbI perovskites with thickness 30 – 150 nm can be produced reliably using spin coating. The film morphology depends strongly on the organic molecule used in the perovskite, and dewetted films are produced for hydrophobic moieties. However film coverage and uniformity can be improved by using higher spin speeds, or functionalisation of the substrate surface using techniques such as silanisation. Film thickness is controlled by the spin speed and initial solution concentration, and follows an $\omega^{-0.45}$ dependence, close to the theoretical prediction. Formation of the perovskite structure can be disrupted by water

in the atmosphere, and a dehydration agent can be placed in the spin coater to controllably produce a low humidity environment. The simplicity and adaptability of spin coating allows PbI perovskite thin films to be deposited on suitable substrates to create hybrid nanostructures.

Chapter 5

Micromechanical exfoliation of lead iodide perovskites

5.1 Introduction

Uniform thin films of PbI perovskites can be created over large areas as a result of spin coating, however it is hard to achieve thicknesses $\lesssim 20$ nm. For thinner samples a layer-by-layer deposition technique can be used [52, 55]. Micromechanical exfoliation is another way of producing ultra-thin samples, where thicker crystals are cleaved to form progressively thinner samples.

In recent years much attention has been paid to 2D layered compounds such as graphene or transition metal dichalcogenides. Due to weak van der Waals bonding, it is easy to separate neighbouring layers and form ultra-thin samples [138–143]. In these materials new optical and electronic properties emerge for mono- or few-layer regions, providing new avenues for material application. In this Chapter I report the micromechanical exfoliation of 2D PbI perovskites, and explore the few-layer behaviour of such systems via optical spectroscopy.

5.2 Experimental methods

Preparation of exfoliated PbI perovskite samples is shown in Fig. 5.1. Lead iodide (PbI_2) microcrystals are synthesized using a previously described solvothermal method, and intercalated using an 8 mg/ml organic ammonium iodide/toluene solution to create hexagonal perovskite microcrystals $\sim 30\ \mu\text{m}$ in lateral size [144]. The crystals are then heated at 50°C

to completely remove the intercalation solution. We then use a micromechanical exfoliation technique to create thinner flakes, transferring the resulting samples onto an oxidized silicon (Si) wafer for further measurements. The thinnest regions are identified using optical microscopy, and then characterized with white light spectroscopy and atomic force microscopy (AFM).

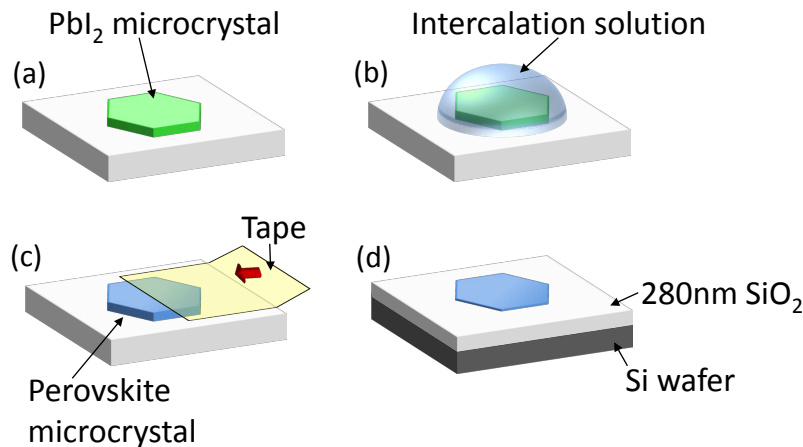


Fig. 5.1 Preparation of exfoliated perovskite samples.

5.3 Exfoliated CHPI samples

BF images of intercalated CHPI and C_{12}PI microcrystals at $20\times$ magnification are shown in Fig. 5.2(a,b). Reflectivity spectra for such microcrystals show an exciton resonance at $\sim 500\text{nm}$ indicating formation of the 2D MQW structure, with Fabry-Perot fringing due to the finite crystal thickness, typically $\sim 1\ \mu\text{m}$. The top surfaces of crystals are rough as a result of etching by the intercalation solution, however such surfaces should adhere to the tape during exfoliation, and will therefore not be present in the measured samples. The exciton wavelength (grey dashed line) varies from literature values as a build up of strain in thick layer stacks can lead to structural distortions/rearrangements and thus change the exciton energy [28, 62, 144].

BF images of exfoliated flakes of CHPI and C_{12}PI [Fig. 5.2(c,d)] show similar features. Although the crystals are fractured during the exfoliation process, we are able to obtain ultra-thin samples ($< 20\ \text{nm}$) with lateral sizes $\sim 1 - 10\ \mu\text{m}$. We observe excitonic resonances in both CHPI and C_{12}PI samples, however due to the bistability of C_{12}PI we use CHPI samples for further analysis.

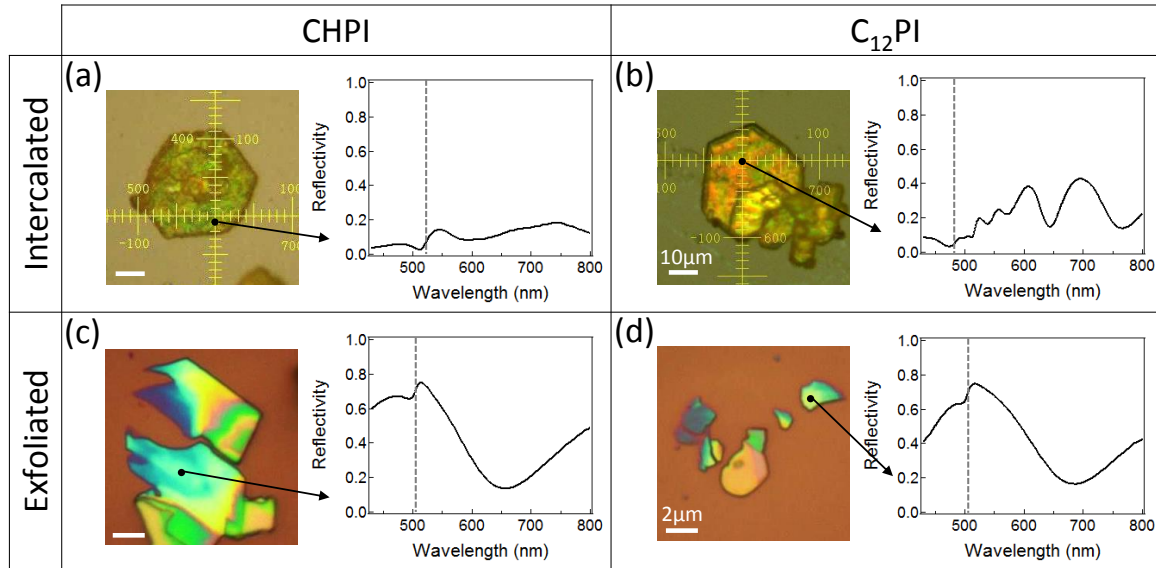


Fig. 5.2 Bright field images of intercalated (a) CHPI and (b) C₁₂PI microcrystals on glass at 20× magnification, and exfoliated (c) CHPI and (d) C₁₂PI flakes at 100× magnification. The reflectivity spectra of the areas indicated are shown on the right. Grey dashed lines indicate the wavelength of the exciton resonance.

BF and DF reflection images of a typical CHPI flake are shown at 100× magnification in Figs. 5.3(a,b) respectively. The DF scattering seen from the edges and grain boundaries of the sample is typical for such crystals. The reflectivity spectra for these exfoliated samples [Fig. 5.3(d)] consist of an excitonic Fano resonance at $\lambda_{ex} \approx 504$ nm superimposed on a background of Fabry-Perot fringes. These fringes correspond to the colour of the crystal seen in BF, and come from the path difference experienced by light double passing through the flake. The oxide layer on the substrate is designed to maximize optical contrast for very thin layers, and while optimized for graphene, this 280 nm SiO₂/Si system also works well for CHPI. By using this spectral information in conjunction with AFM measurements [Fig. 5.3(e)], we can correlate the position of Fabry-Perot fringes with thickness t . Thus it is then possible to spectroscopically determine the thickness of CHPI flakes.

A histogram of AFM heights in the boxed area of Fig. 5.3(c) shows three predominant thicknesses, which can be fit to Gaussians separated by steps of 1.6 nm [Fig. 5.3(f)]. This interlayer spacing agrees well with X-ray diffraction measurements, where the periodicity was found to be 1.7–1.8 nm [54, 145]. Due to the presence of molecules adsorbed on the surface of the substrate, the initial step of 2.5 nm is likely due to a monolayer, allowing us to label the three peaks as 1-, 2-, and 3-layer regions.

Spectroscopic measurements of flake thickness require detailed knowledge of the CHPI

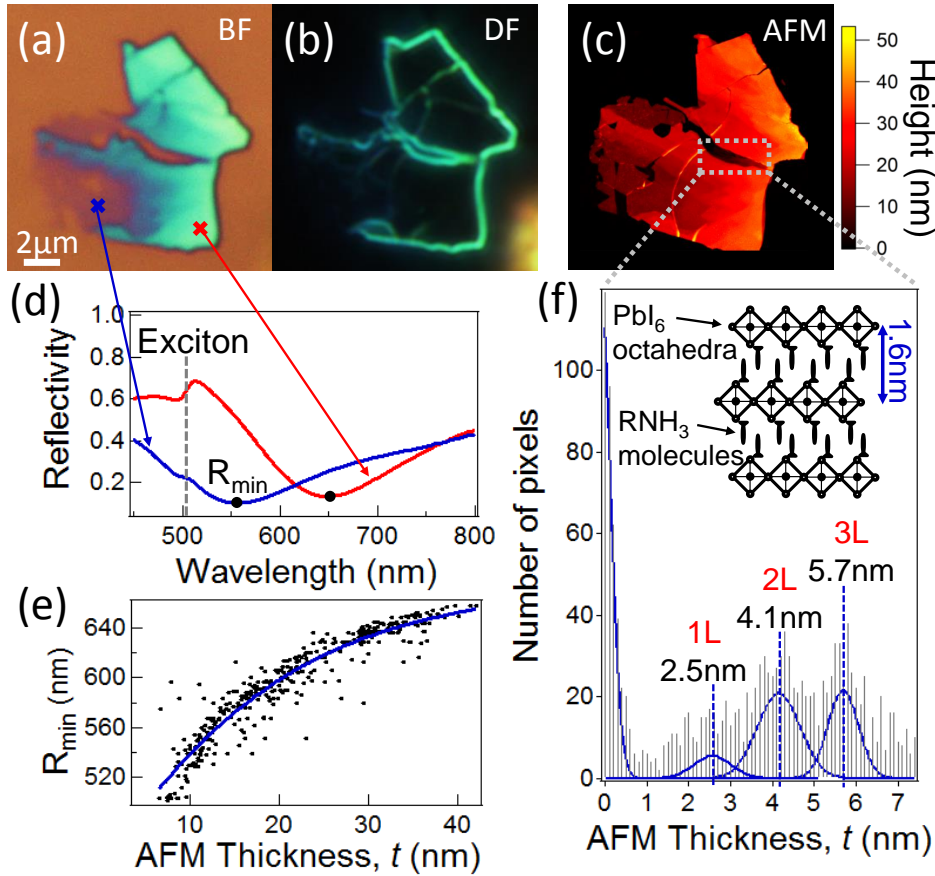


Fig. 5.3 Images in $100\times$ magnification using (a) bright and (b) dark field on an exfoliated CHPI flake; (c) AFM image of the same area. (d) Reflectivity spectra of two regions on the flake. The exciton wavelength is indicated by the dashed line. (e) Relationship between the measured reflectivity minimum (labelled as R_{\min} in (d)) and AFM thickness. (f) Histogram of heights measured in the boxed area of (c). Multipeak fitting to the data (blue lines) gives an interlayer spacing of 1.6 nm. The inset shows the structure of 2D PbI perovskites.

refractive index, which is not well known. Instead we extract the required information from reflectivity data using the transfer matrix formulation [146]. In the wavelength range of interest (460 - 750 nm), the dielectric function ϵ of 2D PbI perovskites can be modelled as the sum of a constant background and two Lorentzian oscillators: the exciton (*ex*) and an additional charge transfer (*CT*) transition at ~ 400 nm [24, 62, 87, 147–149]. Hence

$$\epsilon = \epsilon_1 + i\epsilon_2 + \frac{A_{ex}}{\lambda_{ex}^2 - \lambda^2 + i\Gamma_{ex}\lambda} + \frac{A_{CT}}{\lambda_{CT}^2 - \lambda^2 + i\Gamma_{CT}\lambda}, \quad (5.1)$$

where ϵ_1, ϵ_2 are the background terms, while A_i is the amplitude, λ_i the wavelength, and Γ_i the linewidth of oscillator i . The refractive index ($\tilde{n} = \sqrt{\epsilon}$) can then be used in the

multilayer transfer matrix to calculate the expected reflectivity. The *CT* peak, due to the charge transfer between organic and inorganic layers, is particular sensitive to disorder and the local dielectric environment, and depends on the precise spin coating conditions when comparable thin films are produced [62].

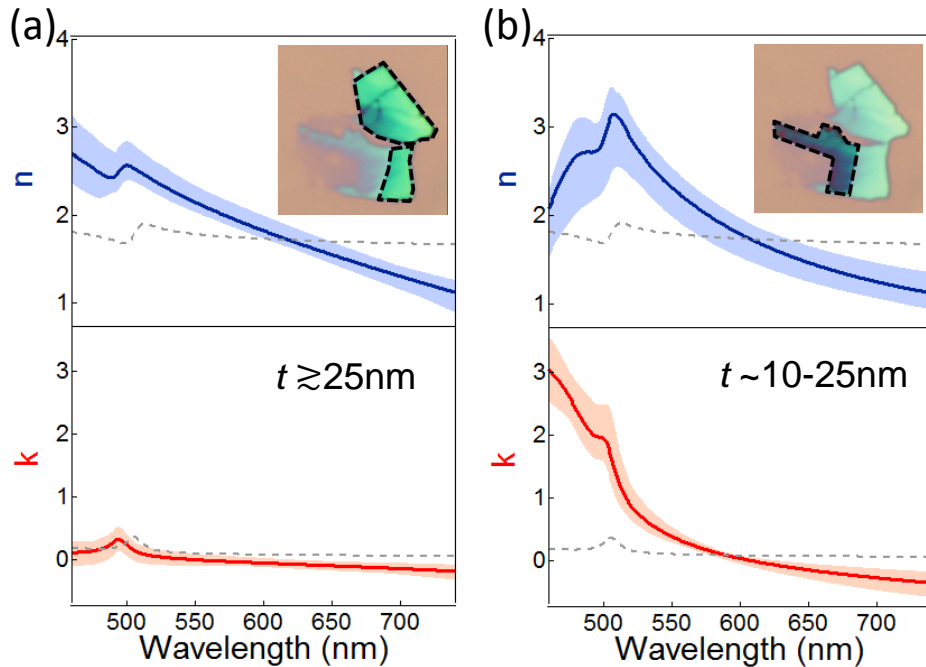


Fig. 5.4 Fitted complex refractive index of CHPI flakes for more than 200 pixels. Two regimes are found: (a) low absorption, occurring at positions of high thickness ($t \gtrsim 25$ nm), and (b) high absorption, at lower thickness ($t \sim 10-25$ nm). The insets indicate typical areas where each regime is found. Shaded regions show the range of values extracted from the fit, and grey dotted lines represent the refractive index of a CHPI film ($t \sim 60$ nm) measured using ellipsometry.

The results of these refractive index fits for more than 200 spectra are shown in Fig. 5.4. The fitting works well for spectra that are not collected at the edges of the flake, therefore the thinnest areas are excluded. Within these regions, two main regimes of refractive index are observed. In both cases the background and exciton oscillator are relatively unchanged. For thicker areas of the sample ($t \gtrsim 25$ nm) a low-absorption regime is observed, where the *CT* oscillator is mainly reflective. For thinner areas ($t \sim 10-25$ nm) a high-absorption regime is seen, where the *CT* oscillator redshifts and becomes more optically active. As discussed below, the thickness range encompassed by the absorbing regime is correlated with a region of structural reconfiguration. This leads to a change in the energy states of the hybrid perovskite, and modifies the charge transfer between neighbouring organic and

inorganic sheets. For comparison, the refractive index of a $t \sim 60$ nm film extracted from ellipsometry (grey dashed line) is also shown in Fig. 5.4. The film absorption (k) is closer to that of thicker flake areas, with a reduced contribution from the *CT* oscillator in the refractive index. X-ray diffraction shows that while distinct layers are formed during spin coating, there is greater structural disorder in each layer when compared with intercalated PbI_2 microcrystals [144]. This interface mismatch can be responsible for a large range of charge transfer environments, leading to the reduced strength of the *CT* resonance that we observe here.

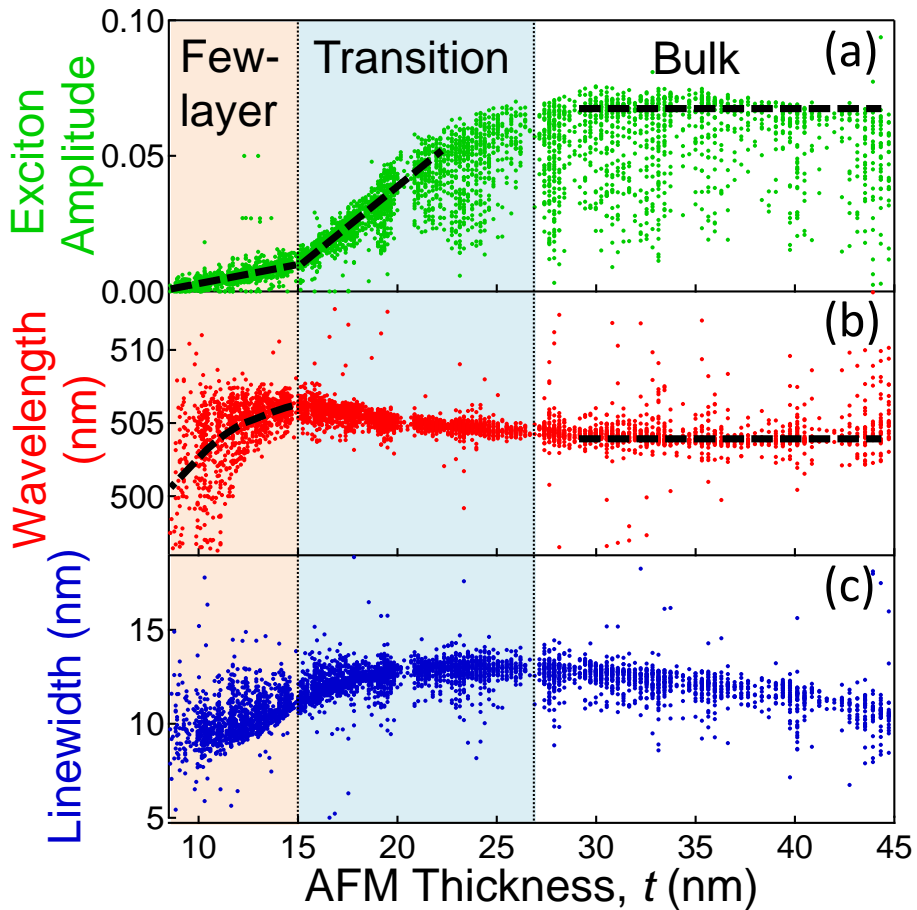


Fig. 5.5 Fitted exciton (a) amplitude, (b) wavelength, and (c) linewidth from reflectivity spectra (see Eq. 5.2). Dashed lines are guides for the eye.

In reflectivity the exciton produces a Fano lineshape due to interference between its narrow resonance and the continuum background. On account of this complication, we

extract information about exciton properties by describing $\Delta R = R_{\text{CHPI}} - R_{\text{substrate}}$ as

$$\Delta R = R_{\text{bkg}} + A \frac{(\lambda - \lambda_{\text{ex}} + q\gamma)^2}{(\lambda - \lambda_{\text{ex}})^2 + \gamma^2}, \quad (5.2)$$

where R_{bkg} represents the continuum background with Fabry-Perot fringing; A , λ_{ex} and γ are the amplitude, wavelength, and linewidth of the exciton respectively, and the parameter q describes the asymmetric shape of the Fano resonance. The results of the fit are shown in Fig. 5.5 for positions across many flakes with different thicknesses. A , λ_{ex} and γ are equivalent to the corresponding terms in Eq. 5.1, while q represents the interference between the exciton, CT and background terms. Near the vicinity of the exciton the effects of the CT and background are not distinguished, therefore Eq. 5.2 allows us to focus exclusive on the exciton components, while Eq. 5.1 gives us the overall refractive index. Since the perovskite resembles a multilayer system, we find the exciton amplitude initially scales linearly with the number of layers as expected, before saturating at $t \approx 27$ nm (15 layers). The large variability of amplitudes at high thickness arises predominantly from spectra taken at edges of flakes. Linear extrapolation of our data indicates the exciton amplitude will drop to zero at $t \sim 7$ nm (3 layers). However layer-by-layer assembly of perovskite films has shown that linear increases in the exciton intensity occur only after the fourth layer, while two monolayers are required to observe room temperature exciton behaviour [55].

From Fig. 5.5, we identify 3 regions of interest. Firstly the ‘bulk’ region ($t \gtrsim 27$ nm), where the exciton wavelength remains roughly constant; secondly the transition region ($t \sim 15–27$ nm), where the wavelength begins to redshift, while the linewidth reaches a maximum; and finally the few-layer region, where the wavelength blueshifts below the bulk limit, along with a decrease in the linewidth. This data helps us understand the changes happening at a structural level: disorder causes inhomogeneous broadening of the exciton resonance [150–152], while the exciton energy is directly related to the angle between PbI_6 octahedra in the inorganic layers [44]. In ‘bulk’ CHPI, the exciton has a wavelength of 504 nm and a spectral width of ≈ 10 nm. Close to the thickness transition region, the system is seen to become more disordered as the PbI sheets rearrange, becoming flatter and more strained. Finally at small t , the few-layer regime reveals how the layers relax and crumple again to reach the lowest energy configuration. Extrapolation of the fitted exciton wavelength to monolayer thickness (3 nm) leads to a wavelength of ~ 495 nm, comparable to the value of ~ 490 nm reported for PbI_2 thin films [153, 154]. We were unable to spectroscopically probe areas with $t < 8$ nm (4 layers) as they lie on the edges of flakes, and are around 100 nm in size. Since the lateral resolution of reflectivity measurements is $1 \mu\text{m}$, these spec-

tra are averaged with the much bigger signals from thicker areas. In order to achieve more sizeable monolayer regions, large-area samples are desirable for exfoliation, for instance using solution-grown single crystals. Exfoliating onto flexible polymer substrates may also improve our capability for attaining large monolayer regions as this can reduce fracture of crystals. However our measurements clearly show that these organic-inorganic hybrid perovskites change their electronic properties as the thickness is reduced, and this is connected to changes in the strain, disorder and layer structure.

5.4 Conclusions

In conclusion, we report the exfoliation of 2D organic-inorganic perovskites. Monolayers are observed, and the interlayer distance was found to be 1.6 nm. As with other 2D materials, the thinnest regions (<8 layers) behave differently from the bulk material due to the influence of strain on the layer structure. We note however that the active excitonic layers are already electronically isolated in these hybrids, so changes in the band structure as observed in dichalcogenide systems are not expected. Instead, the effects seen are due to the re-organisation of organic molecules around the inorganic sheets. This suggests that pre-organisation of the intercalating molecules is key to controlling material structure at the monolayer scale, which may be accessible through chemical growth rather than exfoliation. This work suggests the potential to construct optoelectronic devices for monolayers of these hybrid materials, offering new routes to emission.

Chapter 6

Perovskite-coated metal islands

6.1 Introduction

Interactions between localised surface plasmons (LSPs) and material in their environment can be used for a host of applications. For example sensitivity of the resonance frequency to the local dielectric function can be exploited in sensing devices [155–158], while the large field enhancement caused by electron oscillations can be used to increase Raman signals [159–161] or emission [162–165]. LSP resonances of noble metal nanoparticles can be tuned across the visible spectrum via their geometries, so fabrication of metal island nanostructures should be tuned to their application.

In this Chapter I will describe the creation of Au/Ag nano-islands overcoated with a perovskite layer, then use structural and optical characterisation techniques to explore how excitons are affected by electrons oscillations in the metal.

6.2 Metal island films

The morphology of a thin film depends on interactions between the film and substrate atoms (i. e. the diffusion of metal atoms on substrate surface), as well as external conditions such as deposition rate, substrate temperature and subsequent annealing steps [166]. Deposition via evaporation is a heterogeneous nucleation process, and requires high vapour pressure. Various growth modes are possible, but for noble metal films deposited on glass the metal-metal interaction is stronger than the metal-substrate interaction, causing island formation on the substrate. With increased deposition time such islands can coalesce, either preserving the grain boundaries or forming a continuous structure.

Such metal island films (MIFs) are essentially nanoparticle arrays: if the islands are well separated (separation $l \gtrsim$ island diameter d) then there is no optical coupling between the particle resonances and we expect to see a single LSP resonance in optical spectra. The resonance wavelength of such arrays depend on the island geometry, and can be controlled by the deposited film thickness [167–171]. As with nanoparticles we can model these islands as dipoles embedded in a medium with dielectric function ϵ to predict the resonance wavelength [172–175].

6.2.1 Experimental methods

Glass substrates are prepared as described in Sec. 4.3. Metal deposition is performed using an Edwards resistance evaporator, under pressure $\sim 4 \times 10^{-6}$ mbar with deposition rate $\sim 0.5 \text{ \AA/s}$. The substrates are not heated, and the deposited film thickness t is determined by a 6 MHz quartz crystal microbalance. To avoid oxidation, Ag samples are placed in a nitrogen purge dessication cabinet within 15 minutes of fabrication, and only removed for further processing/characterisation. Annealed Au and Ag films are made by heating the samples at 200°C for 24 hours. In order to create the CHPI overcoating, a CHPI/THF solution is spin coated onto the nanostructured films under a dehydrated atmosphere (layer thickness $\sim 100 \text{ nm}$). The samples are then characterised using AFM, SEM, and white light microscopy. 400 unpolarised reflection (R) and transmission (T) spectra are taken over an area $0.5 \times 0.5 \text{ mm}^2$, and due to sample uniformity, all 400 spectra are averaged to produce the data shown, where extinction is defined as $E = 1 - R - T$.

6.2.2 Au metal island films

SEM images of evaporated Au films on glass show the formation of a rough, non-uniform, but continuous film for $t = 30 \text{ nm}$ [Fig. 6.1(c)]. As t decreases dewetting is observed as a result of weak Au-glass interactions [Figs. 6.1(a,b)]. During annealing, Au atoms diffuse and form distinct islands [Figs. 6.1(d-f)]. With decreasing t the islands become more closely spaced and ellipsoidal, smaller in both lateral size d and height h [Fig. 6.2]. For $t = 8 \text{ nm}$ we observe islands with $4 \sim 50 - 100 \text{ nm}$, $h \sim 70 \text{ nm}$, and $l \sim 100 - 200 \text{ nm}$. The decrease in size can also be seen optically in $100 \times$ magnification DF images, where scattering from the islands due to LSPs is broadband for $t = 30 \text{ nm}$, but becomes progressively redder as the island size decreases [Fig. 6.2].

Fig. 6.3 shows the extinction spectra for $t = 8 \text{ nm}$ as-deposited and annealed Au MIFs. We observe a resonance at 570 nm in the extinction of the as-deposited film, however this is

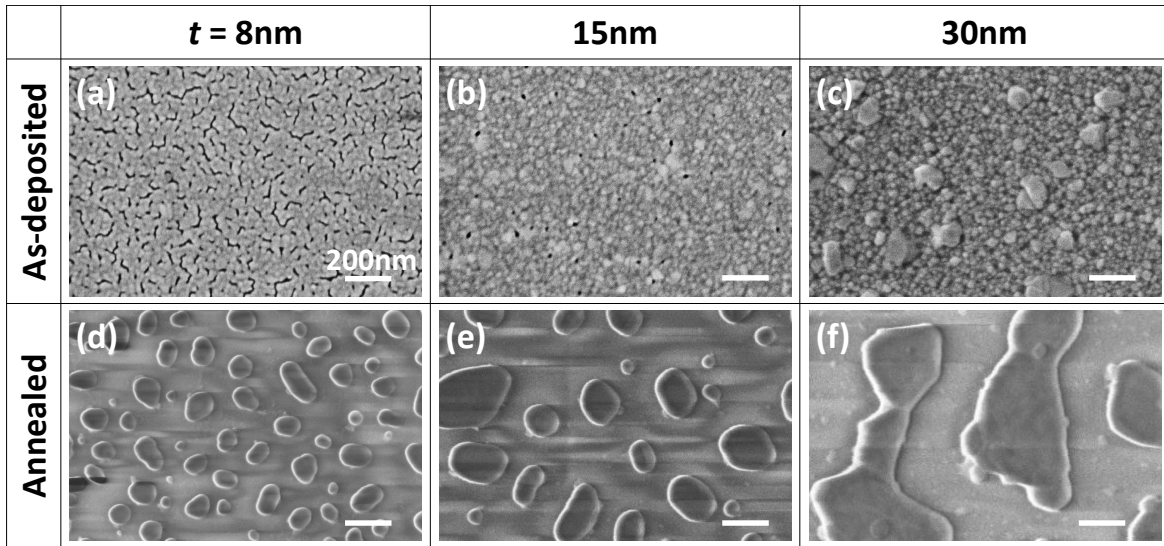


Fig. 6.1 SEM images of (a-c) as-deposited and (d-f) annealed evaporated Au metal island films. The initial deposited film thickness t is labelled.

due to grains and therefore has a large linewidth of 245 nm. In the annealed film we observe a resonance at 550 nm with linewidth 50 nm due to island LSPs.

6.2.3 CHPI-coated Au metal island films

BF images at $100\times$ magnification show the formation of CHPI on glass [Fig. 6.3(a)] and $t = 8\text{ nm}$ as-deposited and annealed Au MIFs (green areas in Figs. 6.3(b,c)). The exciton resonance at 505 nm is observed for all three films, confirming formation of the MQW structure despite some roughness and dewetting on Au substrates. We observe a redshift in the LSP resonance as a result of the CHPI coating (550 nm to 735 nm), with a considerable increase in the linewidth due to the non-uniform CHPI coverage (50 nm to $\sim 200\text{ nm}$). However the excitons in CHPI are completely unaffected by the presence of Au islands, remaining at the same wavelength and linewidth although the overall magnitude of the extinction across the entire visible range by around 20%.

6.2.4 Ag metal island films

The morphology of Ag evaporated films on glass are similar to Au films: rough films lead to dewetted films with decreasing t , as well as formation of MIFs when the as-deposited films are annealed [Fig. 6.4]. However the interactions between Ag atoms and glass is clearly stronger as annealing only causes coalescence and larger grains for $t = 30\text{ nm}$ films, not

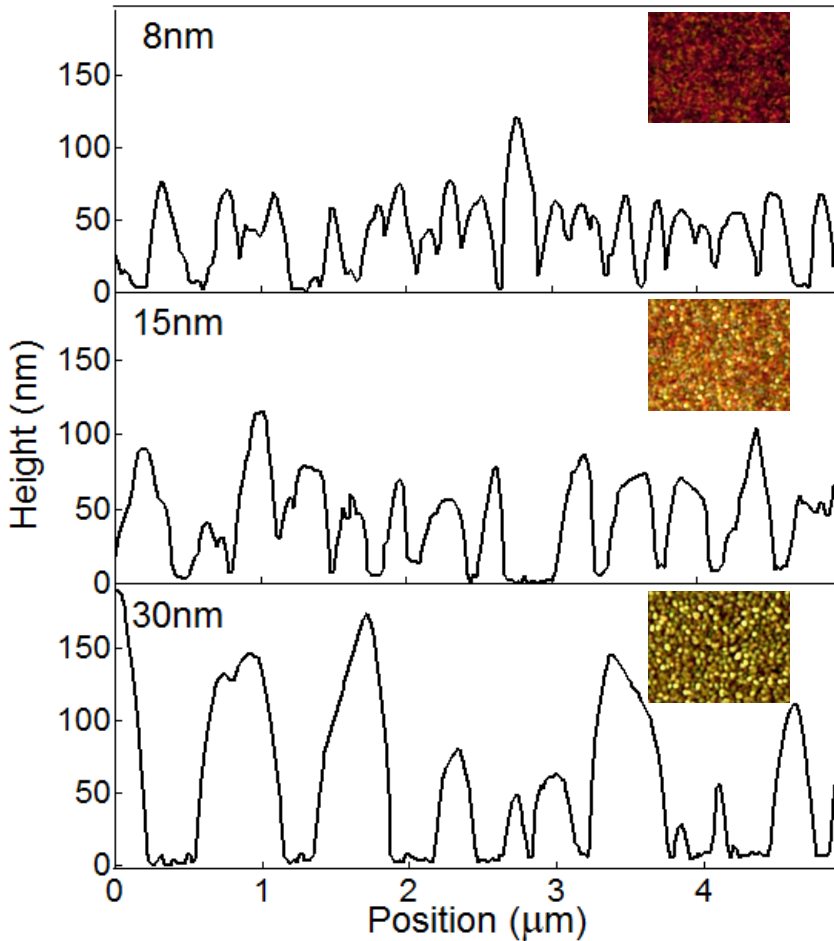


Fig. 6.2 AFM profiles of annealed Au metal island films. The deposited film thickness t is labelled. Insets show 100 \times magnification DF images of the samples.

separated islands. Annealed $t = 8$ nm Ag MIFs consist of ellipsoidal islands with $d \sim 40 - 100$ nm, $h \sim 80$ nm, and $l \sim 50 - 150$ nm [Fig. 6.5]. DF images at 100 \times magnification also show a change from broadband white scattering to green as t decreases [Fig. 6.5].

As seen in the SEM images, as-deposited Ag films are essentially continuous with some dewetting if $t > 8$ nm. Thus extinction spectra are similar to that of bulk Ag films, with increasing extinction up to the band gap ~ 300 nm [Fig. 6.6(a)]. However resonances can be observed if $t \leq 8$ nm, particular $t = 2$ nm (resonance 560 nm and linewidth 175 nm), indicating formation of islands even without annealing (Sec. 6.2.6).

After annealing, LSP resonances of Ag islands dominate the extinction spectra [Fig. 6.6(b)]. Although the positions of the extinction peaks do not change significantly with t , there is a clear decrease in the linewidth of the $t = 2$ nm film compared to the others [Fig. 6.6(c)]. The

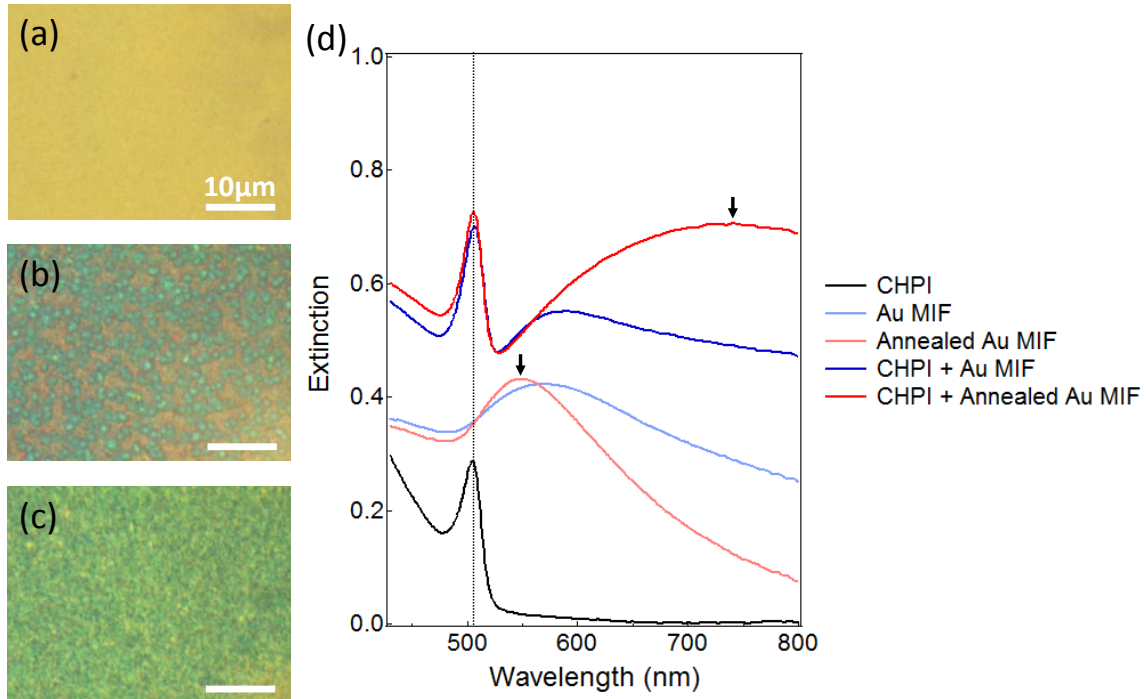


Fig. 6.3 BF images at $100\times$ magnification for CHPI films on (a) glass, (b) $t = 8\text{ nm}$ as-deposited and (c) $t = 8\text{ nm}$ annealed Au metal island films. (d) Average extinction spectra for 400 pixels over $0.5.5\text{ mm}^2$. The exciton wavelength is marked by the dashed line, and LSP resonances by arrows. The CHPI + (annealed) Au spectra are offset for clarity.

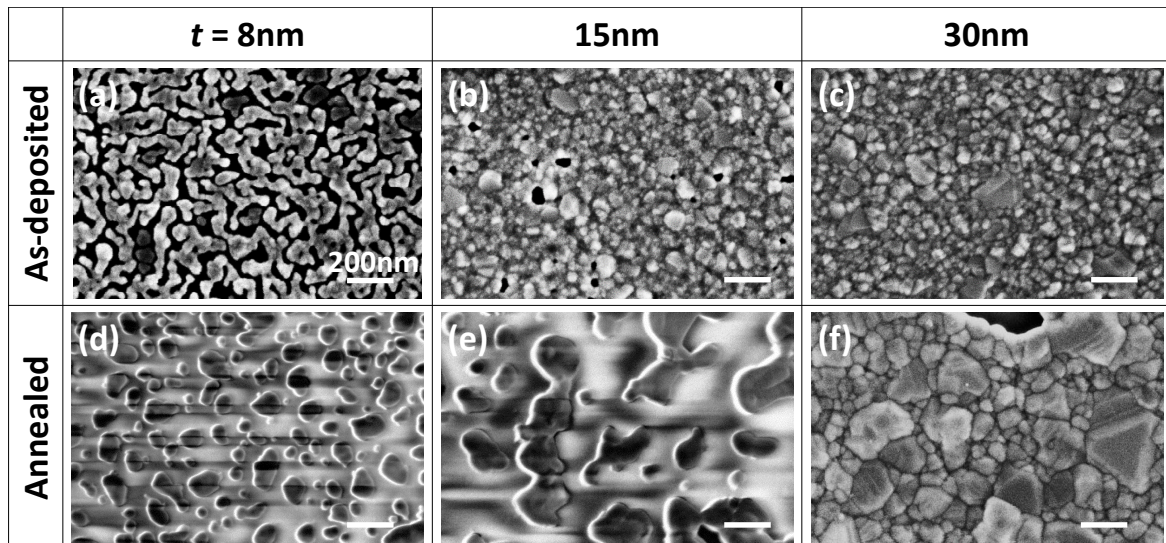


Fig. 6.4 SEM images of (a-c) as-deposited and (d-f) annealed evaporated Ag metal island films. The initial deposited film thickness t is labelled. Dark areas/streaks are seen in (a, d, e) due to charging of the sample.

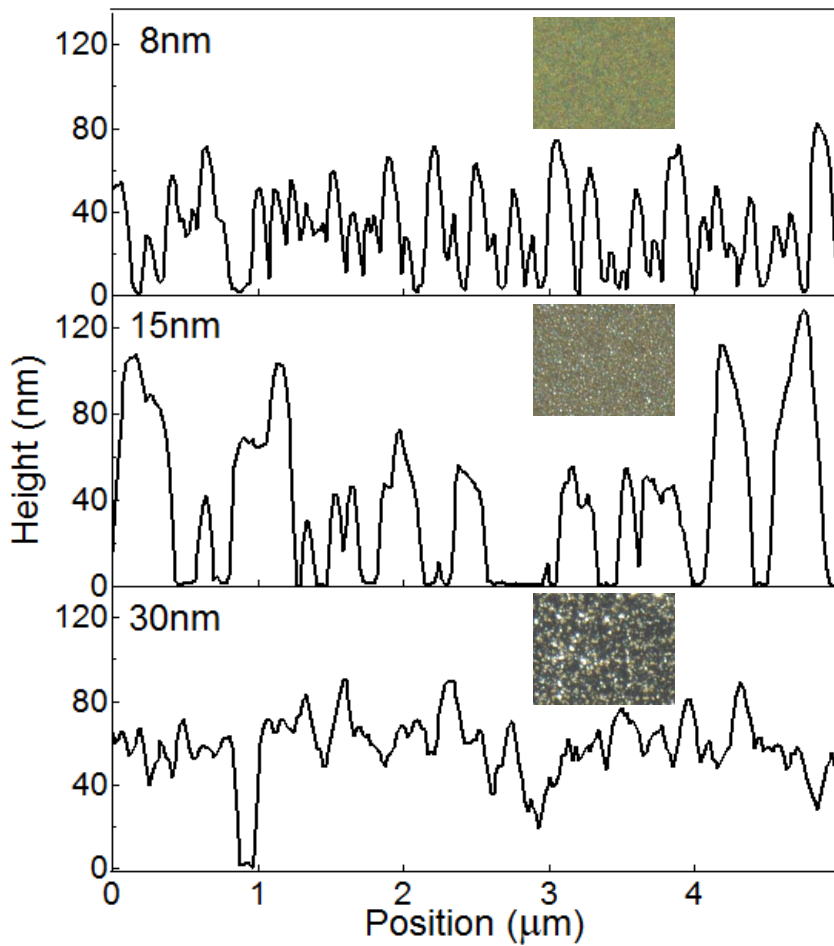


Fig. 6.5 AFM profiles of annealed Ag metal island films. The deposited film thickness t is labelled. Insets show 100 \times magnification DF images of the samples.

relative stability of the LSP wavelength suggests the average island size does not change with t , however we may have a larger range of island shape/size, leading to a superposition of many resonance wavelengths and higher order LSP modes. As a result of the CHPI coating the Ag island resonance is expected to redshift to ~ 550 nm.

6.2.5 CHPI-coated Ag metal island films

CHPI coated Ag films behave similarly for $t \leq 8$ nm, so here we use $t = 8$ nm as an example. BF images at 100 \times magnification show very little difference between CHPI films on glass, as-deposited or annealed Ag MIFs [Fig. 6.7(a-c)], although some non-uniformity is observed in the case of annealed Ag MIF. As-deposited Ag MIF causes little change to the

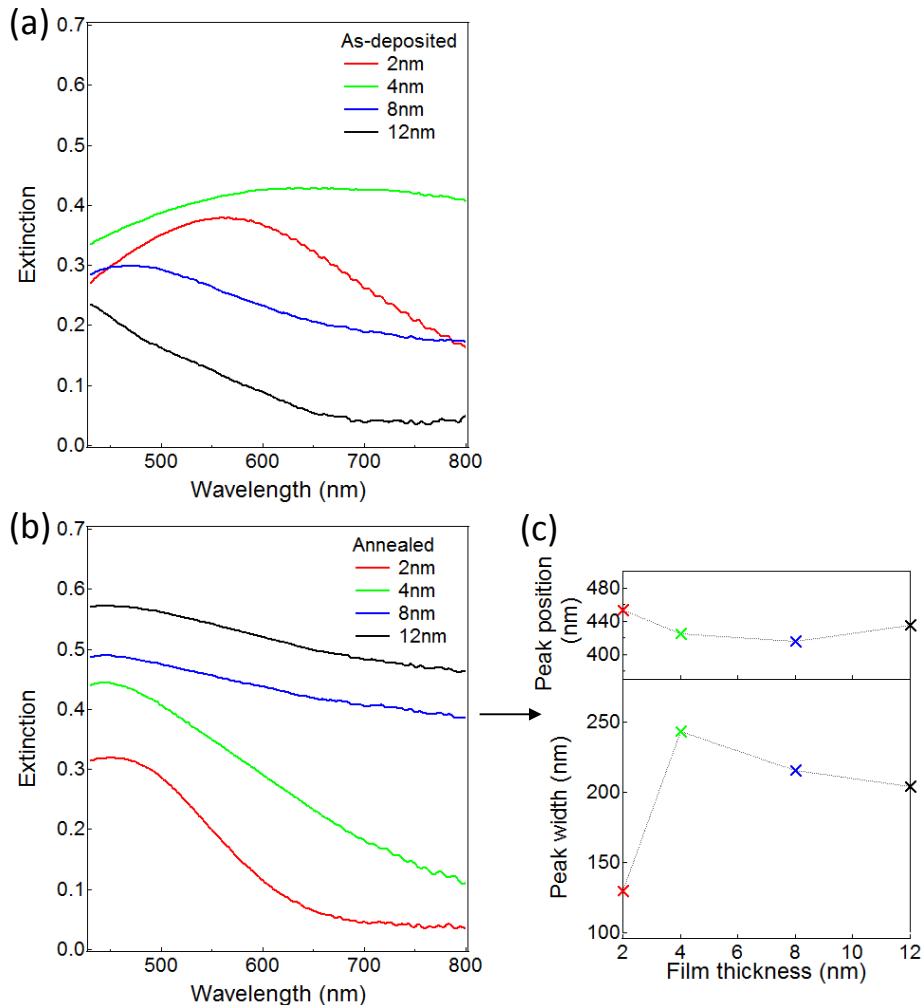


Fig. 6.6 Average extinction spectra of 400 pixels over $0.5 \times 0.5\text{mm}^2$ for (a) as-deposited and (b) annealed Ag metal island films with the labelled thickness t . (c) Extinction peak position and linewidth for the spectra in (b).

exciton wavelength (505 nm). However for annealed Ag MIF the island LSP is resonant with CHPI excitons, thus we see weak coupling in the form of a blueshift in the exciton by 5 nm to 500 nm, as well as an increase in the size of the exciton extinction peak by 12%. The extinction spectra of CHPI coated as-deposited Ag film is very similar to the spectra of CHPI film on glass (exciton at 505 nm). However the Ag islands of the annealed film causes a blueshift of the exciton wavelength to 500 nm, we see no appearance of the island LSP resonance, and there is an overall increase in the exciton extinction peak as a result of the Ag islands. Together this indicates weak coupling between the Ag LSP and excitons and enhancement in exciton absorption due to the near-field of the LSP.

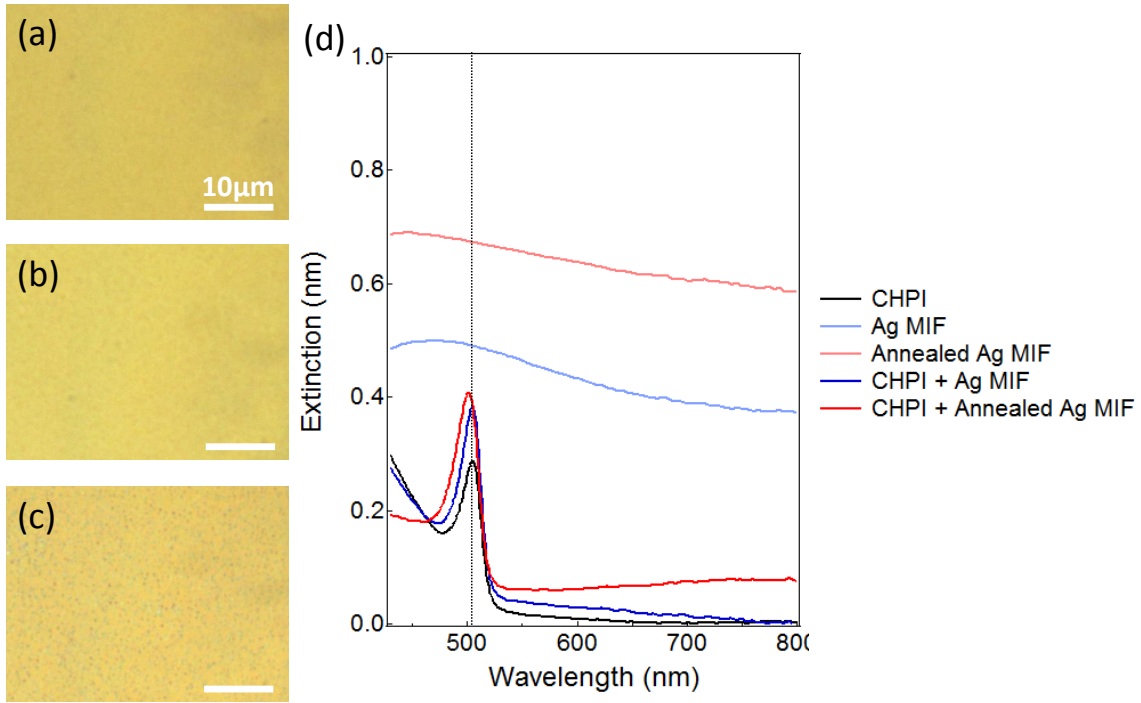


Fig. 6.7 BF images at 100 \times magnification for CHPI films on (a) glass, (b) $t = 8$ nm as-deposited and (c) $t = 8$ nm annealed Ag metal island films. (d) Average extinction spectra for 400 pixels over $0.5 \times 0.5\text{mm}^2$. The exciton wavelength of the CHPI film on glass is marked by the dashed line. The (annealed) Ag MIF spectra are offset for clarity.

6.2.6 Ag islands on CHPI films

Instead of coating Ag MIF films with CHPI, we also fabricate samples of Ag islands on top of a CHPI film on glass. Since the organic molecules undergo a melting transition $\sim 80^\circ\text{C}$ [40], we thermally evaporate only 2 nm of Ag to prevent degradation of the CHPI film due to heat. The AFM profile of a 2 nm as-deposited Ag MIF on glass [Fig. 6.8(b)] shows the formation of separated metal islands, with $d \sim 30$ nm and $h \sim 6$ nm. The AFM profile of a Ag MIF on CHPI is dominated by surface roughness of the CHPI film (~ 5 nm, *cf* Fig. 6.8(a)), however some high frequency noise on the order of d can also be seen. The lack of distinct MIF features suggests Ag islands may be partially embedded in the CHPI film. The thermal evaporation of Ag has not damaged the CHPI film as a strong exciton peak can still be seen in extinction spectra. The Ag island LSPs has again weakly coupled to excitons, causing a blueshift of 4 nm but an increase in extinction of only 5% [Fig. 6.8(d)].

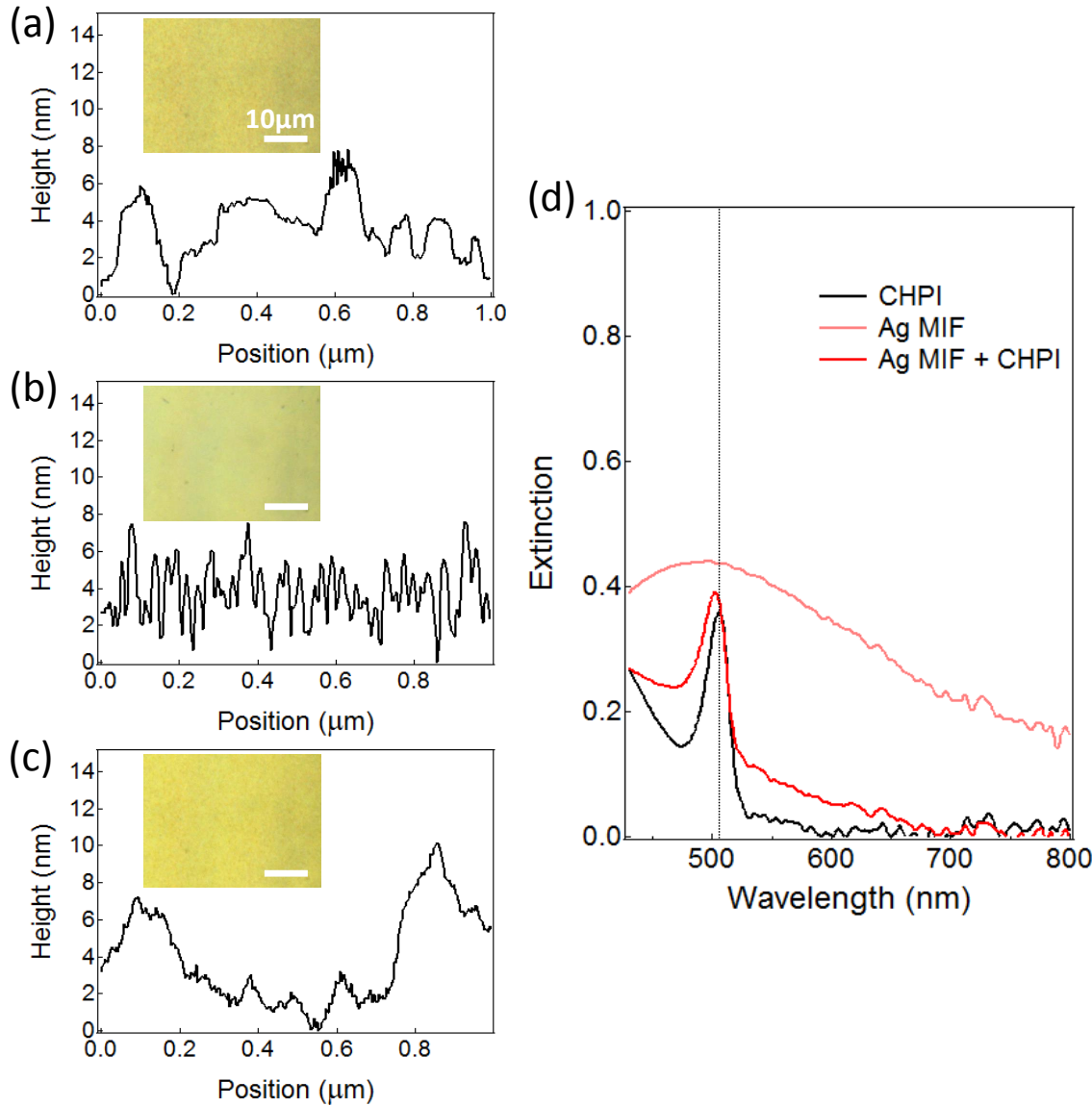


Fig. 6.8 AFM profiles of (a) CHPI film on glass, (b) $t = 2$ nm evaporated Ag film on glass, and (c) $t = 2$ nm evaporated Ag film on CHPI. Insets show 100 \times magnification BF images of the samples. (d) Average extinction spectra for 400 pixels over $0.5 \times 0.5\text{mm}^2$. The exciton wavelength of the CHPI film on glass is marked by the dashed line. The Ag MIF spectrum is offset for clarity.

6.3 Nanosphere lithography

Nanosphere lithography involves the evaporation of metals through a closely-packed 2D arrays of nano-/microparticles followed by removal of the spheres, leaving behind an array of metal islands on the substrate [176]. The geometry of the island array depends on the

diameter of spheres D . For a colloidal monolayer, the island diameter is $0.223D$, while the inter-island separation is $0.58D$ [177]. The interstices between spheres causes formation of triangular islands, however for small D the islands can become more spherical [178]. Array geometry can also be controlled by changing the evaporation angle [179].

Much like MIFs, these triangular islands produce a LSP peak in optical spectra that depends on the size/shape of islands as well as the dielectric environment [155], and can be modelled as an array of dipoles [157, 180]. However nanosphere lithography provides better control of the island geometry due to the lithography mask, and should provide a sharper LSP resonance compared to MIFs.

6.3.1 Experimental methods

We use $D = 460$ nm polystyrene (PS) microspheres from Sigma Aldrich to create the colloidal monolayer. The 10 vol% microsphere solution in water is diluted in a 1:1 mix with ethanol (absolute). Glass substrates are cleaned as described in Sec. 4.3 then plasma etched for 1 minute to create a hydrophilic surface. The substrates are placed at a 10° angle before a deionised water droplet is applied to cover the glass surface. A 2 wt% solution of sodium dodecylsulphate in water ($< 0.5 \mu\text{l}$) is applied to the water surface, where the amphiphilic molecules act to reduce the surface charge on PS microspheres. A pipette is used to spread PS microspheres onto the droplet surface [Fig. 6.9(a)], and the water is allowed to evaporate under standard conditions. 50 nm of Au is then deposited on the samples using an electron-beam evaporator system under pressure $\sim 5 \times 10^{-6}$ Torr at rate of 1 Å/s. The PS microspheres are dissolved by placing the sample in a solution of dichloromethane for 30 minutes, then sonicating the solution for 5 minutes. A CHPI/THF solution is spin coated onto the island samples under a dehydrated atmosphere. Optical characterisation is performed by taking 400 scans over a $50 \times 50 \mu\text{m}^2$ region, then averaged to produce the spectra shown.

6.3.2 Au islands

Closely-packed 2D arrays of PS microspheres are formed using this technique [Fig. 6.9(b)], and the ordering is best at contact lines. After removal of PS, triangular islands are left behind on the glass substrate [Fig. 6.9(c)] with $d \sim 90$ nm. We can see from Fig. 6.9(c) that even in the best areas we do not uniformly find well-separated triangular islands. Due to small deviations in the microsphere packing bow-tie shaped islands can form, and lines of Au are found at domain boundaries. However in the extinction spectra of such island

samples [Fig. 6.10] we do observe an LSP resonance at 590 nm with a linewidth of 80 nm, comparable to MIF spectra.

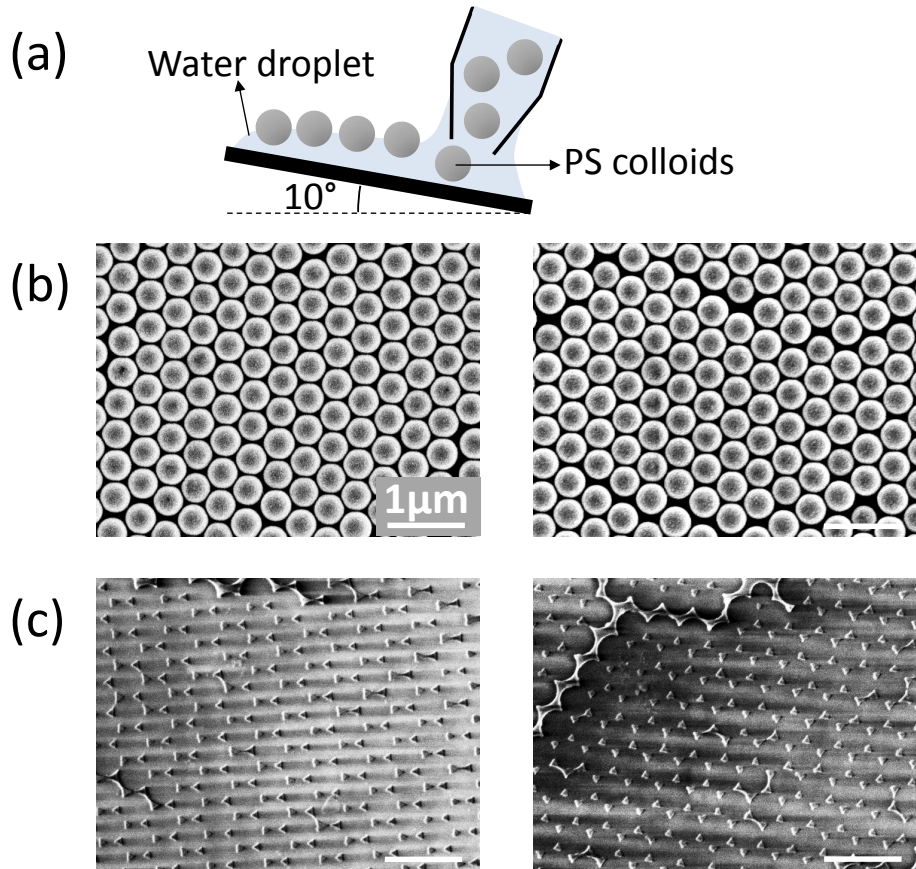


Fig. 6.9 (a) Illustration of the creation of $D = 460$ nm PS colloidal monolayer on a water droplet. (b) SEM of colloidal monolayer formed after the evaporation of water. (c) SEM of triangular islands formed after evaporation of Au and removal of colloids.

6.3.3 CHPI-coated Au islands

Similar to CHPI-coated Au MIFs, strong exciton peaks in the extinction spectra of CHPI-coated Au islands indicate formation of the MWQ structure. The exciton wavelength is unaffected by the Au (505 nm). As before, the LSP resonance redshifts due to the CHPI coating, and the linewidth broadens to ~ 150 nm. We observe a systematic increase of the LSP redshift as a result of increasing spin speed, and attribute this to more complete CHPI encapsulation of the Au islands as a result of larger forces at high spin speeds.

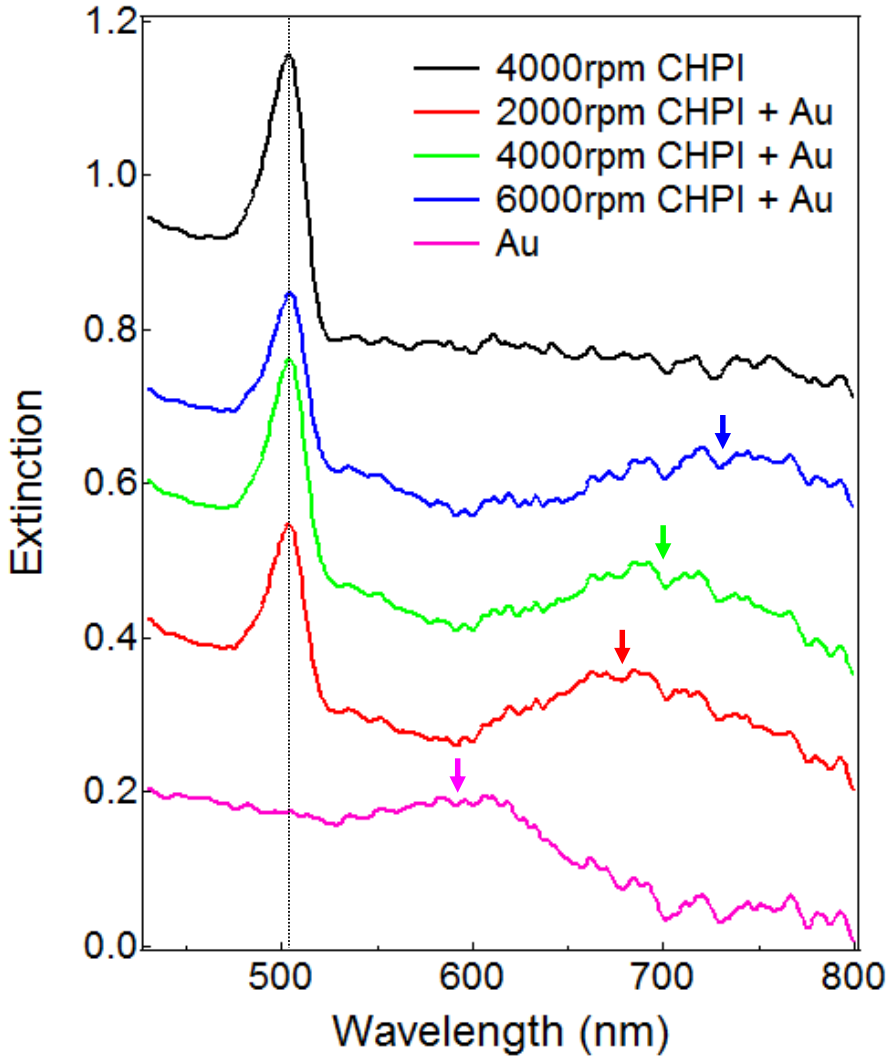


Fig. 6.10 Average extinction spectra (400 pixels over $50 \times 50 \mu\text{m}^2$) for CHPI-coated Au islands as labelled. Arrows indicate the positions of LSP resonances, and a dashed line indicates the exciton wavelength.

6.4 Conclusions

Evaporation of noble metals can be used to create ellipsoidal nanoparticles on a glass substrate. These metal island films behave like a nanoparticle array, and show distinct localised surface plasmon resonances that can be tuned via deposition parameters. In the case of perovskite-coated Au islands the LSPs are far off-resonance with excitons, and the dielectric coating causes a redshift in LSPs with no effect on excitons. In the case of perovskite-coated Ag islands, LSPs weakly couple to excitons and cause a blueshift in the exciton resonance of 5 nm, as well as an increase in exciton extinction by $\sim 10\%$ due to the electric field en-

hancement. Such enhancement has been investigated and is of particular interest for the design of solar cells [181–184].

The linewidth of the LSP resonance may be a barrier to strong coupling between plasmons and exciton in perovskite-coated nanostructures. The large variation in shape and size of metal particles in MIFs is an issue, however from our experiments more controllable islands created using nanosphere lithography do not show a marked improvement in LSP linewidth. Chemically created metallic NPs, which are often pre-screened for size, may provide an avenue for future exploration, however a method of controllably assembling a dense array of well-separated NPs from solution will need to be investigated.

Chapter 7

Perovskite-coated gratings

7.1 Introduction

Despite their structural simplicity, many electromagnetic modes can be sustained by grating samples, from diffractive interference effects to more localised and waveguided modes. In plasmonic gratings we can distinguish between such ‘photonic’ gratings modes and the ‘plasmonic’ modes that involve interactions with excited surface plasmon oscillations, as described in Sec. 3.3. The dispersion and efficiency of grating modes in optical spectra depend on the coupling with incoming/outgoing photons, and is very sensitive to factors such as the polarisation of light, changes in geometry and the refractive index of any coating materials.

In this Chapter I explore the optical behaviour of perovskite-coated 1D gratings, and use CHPI-coated Ag gratings to understand the interactions between excitons and SPPs.

7.2 Experimental methods

The fabrication of dielectric-coated metal gratings is shown in Fig. 7.1(a). Gratings are fabricated in ethylene tetrafluoroethylene (ETFE) from nanopatterned silicon stamps using nanoimprinting. A sheet of ETFE (thickness 0.8 mm) is placed on a silicon stamp, heated to 200°C and placed under 30 Bar pressure for 300 s. The ETFE is cooled to 90°C while maintaining the same pressure, then released from the stamp. An optically opaque metal layer (\sim 120 nm thick Ti/Ag) is deposited onto the polymer to form metal gratings. Chemically synthesised CHPI powder [Sec. 2.3.2] is dissolved in tetrahydrofuran and spin coated onto the gratings in a dehydrated atmosphere to produce a conformal coating. For polystyrene

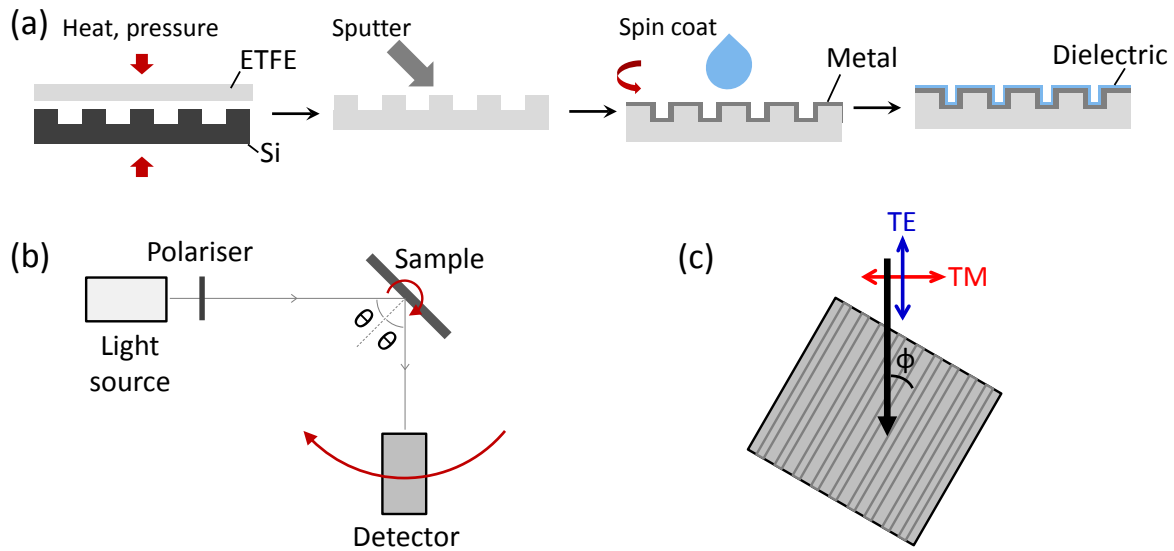


Fig. 7.1 (a) Fabrication of dielectric-coated metal grating. (b) Setup of angle-dependent reflectivity measurements. (c) Relationship between the polarisation of incoming light and azimuthal angle ϕ .

(PS)-coated gratings, $M_w = 500000$ PS powder is dissolved in toluene and spin coated onto the gratings. All samples are kept under a nitrogen atmosphere to prevent oxidation. Measurements by SEM and AFM of the metal and dielectric-coated gratings are used to extract the dimensions of the nanostructures. Polarised specular reflection measurements are made as a function of the incident polar (θ) and azimuthal (ϕ) angles using a polarised broadband white light source (215 – 2500 nm) [Figs. 7.1(b,c)]. The sample properties are uniform over cm^2 areas, with small variations due to the depth and morphology of the coatings.

7.3 Dielectric gratings

7.3.1 ETFE gratings

AFM scans of the imprinted $D = 417 \text{ nm}$ ETFE grating [Fig. 7.2(a)] show the formation of a square-wave grating with depth 140 nm and slit width 200 nm [Fig. 7.2(b)]. TM and TE polarised reflectivity scans show $m = -1$ photonic modes in air according to Eq. 3.7 [grey dashed lines on Figs. 7.2(c,e)] appearing as dips in the reflectivity [Figs. 7.2(d,f)]. In TE polarisation we also see the appearance of a redshifted photonic mode (grey dot-dashed line on Fig. 7.2(e)), attributed to light that has penetrated the transmissive ETFE. This mode fits well to Eq. 3.7 with $n = 1.4$, the reported ETFE refractive index [185]. For both polarisations the grating modes are no longer visible for $\phi > 60^\circ$. Note also a dip in the reflectivity of

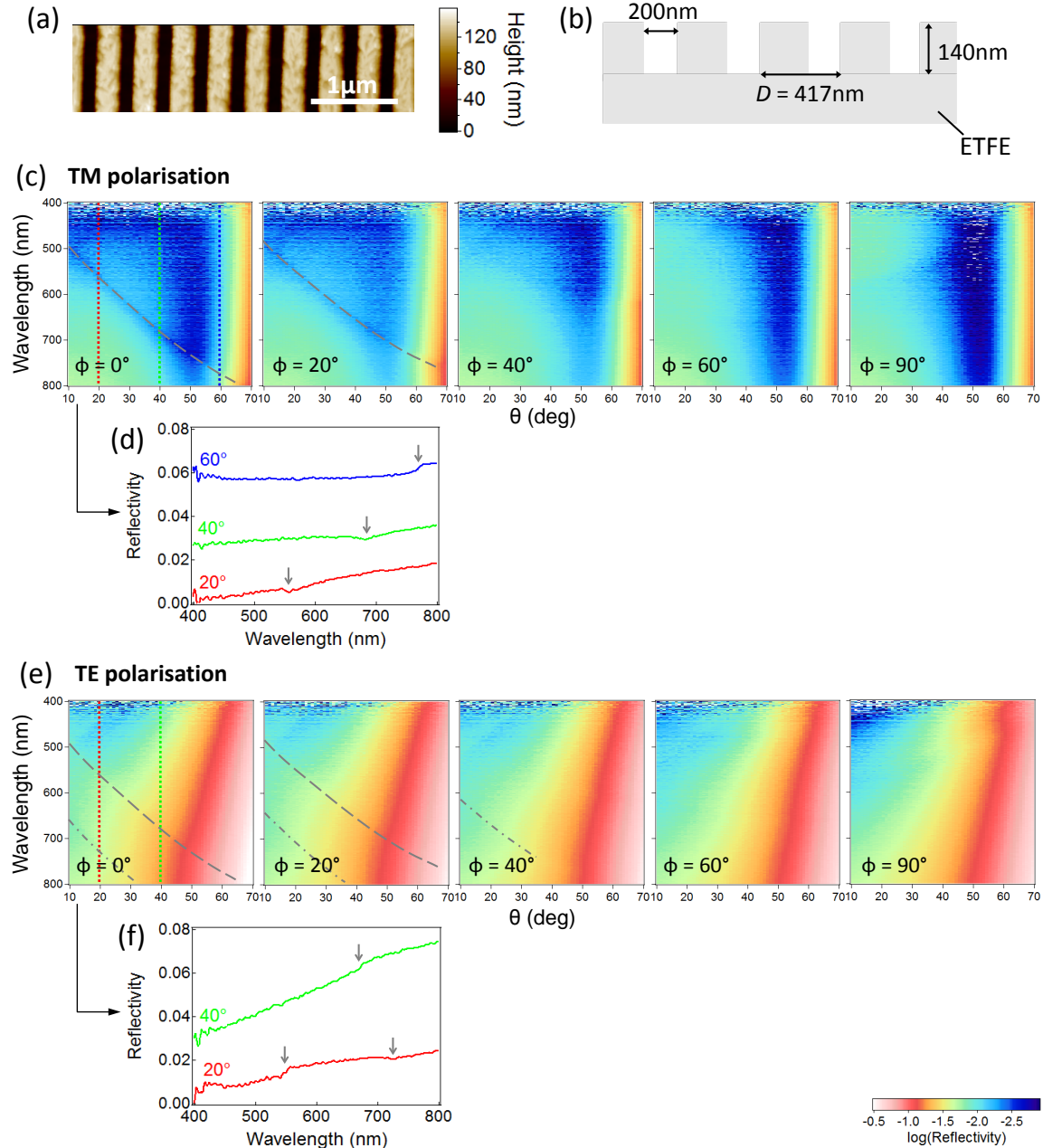


Fig. 7.2 (a) AFM image and (b) schematic structure of $D = 417\text{ nm}$ ETFE grating. (c) TM polarised reflectivity scans of ETFE grating at labelled ϕ , and (d) reflectivity spectra at indicated θ values for $\phi = 0^\circ$. (e,f) Same as above for TE polarisation. Photonic grating modes are indicated by grey lines/arrows on reflectivity scans/spectra.

TM scans at $\theta \approx 50^\circ$ due to the Brewster angle of ETFE.

7.3.2 CHPI-coated ETFE gratings

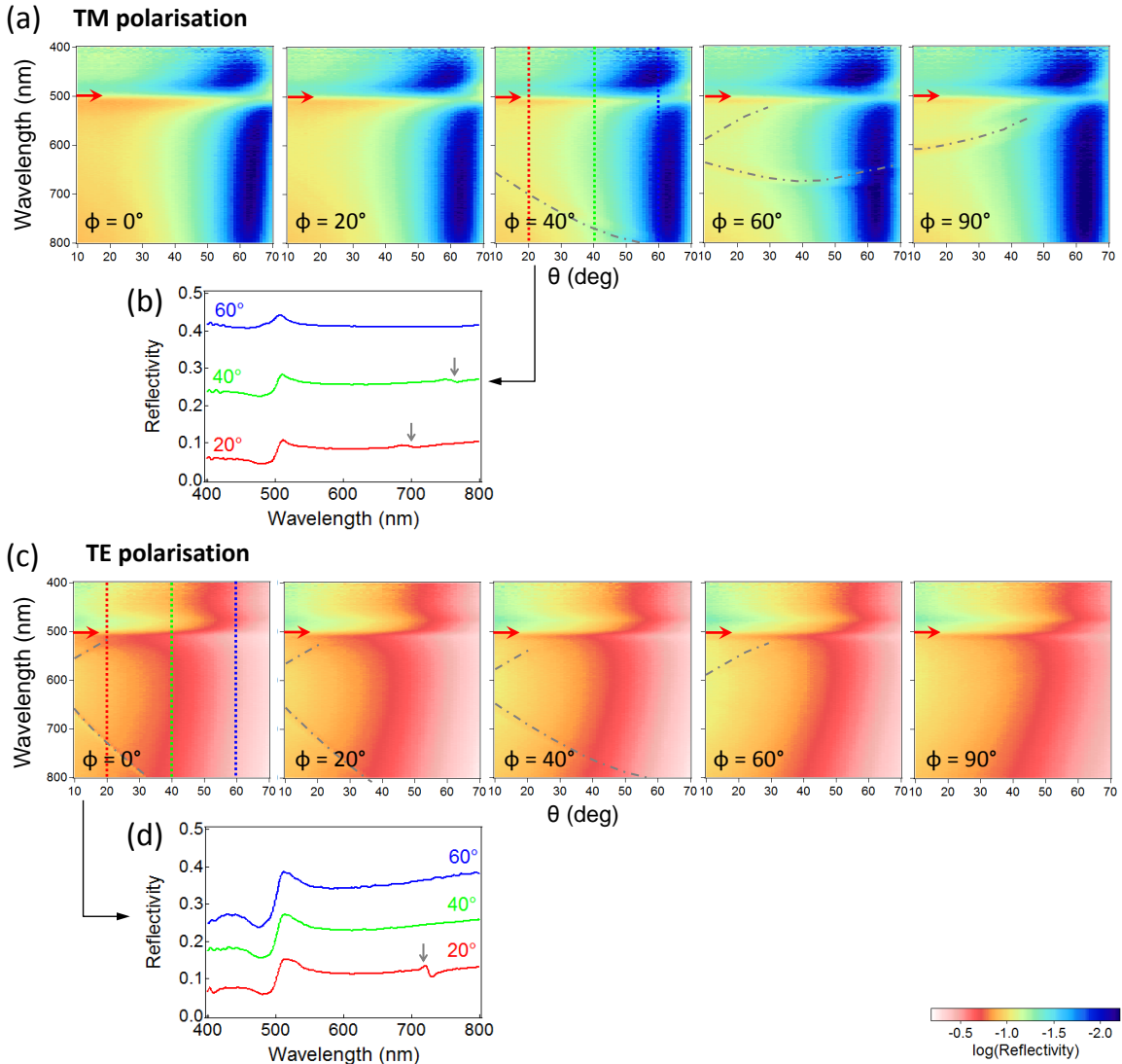


Fig. 7.3 (a) TM polarised reflectivity scans of $D = 417$ nm CHPI-coated ETFE grating at labelled ϕ , and (b) reflectivity spectra at indicated θ values for $\phi = 40^\circ$. (c) Same as (a) for TE polarisation and (d) reflectivity spectra at indicated θ for $\phi = 0^\circ$. Photonic grating modes are indicated by grey lines/arrows on reflectivity scans/spectra, and excitons by red arrows.

The exciton resonance at 505 nm dominates both the TM and TE reflectivity scans of CHPI-coated $D = 417$ nm ETFE gratings [Figs. 7.3(a,c)]. The $m = \pm 1, n = 1.4$ diffractive photonic grating modes are again visible [grey dot-dashed lines on Fig. 7.3(a,c)], and appear as Fano resonances in reflectivity due to interaction with the reflectivity of the CHPI film [Figs. 7.3(b,d)]. In TM polarisation the diffractive modes are strongest for $\phi = 90^\circ$, while

for TE they are strongest at $\phi = 0^\circ$, thus coupling with photons is strongest when the E -field is parallel to grating lines. Note there are no interactions between grating modes and excitons in this system. The Brewster angle in TM scans has now changed to $\theta \approx 62^\circ$ due to the larger refractive index of CHPI.

7.4 Non-plasmonic metal gratings

7.4.1 Ti gratings

SEM image of a $D = 417$ nm Ti grating shows the roughness of sputtered Ti film on ETFE [Fig. 7.4(a)], while AFM measurements reveal a trapezoidal grating profile due to the nanoimprinting process. Heating and cooling of ETFE during sputtering also appears to have changed the grating periodicity D , as the photonic grating modes in reflectivity scans [Figs. 7.4(c,e)] are best fit to $D = 410$ nm [Eq. 3.7]. Aside from the change in geometry, the appearance of $m = -1$ grating modes in optical spectra is very similar to that of of ETFE gratings, with modes appearing as dips in reflectivity. However the coupling to photons is much weaker in TE polarisation, as the E -field is parallel to grating lines [Sec. 3.3].

7.4.2 CHPI-coated Ti gratings

Polarised reflectivity spectra of CHPI-coated planar Ti film [Fig. 7.5] show the appearance of an exciton resonance at 505 nm, indicating the excitons are unaffected by the metal film below. The experimental data fits well to transfer matrix simulations of 70 nm CHPI-coated 120 nm Ti film, and the differences observed can be attributed to non-uniformity and roughness in both the CHPI and Ti films.

AFM measurements show the metal grating is completely immersed in a non-uniform coating for $D = 417$ nm CHPI-coated Ti grating [Figs. 7.6(a,b)]]. As with CHPI-coated ETFE gratings, the exciton resonance at 505 nm dominates reflectivity spectra for both polarisations [Figs. 7.6(c,e)]. Although very weak dips can be seen to indicate diffractive $m = -1$ grating modes in TM polarisation [Fig. 7.6(d)], coupling of TE-polarised light to grating modes is so weak that spectra appear almost identical to that of a CHPI-coated planar Ti film [Fig. 7.6(f)]. In both cases there are no interactions between CHPI excitons and modes of the Ti grating.

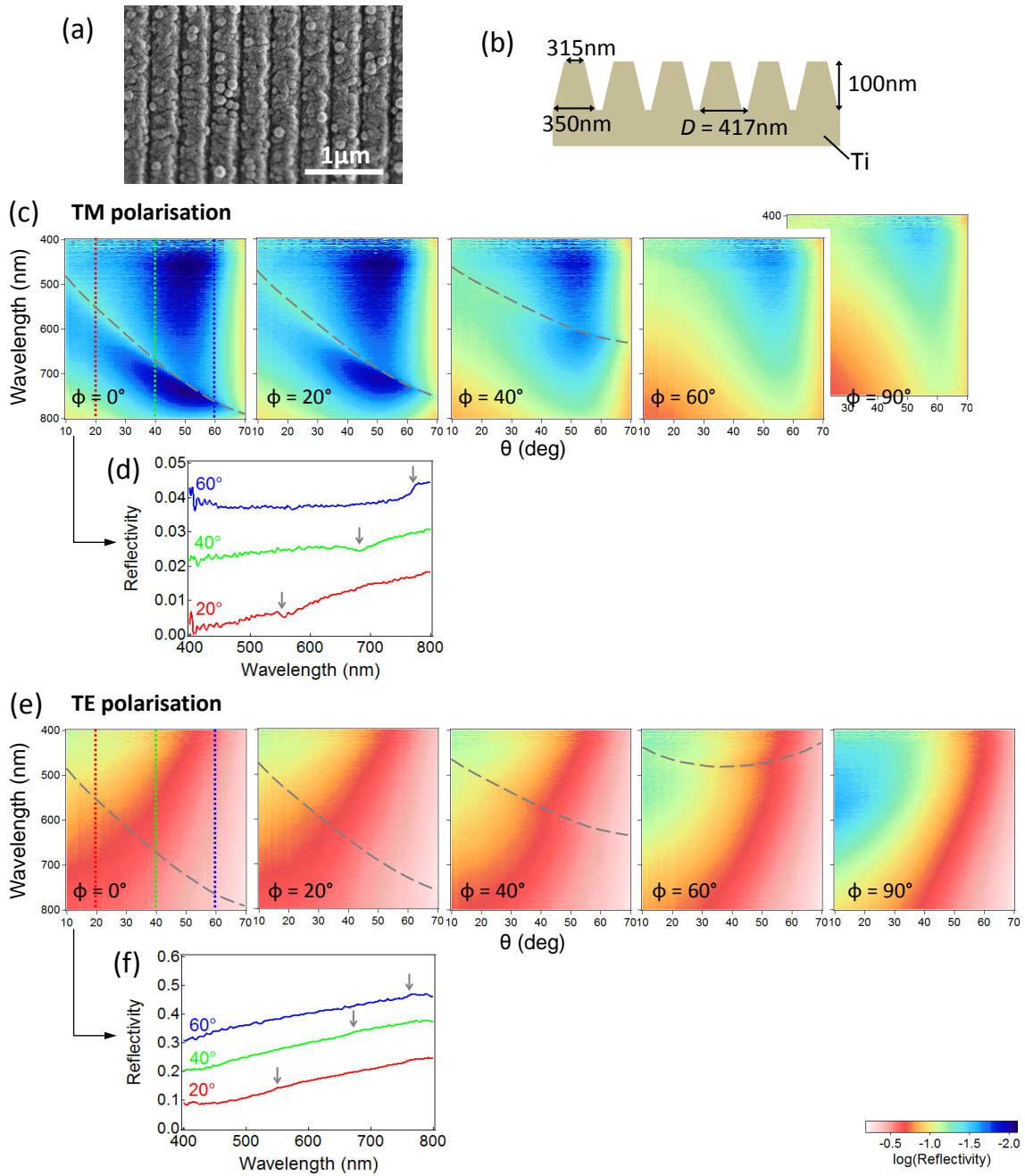


Fig. 7.4 (a) SEM image and (b) schematic structure of $D = 417\text{ nm}$ Ti grating. (c) TM polarised reflectivity scans of Ti grating at labelled ϕ , and (d) reflectivity spectra at indicated θ values for $\phi = 0^\circ$. (e,f) Same as above for TE polarisation. Photonic grating modes are indicated by grey lines/arrows on reflectivity scans/spectra.

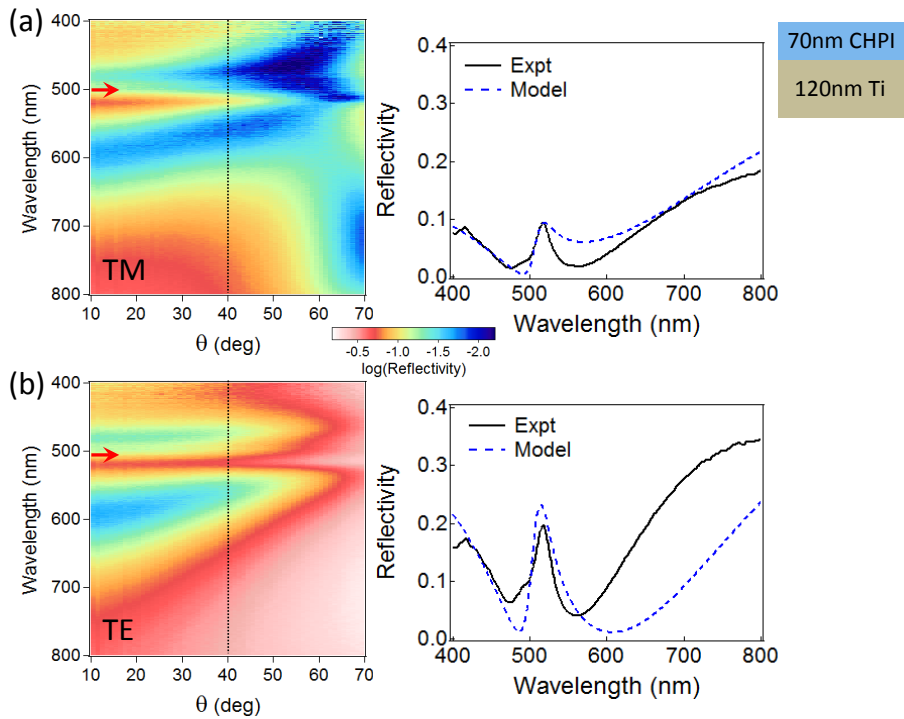


Fig. 7.5 Specular reflectivity scans of 70 nm CHPI film on 120 nm planar Ti film (schematic top right) with (a) TM and (b) TE polarised light. Excitons are marked by red arrows. Spectra at $\theta = 40^\circ$ are plotted with those predicted by transfer matrix simulations (right).

7.5 Plasmonic metal gratings

7.5.1 Ag gratings

Fig. 7.7 shows reflectivity scans for Ag gratings, $D = 556, 417$ and 278 nm. The spectra for all three gratings show the same features: in TM polarisation a sharp threshold anomaly whose dispersion follows Eq. 3.7 with $m = \pm 1$ modes (grey dashed lines), and a redshifted dip follows for the resonance anomaly indicating the presence of excited SPPs (black dashed lines). In TE polarisation we don't observe any anomaly features due to the inability to excite SPPs, instead we see the $m = \pm 1$ photonic modes.

Concentrating on the $D = 417$ nm grating, we see that the sputtered Ag film on ETFE shows some roughness [Fig. 7.8(a)], and AFM measurements indicate a square-wave grating with depth 140 nm and slit width 130 nm [Fig. 7.8(b)]. In reflectivity the threshold anomalies (grey dashed lines) shift as expected according to Eq. 3.7 in TM polarisation [Fig. 7.8(c)], and appear as sharp changes in the intensity [Fig. 7.8(d)]. The redshifted resonance anomalies (black dashed lines) become weaker with increasing ϕ and is no longer observed when $\phi > 60^\circ$ as it becomes harder for photons to couple to SPPs in this polarisation. For the same

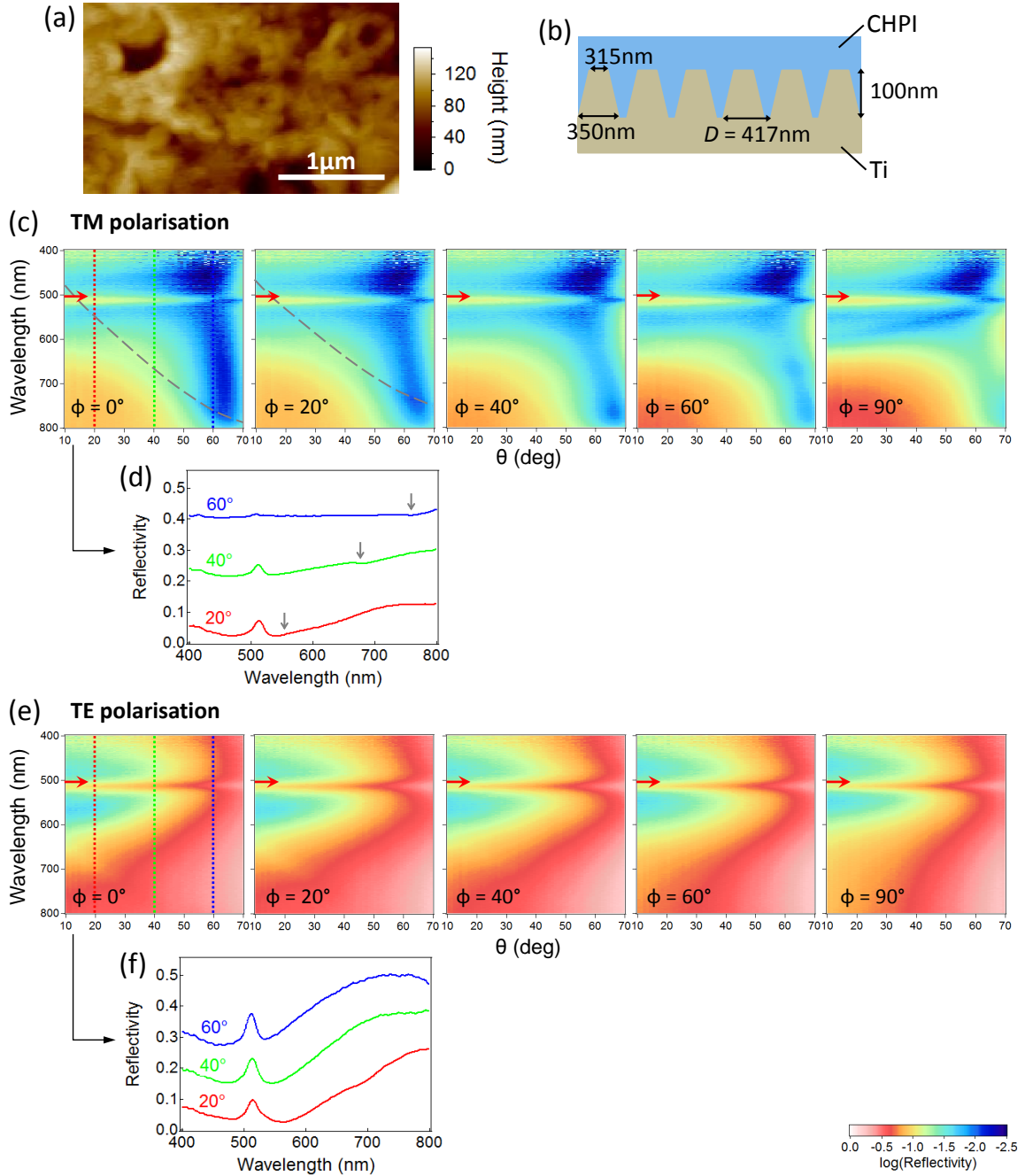


Fig. 7.6 (a) AFM image and (b) schematic structure of $D = 417\text{ nm}$ CHPI-coated Ti grating. (c) TM polarised reflectivity scans of $D = 417\text{ nm}$ CHPI-coated Ti grating at labelled ϕ , and (d) reflectivity spectra at indicated θ values for $\phi = 0^\circ$. (e,f) Same as above for TE polarisation. Photonic grating modes are indicated by grey lines/arrows on reflectivity scans/spectra, and excitons by red arrows.

reason no anomalies are observed in TE polarisation at low ϕ , where the photonic modes

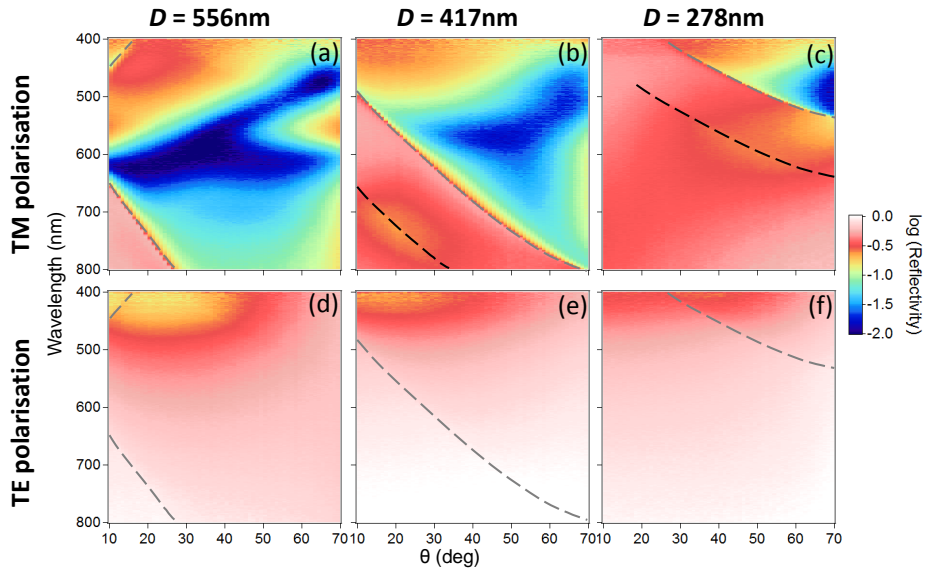


Fig. 7.7 Specular reflectivity scans of uncoated Ag gratings with the labelled periodicity D and polarisation of light. Photonic grating modes (threshold anomalies) are marked by grey dashed lines, and plasmonic grating modes (resonance anomalies) are marked by black dashed lines.

appear weakly in spectra [Fig. 7.8(f)]. We would expect to observe anomalies at $\phi = 90^\circ$ in TE polarisation, however the energy of the mode is too high for our measurement range here. The broad dip seen at $\phi = 60^\circ$ in both polarisations and $\phi = 90^\circ$ in TE polarisation is assigned to the Fabry-Perot interference mode of light reflected from the top and bottom surfaces of the grating. This mode doesn't change in position with ϕ and extrapolates to ~ 600 nm at $\theta = 0^\circ$, which fits the height of the gratings as seen in AFM measurements.

We use the finite element method (FEM) to model the electromagnetic nearfield of grating modes in order to understand their behaviour. The modelled spectrum for $\phi = 0^\circ$, $\lambda = 600$ nm agrees very well with the features of the experimental data [Fig. 7.9(a)], but has a larger reflectivity overall as the model does not take into account the roughness of the Ag film. Low efficiency of the specularly reflected grating order gives rise to the low reflection region seen at high θ . Instead the coupling is strongest to the -1 diffracted order, as shown in Fig. 7.9(b). The modelled H_z field component for $\phi = 0^\circ$, $\theta = 30^\circ$, $\lambda = 700$ nm [Fig. 7.9(c)] shows that the resonance anomaly does indeed behave like SPP travelling on the surface of the metal.

The position of the threshold anomaly is fixed by the periodicity of the structure, however as the resonance anomaly is caused by the interference between diffracted light and SPPs we expect the position of this to be much more sensitive to the geometry of the grating.

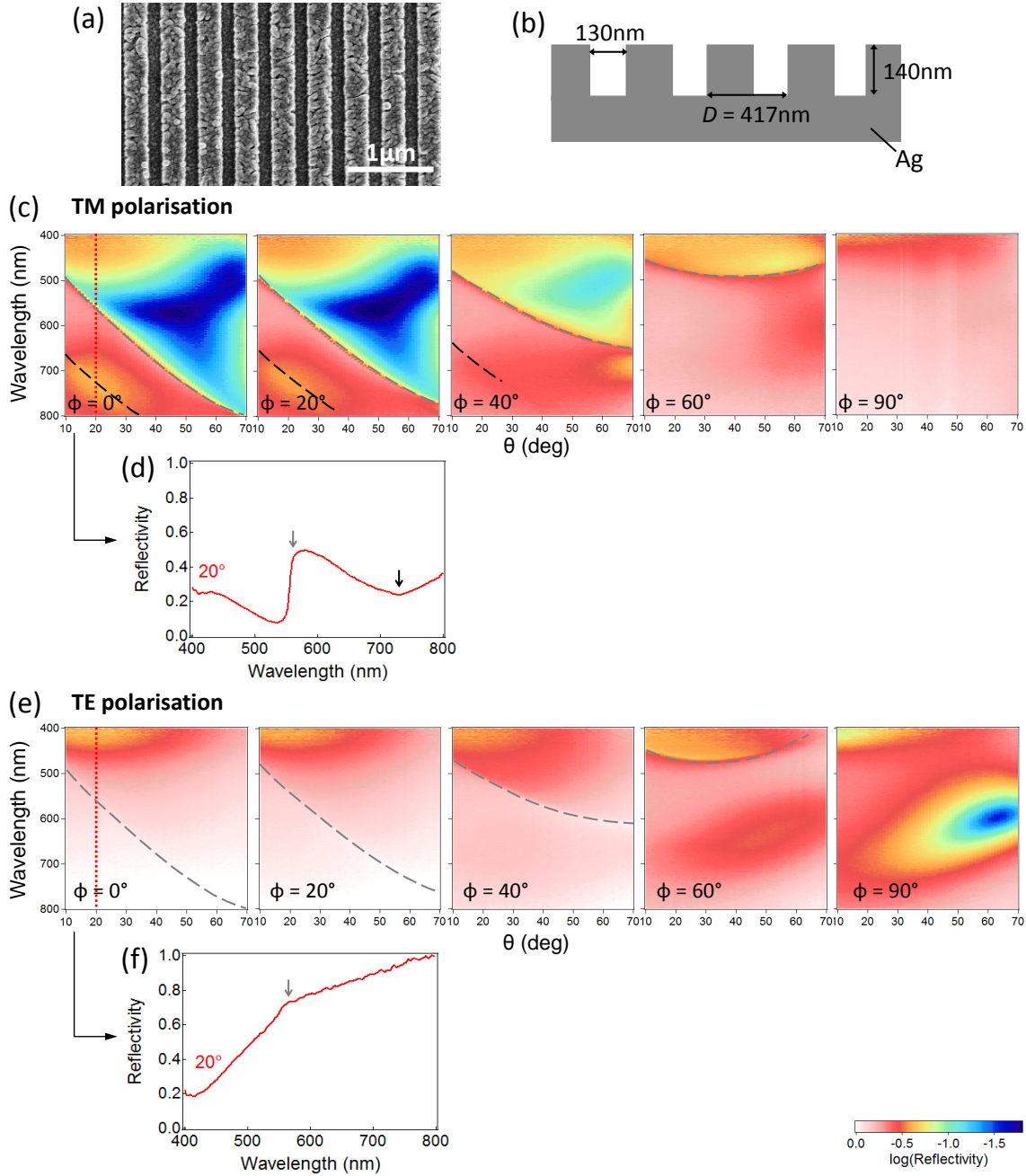


Fig. 7.8 (a) SEM image and (b) schematic structure of $D = 417\text{ nm}$ Ag grating. (c) TM polarised reflectivity scans of $D = 417\text{ nm}$ Ag grating at labelled ϕ , and (d) reflectivity spectra at indicated θ values for $\phi = 0^\circ$. (e,f) Same as above for TE polarisation. Photonic grating modes (threshold anomalies) are indicated by grey lines/arrows on reflectivity scans/spectra, and plasmonic gratings modes (resonance anomalies) by black lines/arrows.

Fig. 7.10 shows the structures and TM reflectivity scans at $\phi = 0^\circ$ of three different gratings, ranging from square-wave [Fig. 7.10(a)] to more sinusoidal profiles [Fig. 7.10(b,c)].

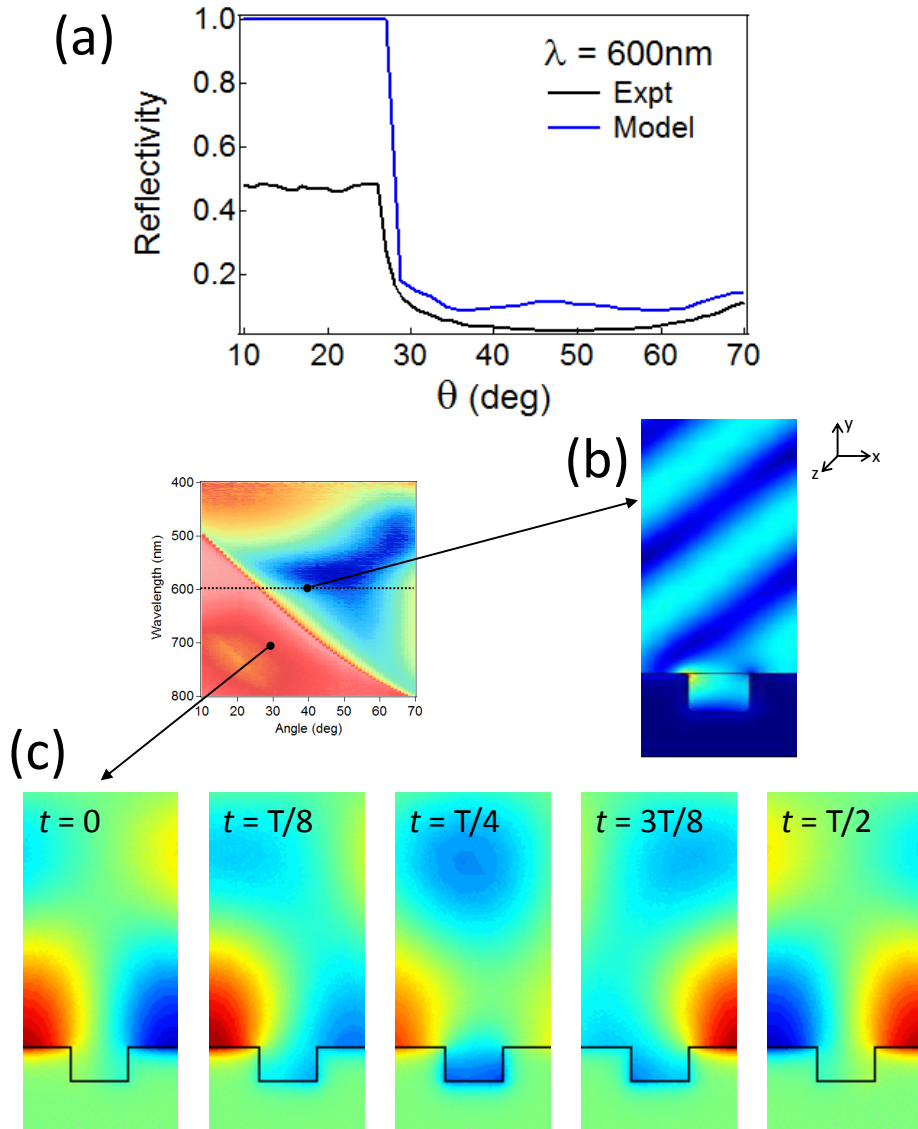


Fig. 7.9 (a) Experimental and modelled TM reflectivity spectra of $D = 417$ nm Ag grating for $\phi = 0^\circ$, $\lambda = 600$ nm. (b) Time averaged E -field intensity ($\vec{E} \cdot \vec{E}$) profile for $\lambda = 600$ nm, $\theta = 40^\circ$. (c) H_z nearfield profile at time t of the optical cycle T for $\lambda = 700$ nm, $\theta = 30^\circ$.

We see the sharp threshold anomalies (grey dashed lines) remain in the same position for all three gratings, barring small changes in D as a result of the sputtering process. However the widths and positions of the resonance anomalies vary greatly with geometry, and the sharpest resonances are produced by sinusoidal gratings. We also observe a dispersionless mode at ~ 450 nm in Figs. 7.10(b,c) that may be due to the presence of channel plasmons, which require a narrowing of the grating slit as seen in the sinusoidal gratings.

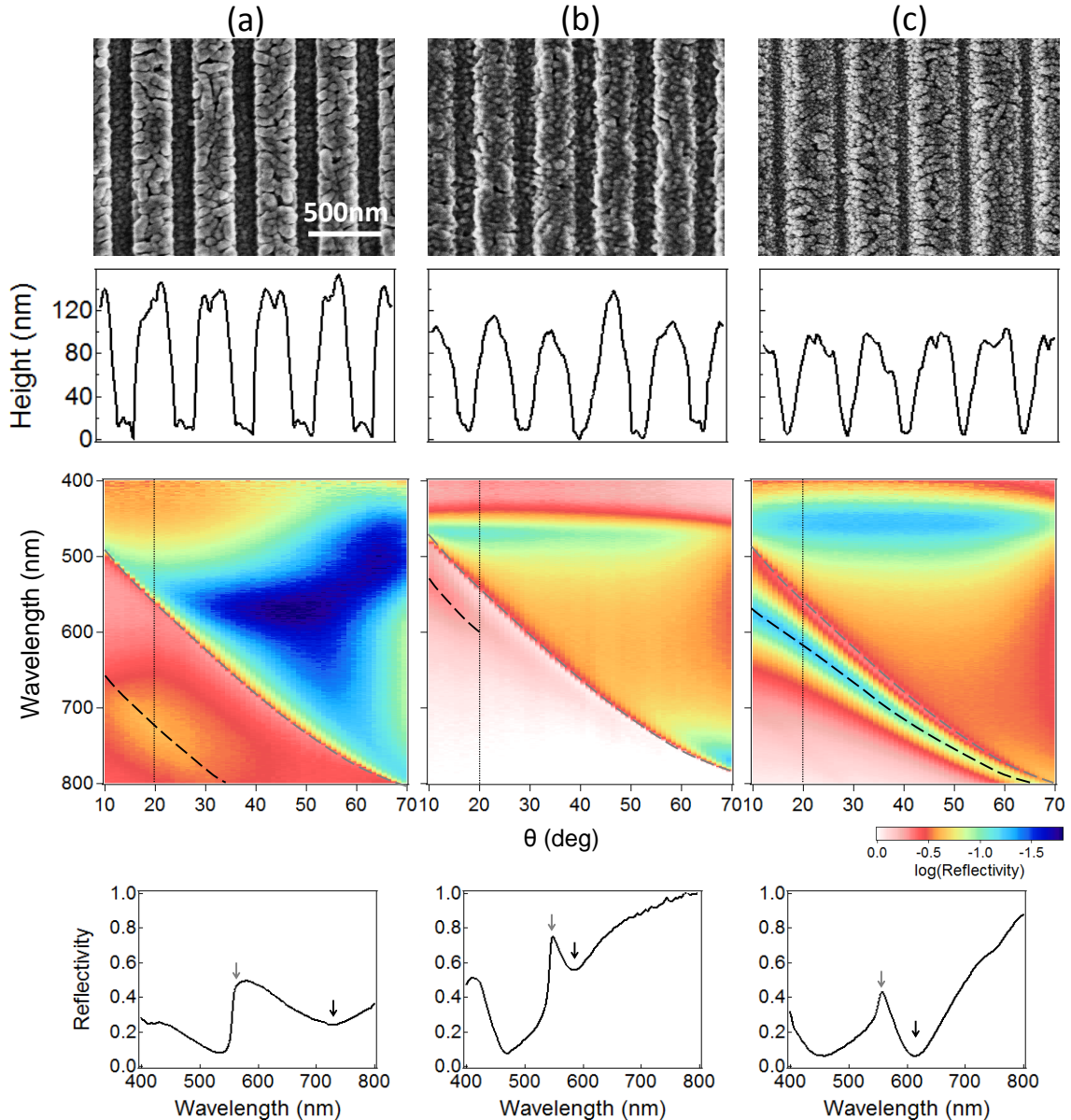


Fig. 7.10 (From top) SEM image, AFM profile, TM specular reflectivity scans at $\phi = 0^\circ$, and reflectivity spectra at $\phi = 0^\circ$, $\theta = 20^\circ$ for three $D = 417\text{ nm}$ Ag gratings. Photonic grating modes (threshold anomalies) are marked by grey dashed lines/arrows, and plasmonic grating modes (resonance anomalies) by black dashed lines/arrows on reflectivity scans/spectra.

7.5.2 PS-coated Ag gratings

From the AFM image of a $D = 417\text{ nm}$ PS-coated grating [Fig. 7.11(a)] we see that the Ag grating is almost submerged beneath the non-uniform PS layer, resulting in a shallow sinusoidal grating with an average height of 5 nm [Fig. 7.11(b)]. The presence of the PS overcoating increases the complexity of the reflectivity spectra by allowing access to more

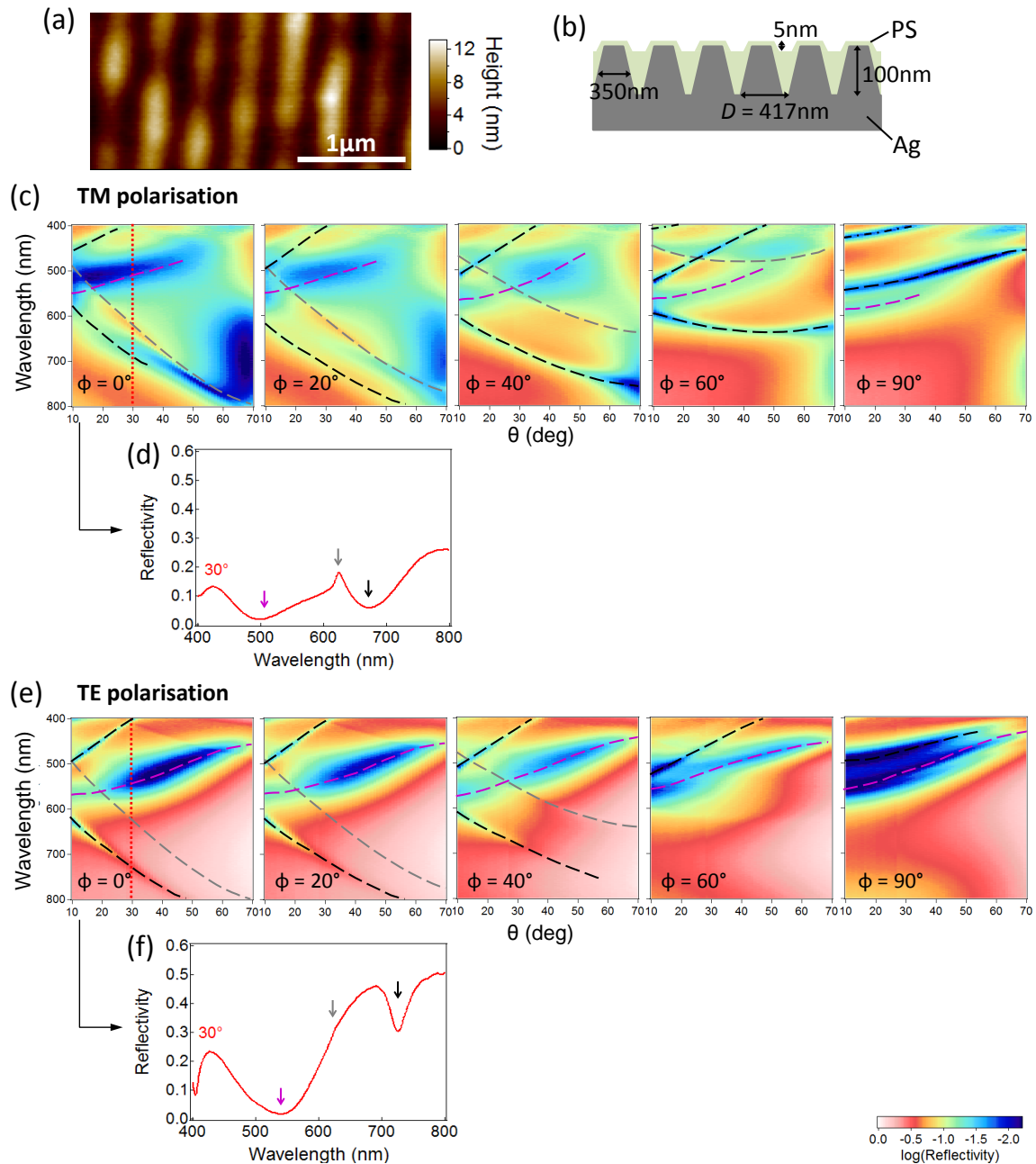


Fig. 7.11 (a) AFM image and (b) schematic structure of $D = 417\text{ nm}$ PS-coated Ag grating. (c) TM polarised reflectivity scans of PS-coated Ag grating at labelled ϕ , and (d) reflectivity spectra at indicated θ value for $\phi = 40^\circ$. (e) Same as above for TE polarisation, and (f) reflectivity spectra at indicated θ value for $\phi = 0^\circ$. Photonic grating modes are indicated by grey lines/arrows on reflectivity scans/spectra, plasmonic gratings modes by black lines/arrows, and waveguide modes by purple lines/arrows.

modes. In both TM and TE polarisation, photonic (grey dashed lines) and redshifted plas-

monic modes (black dashed lines) can be observed [Fig. 7.11(c,e)], however the photonic mode is much weaker in TE polarisation. At high ϕ in TM polarisation, a second set of plasmonic modes can be seen (black dot-dashed lines), likely due to different PS thickness at the top and bottom surface of the grating. We also see a broader mode at ~ 560 nm for $\phi = 0^\circ$, $\theta = 10^\circ$ in both polarisations, which remains in roughly the same position for all ϕ (purple dashed line).

Using FEM modelling, we observe two types of modes at $\phi = 90^\circ$ in TM polarisation. A mode at higher energy has field intensity concentrated at the top surface of the grating, and evanescently decays from the Ag surface [Fig. 7.12(a)]. Taking snapshots throughout the optical cycle, the mode appears to be a quasiparticle travelling along the top surface of the grating [Fig. 7.12(b)]. By varying the geometry of the grating, we find the mode decreases in energy as D increases, increases in energy with the slit width, and is unaffected by grating height, thus showing the behaviour expected for an SPP mode. On the other hand, the field intensity of the lower energy mode is mainly concentrated in the slit of the grating [Fig. 7.12(c)], and appears to travel along the slit [Fig. 7.12(d)]. The energy of the mode is unaffected by D or the grating height, and decreases as the slit width increases, the behaviour of a mode waveguided by the grating slit. According to Eq. ??he dispersion fits that of a TE_{10} mode.

Both SPP and waveguided modes are very sensitive to the dielectric environment as shown by Eqs. 3.7 and 3.10, and Fig. 7.13 shows the change in these modes with increasing PS thickness. Both the narrower SPP resonances (black dashed lines) and broader waveguided modes (purple dashed lines) redshift with increasing PS coverage as expected. For the structure in Fig. 7.13(c) these two modes actually overlap, although no interactions occur.

7.5.3 CHPI-coated Ag gratings

Fig. 7.14 shows TM reflectivity scans for CHPI-coated Ag gratings, $D = 556$, 417 and 278 nm at $\phi = 0$ and 90° . The spectra for $D = 556$ and 417 nm are very similar, showing two exciton modes (red arrows) that strongly couple to an SPP grating mode (black dashed line) as the oscillations become resonant at $\phi = 90^\circ$. Two excitons can also be observed for $D = 278$ nm, however the SPP mode is at a higher energy and thus the coupling occurs at $\phi = 0^\circ$.

TM polarised reflectivity scans of a CHPI-coated Ag grating at $\phi = 0^\circ$ [Fig. 7.15(a)] show two dispersionless exciton modes at 480 and 500 nm (marked by arrows) far off resonance with grating modes. The persistent presence of a second exciton is only detected

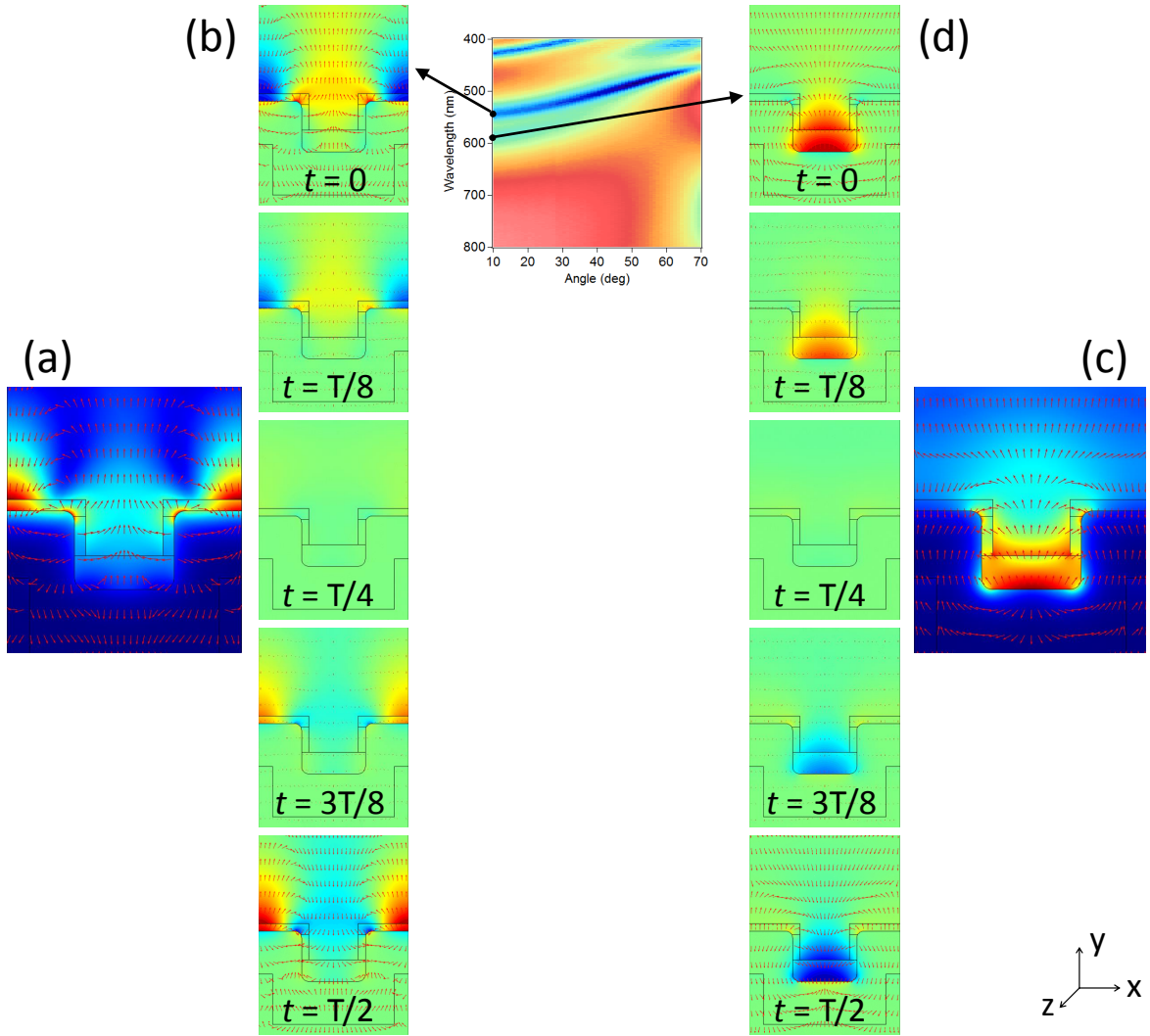


Fig. 7.12 (a) Time averaged and (b) snapshots at time t in the optical cycle T of the E_y nearfield intensity for the higher energy (plasmonic) mode at $\phi = 90^\circ$, $\theta = 10^\circ$. (c,d) Same as above for the lower energy (waveguide) mode. The arrows represent the size and direction of the E -field vector.

when SPPs can be excited, i. e. in TM polarisation [Fig. 7.15(a)] but not TE [Fig. 7.15(b)], nor in CHPI-coated planar Ag films [Fig. 7.15(c)]. It is also not observed for CHPI-coated non-plasmonic gratings [Figs. 7.3 and 7.6], thus from Fig. 7.15 we deduce that SPP excitation leads to the observation of an additional redshifted exciton with a splitting of 100 meV. Its appearance only when SPPs are present rules out any influence from modified CHPI assembly in the grooves, which are in any case hundreds of times larger than the PbI layer spacing. We note slight changes in the CHPI coverage alter the positions and intensities of dispersive grating modes [*cf* Fig. 7.17(c), with a thinner CHPI coating], however the exciton

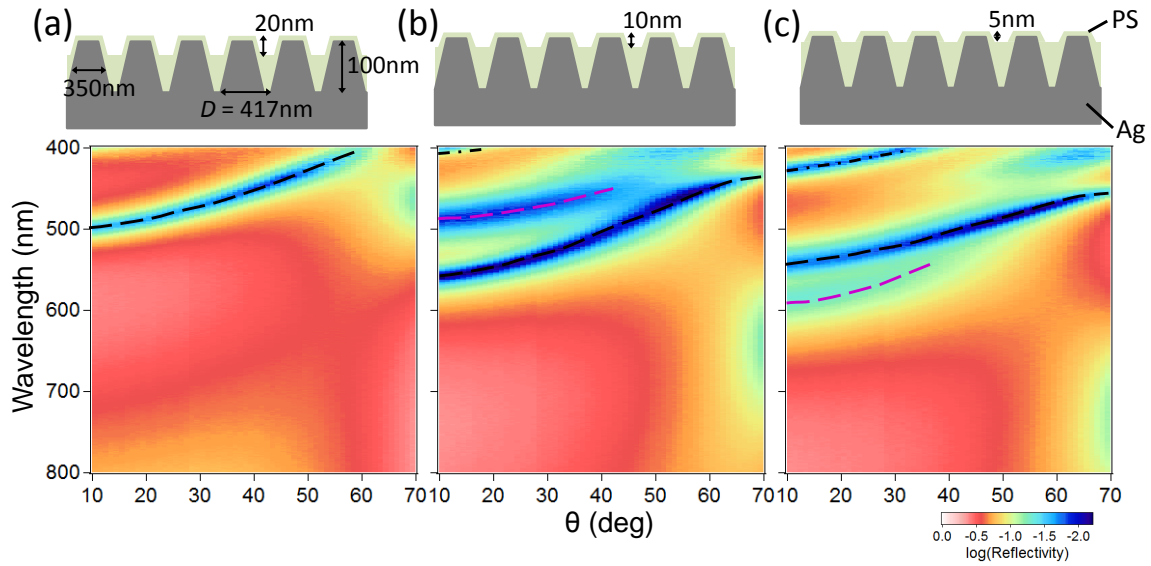


Fig. 7.13 Schematic structure of PS-coated $D = 417\text{ nm}$ Ag gratings (top), and TM polarised reflectivity scans at $\phi = 90^\circ$ (bottom). PS thickness increases from (a) - (c). Plasmonic modes are indicated by black lines, and waveguide modes by purple lines.

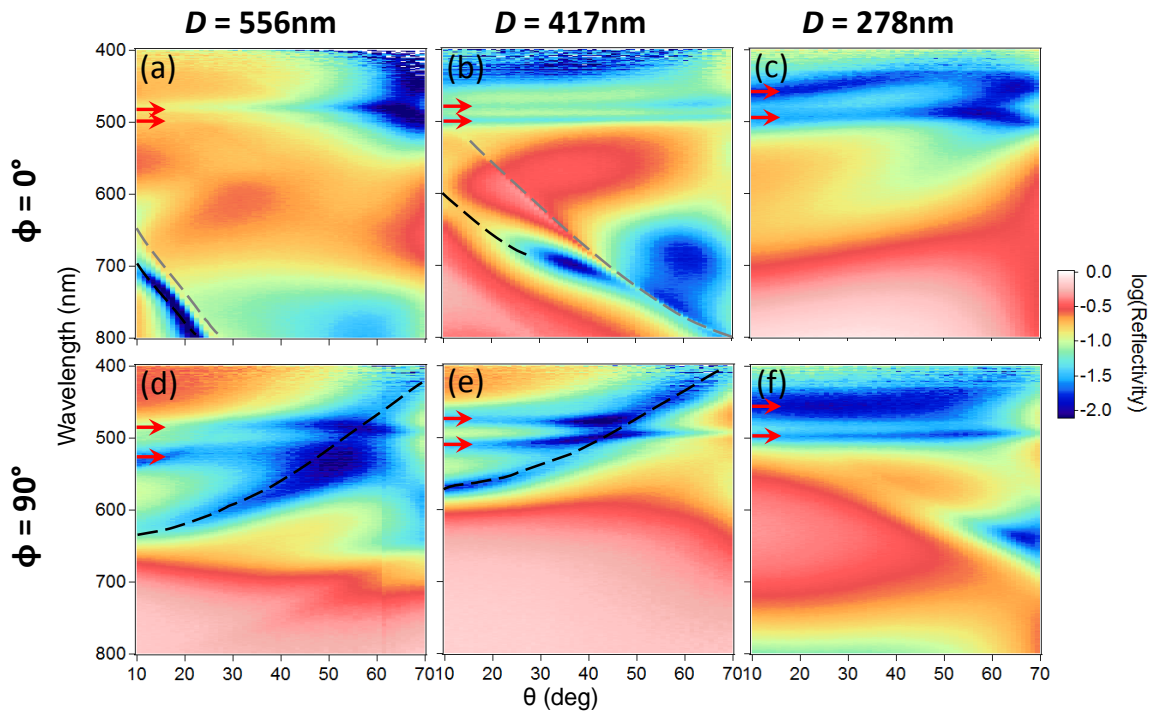


Fig. 7.14 TM specular reflectivity scans of CHPI-coated Ag gratings with the labelled D and ϕ . Photonic grating modes are marked by grey dashed lines, plasmonic grating modes by black dashed lines, and excitons indicated by red arrows.

modes remain essentially unchanged.

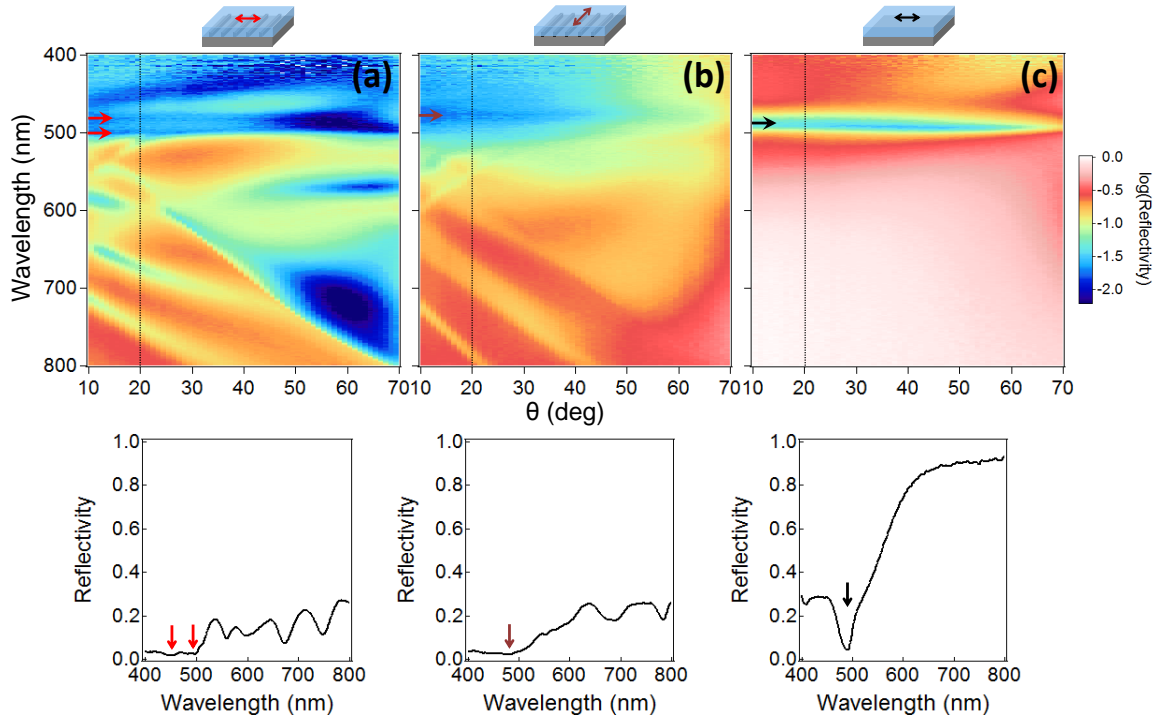


Fig. 7.15 Specular reflectivity scans at $\phi = 0^\circ$: CHPI-coated Ag grating with (a) TM and (b) TE polarised light, and (c) CHPI-coated 120 nm planar Ag film with TM polarised light. The electric field orientation is shown above each scan, the reflectivity spectra at $\theta = 20^\circ$ below, and positions of exciton modes are indicated by arrows.

It is well known that the emitted energy of a dipole (exciton) is lowered when placed in front of a metallic surface due to interactions between the dipole and the reflected electromagnetic field [186–191]. Using the method of images, we can replace the metal and describe instead the coupling between an exciton in the CHPI (ϵ_1) and its image exciton in the metal (ϵ_2), modified by their respective dielectric environments. Chance *et al.* [189] showed the redshift in the emitted energy of an exciton (ΔE_{ex}) oriented parallel to the interface can be approximated by

$$\Delta E_{ex} \sim \left(\frac{k_1}{l} \right)^3 \text{Re} \left\{ \frac{\epsilon_2 - \epsilon_1}{\epsilon_2 + \epsilon_1} \right\} \Gamma_0, \quad (7.1)$$

where l is the distance between the exciton and a metal surface, k_1 is the wavenumber of light in CHPI, and Γ_0 is the inverse exciton radiative lifetime without the metal. From this we can see the l^{-3} dependence of the redshift as shown in Fig. 7.16(a), where the experimentally observed $\Delta E_{ex} \sim 100$ meV corresponds to $l \sim 22$ nm, close to the experimentally-determined

CHPI thickness. Clearly ΔE_{ex} is also affected by the dielectric response of CHPI and Ag, and from Eq. 7.1 we see that ΔE_{ex} is maximised if $\epsilon_2 + \epsilon_1 \rightarrow 0$, i. e. when emission is resonant with an SPP on the metal-dielectric interface.

The role of the SPP in this case is to outcouple the signal of the redshifted exciton. There are three main decay channels for dipole emission near a metal surface: direct emission to photons, emission to SPPs, and nonradiative processes such as the excitation of electron-hole pairs and lossy surface waves on the metal. Other nonradiative paths via defects or phonons are independent of l and will be ignored in this analysis. Emission into SPPs provides an extra radiative decay channel as this signal can be extracted to the far field via the periodic nanostructure, and this mechanism has been used to improve the luminescence efficiency of light emitting devices [192, 193]. The relative decay probability for each process is calculated as a function of l [191] and shown in Fig. 7.16(a). Up to a CHPI thickness of 25 nm, SPP mediated emission is the most important radiative decay channel with a maximum emission probability at 22 nm, matching the experimentally observed ΔE_{ex} . Even for thicker CHPI films we expect the exciton modes to remain at the same positions, because SPP emission becomes weak at large l where ΔE_{ex} is negligible.

In our MQW perovskite system, localised excitons in periodically-spaced nearby QWs are optically coupled together to form collective exciton-polariton states an average distance l from the Ag surface [194–197]. Therefore in CHPI-coated Ag gratings we observe both in-plane exciton-polaritons, and out-of-plane interactions that lead to ‘image-biexcitons’, which are outcoupled via SPP emission with a binding energy of 100 meV at room temperature [Fig. 7.16(b)]. For our grating system, the exciton and SPP modes become closer in energy with increasing ϕ [see below and Fig. 7.17(c)], and as a result splitting between the exciton modes (indicated by arrows in Fig. 7.17(c)) increases to around 185 meV at $\phi = 90^\circ$. The azimuthal dependence of the exciton splitting reflects the tuneable modification of the Coulomb interaction in this geometry, but however requires further theoretical development.

AFM image of the CHPI-coated Ag grating clearly shows a grating structure despite the roughness of CHPI coating [Fig. 7.17(a)]. Using AFM measurements, we find CHPI forms a conformal coating around the Ag grating with thickness ~ 25 nm [Fig. 7.17(c)]. In TE polarisation, we only observe the presence of one exciton without the signature of any grating modes, similar to the CHPI-coated Ti gratings. In TM polarised reflectivity scans, as well as strong excitons (red arrows) we also observe $m = \pm 1$ photonic and plasmonic grating modes [Fig. 7.17(c)]. As the SPP modes become resonant with the exciton and image exciton, the light-matter modes strongly couple and produce an anticrossing in the

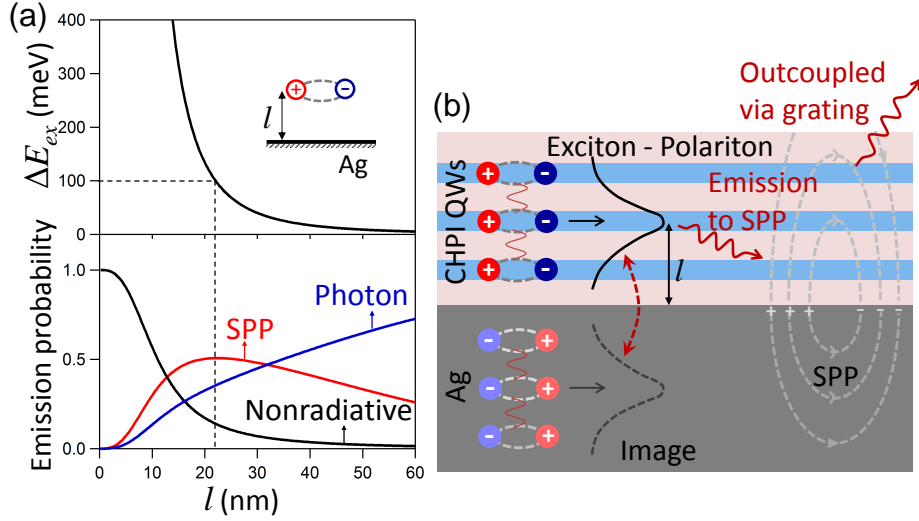


Fig. 7.16 (a) Change in emitted energy (top) and relative decay probabilities (bottom) of an exciton with energy 2.6 eV placed distance l from the Ag surface. The dashed line indicates the experimentally measured redshift. (b) Schematic mechanism for SPP-mediated emission of image-biexciton.

reflectivity of 0.25 eV. Extracting the mode positions from the $\phi = 90^\circ$ scan [Fig. 7.17(c)] allows them to be fit to a three oscillator model using the Hamiltonian

$$\hat{H} = \begin{pmatrix} E_{ex} & 0 & \Omega_{ex}/2 \\ 0 & E_{bx} & \Omega_{bx}/2 \\ \Omega_{ex}/2 & \Omega_{bx}/2 & E_{pl} \end{pmatrix}, \quad (7.2)$$

where E_{ex} , E_{bx} and E_{pl} are the energies of the exciton-polariton, image-biexciton and plasmonic grating modes respectively, while Ω_{ex} and Ω_{bx} represent the interaction between the SPP and exciton/image-biexciton. From this we find Rabi splittings of $\Omega_{ex} = 150$ meV and $\Omega_{bx} = 125$ meV. These are greatly enhanced because of the large confinement of the plasmonic optical field in the thin PBI QW layers. The Rabi splitting is given by $\Omega \propto \sqrt{f_{osc}N_{QW}/V}$, where the oscillator strength (f_{osc}) of the CHPI is assumed to be similar for coupling to photons or plasmons, the number of QWs (N_{QW}) is proportional to the CHPI thickness, and the mode volume (V) is here proportional to the optical mode size. Comparing to Fabry-Perot planar CHPI microcavities in strong coupling [28] which have CHPI thickness of 72 nm, cavity length of 407 nm, and a Rabi frequency of $\Omega_{FP} = 65$ meV, the simple scaling above predicts $\Omega_{SPP} \sim \Omega_{FP} \sqrt{(22/72).(407/22)} = 156$ meV, in excellent agreement with our measurements. Using SPPs to strongly couple to the excitons thus dramatically reduces the cavity length, thus enhancing the light-matter coupling.

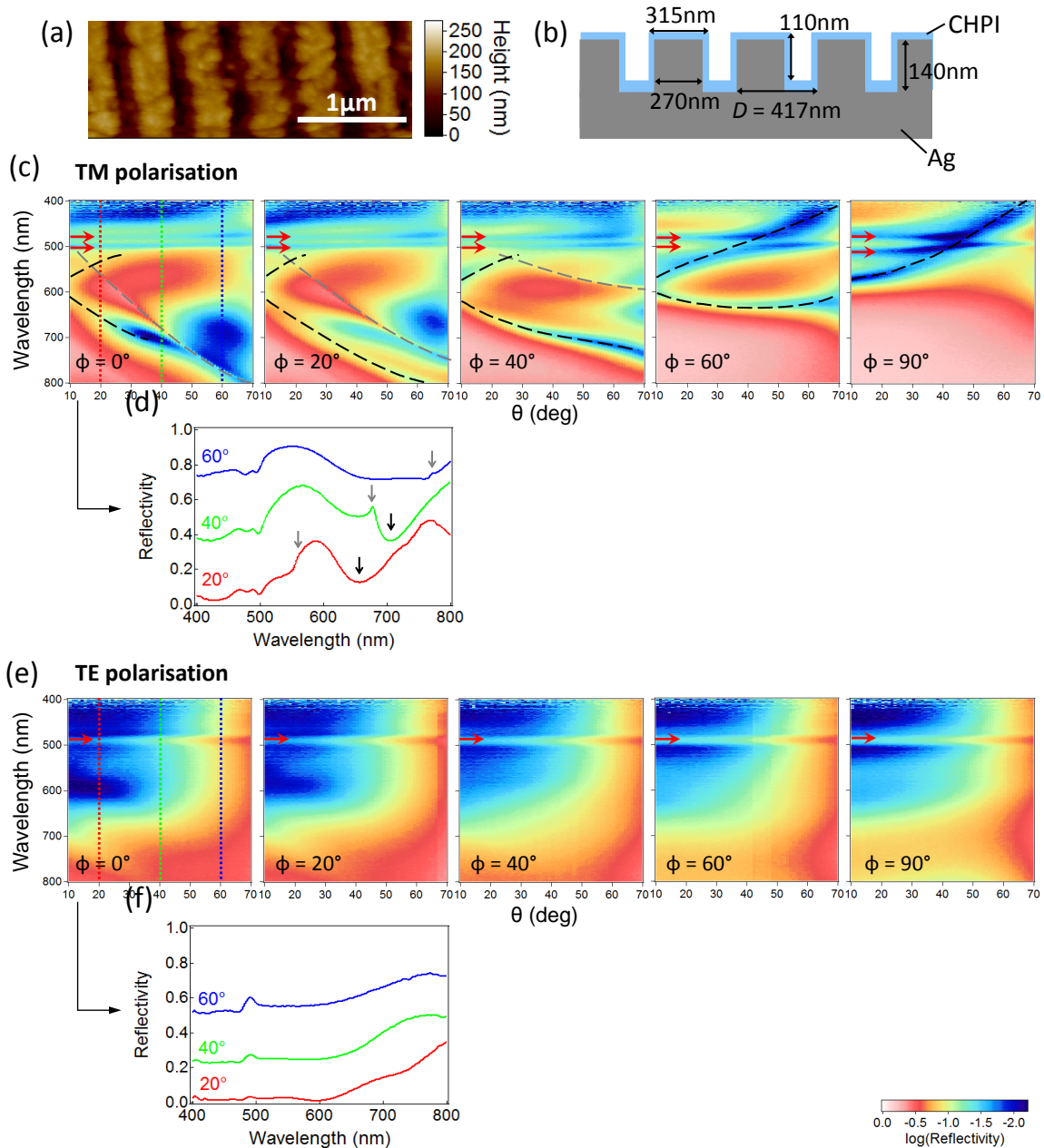


Fig. 7.17 (a) AFM image and (b) schematic structure of $D + 417$ nm CHPI-coated Ag grating. (c) TM polarised reflectivity scans of $D = 417$ nm Ag grating at labelled ϕ , and (d) reflectivity spectra at indicated θ value for $\phi = 0^\circ$. (e,f) Same as above for TE polarisation. Photonic grating modes are indicated by grey lines/arrows on reflectivity scans/spectra, plasmonic gratings modes by black lines/arrows, and excitons by red arrows.

We calculate the full eigenstates of the system using FEM simulations. These confirm the anticrossings observed, and provide the optical field profiles. In the case of strong coupling at $\phi = 90^\circ$, the time-averaged near-field shows strongest intensity inside the CHPI

which coats the bottom surface of the grating, with a rapid evanescent decay away from the interface [Figs. 7.18(b,c)]. The mode is thus both laterally confined by the grating as well as being trapped inside the surface layers where it couples to the excitons.

The SPP *E*-field direction is primarily perpendicular to the metal-dielectric interface, while excitons in CHPI QWs are polarised parallel to this interface [28, 45]. Simulated $\phi = 90^\circ$ spectra for in- and out-of-plane exciton dipoles are shown in Figs. 7.18(d,e) respectively. While strong coupling is seen for both dipole orientations, the bare exciton is only seen for the in-plane dipole. It thus appears that the coupling between the excitons and their images are responsible for mixing the dipole orientations, enabling the strong coupling with the SPP mode. The polariton states mix excitons within the perovskite which are delocalised across many PbI monolayers, with SPPs which are tightly confined to the CHPI layer above the Ag grating and laterally localised in the grating slits by the coupling of standing waves. Such light-matter polaritonic quasiparticles thus combine organic, inorganic and plasmonic components in an unusual fashion.

7.6 Conclusions

Simple plasmonic periodic structures give rise to a wide range of grating modes: photonic modes due to the interference of light, excitement of SPPs on the surface of the metal, or laterally localised modes such as channel plasmons or waveguide modes. The positions and efficiencies of many of these modes depends sensitively on the geometry of the grating and the dielectric environment provided by any overcoating materials.

In CHPI-coated Ag gratings, we observe evidence of image-biexcitons with binding energy 100 meV at room temperature. Such quasiparticles arise from the interaction between excitons and their images in the metal, and are outcoupled from the grating structure via SPP emission. These out-of-plane biexciton states mediate coupling between in-plane QW excitons and out-of-plane SPP grating modes. This enables the observation of strong coupling at room temperature with Rabi splittings of 150 and 125 meV for the exciton and image-biexciton respectively. Both the biexciton binding energy and strong coupling Rabi splitting is tuneable by small changes in the structure of the coated gratings.

Strong coupling has previously been observed between inorganic or organic excitons and Au nanoslit gratings at low temperature. The coupling constants in these systems are much smaller compared to CHPI at room temperature: 55 meV for 50 nm J-aggregate films at 77 K [198], and 8 meV for 10 nm GaAs QWs at 10 K [199]. One key difference is that for the III-V semiconductors the QWs have to be spaced at least 20 nm from the metal surface

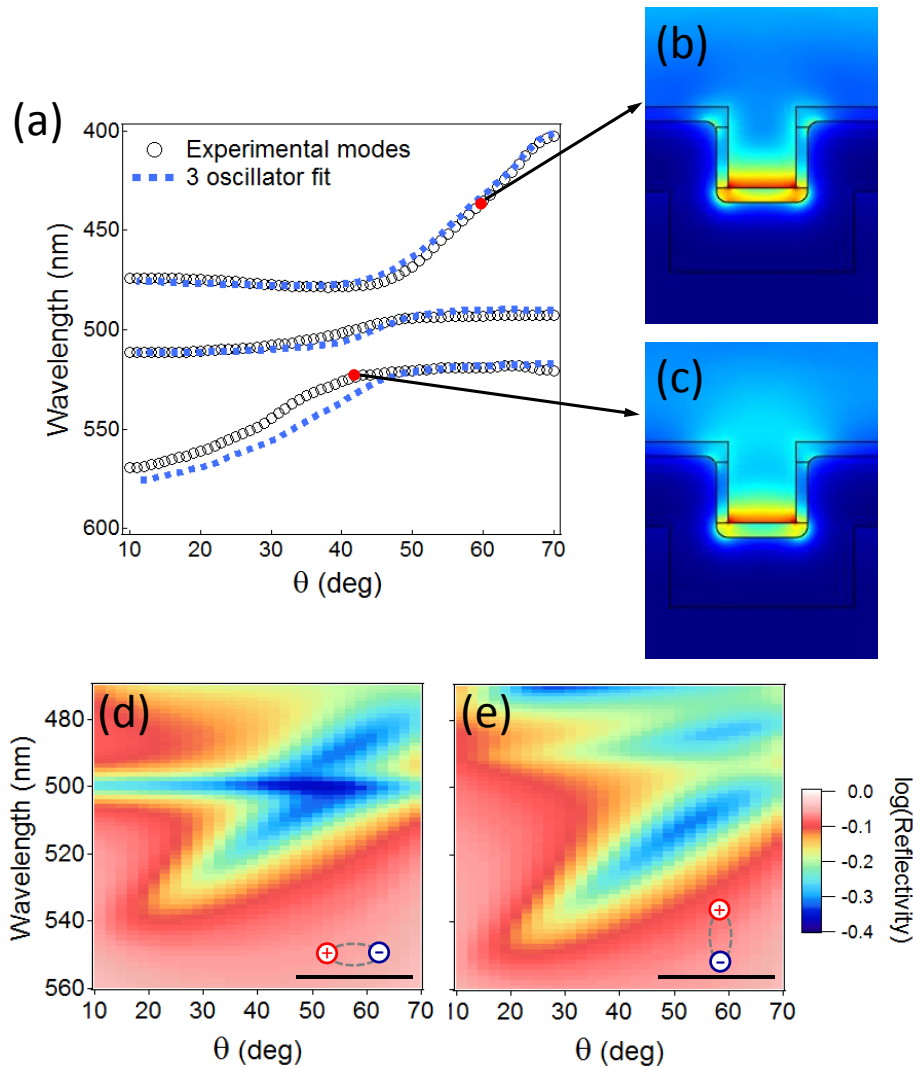


Fig. 7.18 (a) Extracted spectral mode positions for $\phi = 90^\circ$ reflection dips (open circles), and fit from three oscillator coupling model (dashed lines). (b,c) Time-averaged E -field intensity profiles ($\vec{E} \cdot \vec{E}$) as indicated. (d,e) Simulated reflection spectra for (d) in-plane and (e) out-of-plane exciton dipoles.

to maintain their optical quality. In contrast our 25 nm thick CHPI film is prepared directly on the metal, and still gives strongly radiative exciton modes because the organic sandwich protects the PbI QW layers. Theoretically Fig. 7.16(a) shows that excitons remain radiative via SPP coupling for film thickness above 10 nm. Hence the perovskite system is well suited to manipulate light-matter interactions. Such modification of the exciton and SPP states is of great interest for future optoelectronic devices, involving ultra-thin semiconductors including the layered van der Waals materials based on graphene and dichalcogenides.

Chapter 8

Conclusions and further work

Metal-halide based organic-inorganic perovskites are self-assembling semiconductors with many flexible and tunable properties. The exact structure formed depends on the stoichiometric mix of organic and inorganic constituents, and this thesis explored the optical behaviour of thin 2D perovskite samples. Lead iodide perovskites ($(\text{RNH}_3)_2\text{PbI}_4$) forms a layered structure with alternating inorganic $[\text{PbI}_6]$ octahedral networks and organic molecular sheets. Due to the difference in the band gaps of the organic and inorganic constituents a multiple quantum well structure is formed, so that excitons are created and trapped in the inorganic sheets. This reduction in dimensionality (quantum confinement), as well as the reduced refractive index of organic molecules (dielectric confinement), lead to large exciton binding energy. As such the optical properties of such perovskites are dominated by exciton effects even at room temperature. The tunability of the exciton energy via structural changes or external stimuli, as well as the many fabrication techniques available, make such materials promising candidates for use in future devices.

In Chapter 4 we looked at the fabrication of thin perovskite films by spin coating a solution of the perovskite constituents dissolved in a suitable solvent. The morphology of the thin films were strongly affected by the organic moiety of the perovskite, the substrate functionalisation and the atmosphere in which the spin coating took place. The thickness of the films was controlled by the spin speed and the initial solution concentration. We found we could reliably create thin films with thickness $\sim 30 - 150$ nm, uniform on μm lengthscales by spin coating in a dehydrated atmosphere and by functionalising the surface with an aminosilane.

In Chapter 5 we created ultra-thin samples of perovskites using exfoliation, and probed the optical effects of such samples. By changing the substrate to improve optical contrast we were able to view layers just a few monolayers thick microscopically. We were able to pro-

duce monolayer-thick perovskite samples, and found a layer thickness in CHPI of 1.6 nm. The optical spectra were dominated by the exciton and charge transfer between organic and inorganic layers, and we observed three main regimes of behaviour. For areas >27 nm (15 layers) we observed ‘bulk’ thin film behaviour, similar to spin coated films. A structural transition region was found between 15 – 25 nm, where flattening and straining of the inorganic layers led to a redshift and broadening of the exciton peak, with a corresponding redshift and increase in optical activity of the charge transfer. Finally for the thinnest samples (<15 nm, 8 layers), relaxation of the inorganic layers produce a blueshift and decrease in linewidth of the exciton peak.

In Chapter 6 we explored the interaction excitons with localised surface plasmons. Metal island structure were created via the evaporation of noble metals, both with and without templating, then coated with perovskite films. In Au nanostructures, where the plasmon is far off-resonance with the exciton, the perovskite coating caused a redshift and broadening of the localised surface plasmon. However for Ag islands the two oscillators were more in resonance, and thus we observed weak coupling with a ~ 5 nm blueshift of the exciton, as well as an increase in the extinction due to the field enhancement of the localised surface plasmon.

In Chapter 7 we investigated the coupling between excitons and modes on 1D gratings. Both plasmonic and non-plasmonic gratings were created, capable to sustaining a range of diffractive, surface plasmon polariton and localised modes. The energies and strengths of these modes were found to be sensitive to grating geometry, dielectric coatings and light polarisation, and we were able to create modes resonant with the exciton by change the periodicity and incident/azimuthal angle of light. We found no changes to the exciton except in the case of perovskite-coated Ag gratings. In this case we observed the appearance of a second exciton mode due, the image biexciton, formed as a result of the interaction between the exciton and its image in the metallic mirror, outcoupled via the exciton surface plasmon polariton. The binding energy of the image biexciton is 100 meV, and tunable via a change in the electric environment around the exciton, e. g. resonance with a surface plasmon polariton. We also observed strong coupling between the exciton, biexciton, and surface plasmon polariton mode on the grating, with Rabi splittings of 150 and 125 meV for the exciton and biexciton respectively. The out-of-plane image biexciton mediated coupling between perpendicular exciton and surface plasmon modes. Finite element method modelling showed that the surface plasmon mode was trapped in the bottom of the grating slits, and the field enhancement in the perovskite layer as a result enhanced the coupling strength and reduced the cavity length needed when compared to exciton-photon strong coupling. This Rabi

splitting in two orders of magnitude larger than what has been observed in inorganic GaAs quantum wells, and is observable even at room temperature.

Although the optical properties of 2D lead iodide perovskites are fairly well understood, fewer studies have focused on studying their transport activities. Although carrier can clearly be transported in the plane of the inorganic sheets, the structure of the electroluminescent devices [Fig. 2.20] suggests there may be some charge transfer between the organic and inorganic layers, the exact nature of which is not well understood. The transport properties of perovskites must be studied more in order to compare them to materials currently used in optoelectronic devices.

More fundamentally, the driving force behind the self-assembly of the perovskite structure is not known. Particularly important is the understanding of the crystal formation on a molecular level from a liquid phase, for example in spin coating. As a result the formation of layers over structured substrates, for example in the grating system, is not known. This layer orientation has great implications in the optical properties of the nanostructures in question. Better understanding would allow us to control and tailor the perovskite formation to suit the needs of the system.

References

- [1] M. Faraday, *Experimental Researches in Electricity, Volume 1* (Cambridge University Press, 2012).
- [2] A. Becquerel, Comptes Rendus de l'Académie des Sciences **9**, 711 (1839).
- [3] C. Fritts, American Journal of Science **26**, 465 (1883).
- [4] W. Smith, Nature **7**, 303 (1873).
- [5] W. Adams and R. Day, Proceedings of the Royal Society A **25**, 113 (1876).
- [6] H. Round, Electrical World **49**, 309 (1907).
- [7] A. Wilson, Proceedings of the Royal Society A **133**, 458 (1931).
- [8] <http://en.wikipedia.org/wiki/Transistor>.
- [9] http://www.greenrhinoenergy.com/solar/technologies/pv_manufacturing.php.
- [10] H. Naarmann, Ullmann's Encyclopedia of Industrial Chemistry **29**, 295 (2002).
- [11] H. Shirakawa, E. Louis, A. MacDiarmid, C. Chiang, and A. Heeger, Journal of the Chemical Society, Chemical Communications p. 578 (1977).
- [12] L. Miozzo, A. Yassar, and G. Horowitz, Journal of Materials Chemistry **20**, 2513 (2010).
- [13] <http://www.samsung.com/us/video/tvs/KN55S9CAFXZA>.
- [14] S. a. Vaganov, D. a. Zaitsev, and R. P. Seisyan, Technical Physics **58**, 1039 (2013).
- [15] P. Bassu, *Theory of optical processes in semiconductors: bulk and microstructures* (Oxford University Press, 1997).
- [16] H. C. H. N. H. P. Nanomaterial, T. Dammak, M. Koubaa, K. Boukhechda, H. Bougzhala, A. Mlayah, and Y. Abid, The Journal of Physical Chemistry C **113**, 19305 (2009).
- [17] R. Dingle, W. Wiegmann, and C. Henry, Physical Review Letters **33**, 827 (1974).
- [18] M. M. Lee, J. Teuscher, T. Miyasaka, T. N. Murakami, and H. J. Snaith, Science **338**, 643 (2012).

- [19] J. H. Heo, S. H. Im, J. H. Noh, T. N. Mandal, C. S. Lim, J. A. Chang, Y. H. Lee, H. J. Kim, A. Sarkar, M. K. Nazeeruddin, et al., *Nature Photonics* **7**, 486 (2013).
- [20] M. Liu, M. B. Johnston, and H. J. Snaith, *Nature* **501**, 395 (2013).
- [21] F. Hao, C. C. Stoumpos, D. H. Cao, R. P. H. Chang, and M. G. Kanatzidis, *Nature Photonics* **8**, 489 (2014).
- [22] A. Nagami, K. Okamura, and T. Ishihara, *Physica B: Condensed Matter* **227**, 346 (1996).
- [23] T. Fukumoto, M. Hirasawa, and T. Ishihara, *Journal of Luminescence* **87-89**, 497 (2000).
- [24] J.-i. Fujisawa and T. Ishihara, *Physical Review B* **70**, 113203 (2004).
- [25] K. Pradeesh, M. Agarwal, K. K. Rao, and G. V. Prakash, *Solid State Sciences* **12**, 95 (2010).
- [26] D. B. Mitzi, K. Chondroudis, and C. R. Kagan, *IBM Journal of Research and Development* **45**, 29 (2001).
- [27] T. Ishihara, *Journal of Luminescence* **60-61**, 269 (1994).
- [28] K. Pradeesh, J. J. Baumberg, and G. V. Prakash, *Optics express* **17**, 22171 (2009).
- [29] G. Mousdis, G. Papavassiliou, C. Raptopoulou, and A. Terzis, *Journal of Materials Chemistry* **10**, 515 (2000).
- [30] T. Ishihara, J. Takahashi, and T. Goto, *Solid State Communications* **69**, 933 (1989).
- [31] D. B. Mitzi, *Journal of the Chemical Society, Dalton Transactions* pp. 1–12 (2001).
- [32] <http://www.mrl.ucsb.edu/~dshoe/218/>.
- [33] D. G. Billing and A. Lemmerer, *CrystEngComm* **8**, 686 (2006).
- [34] D. G. Billing and A. Lemmerer, *New Journal of Chemistry* **32**, 1736 (2008).
- [35] S. Zhang, G. Lanty, J. S. Lauret, E. Deleporte, P. Audebert, and L. Galmiche, *Acta Materialia* **57**, 3301 (2009).
- [36] K. Teshima, M. Suzuki, Y. Shirai, M. Rikukawa, and K. Sanui, *Japanese Journal of Applied Physics* **42**, L698 (2003).
- [37] K. Kikuchi, Y. Takeoka, M. Rikukawa, and K. Sanui, *Colloids and Surfaces A: Physicochemical and Engineering Aspects* **257-258**, 199 (2005).
- [38] Y. Kawabata, M. Yoshizawa-Fujita, Y. Takeoka, and M. Rikukawa, *Synthetic Metals* **159**, 776 (2009).
- [39] J. Calabrese, N. L. Jones, R. L. Harlow, N. Herron, D. L. Thorn, and Y. Wang, *Journal of the American Chemical Society* **113**, 2328 (1991).

- [40] S. Barman, N. V. Venkataraman, S. Vasudevan, and R. Seshadri, *Journal of Physical Chemistry B* **107**, 1875 (2003).
- [41] T. Ishihara, J. Takahashi, and T. Goto, *Physical Review B* **42**, 11099 (1990).
- [42] C. Xu, S. Fukuta, T. Kondo, R. Ito, Y. Takahashi, K. Kumata, H. Sakakura, and S. Fukuta, *Solid State Communications* **77**, 923 (1991).
- [43] V. V. Naik and S. Vasudevan, *Journal of Physical Chemistry C* **4**, 4536 (2010).
- [44] K. Pradeesh, J. J. Baumberg, and G. V. Prakash, *Applied Physics Letters* **95**, 173305 (2009).
- [45] D. B. Mitzi, *Chemistry of Materials* **13**, 3283 (2001).
- [46] N. Kitazawa, *Japanese Journal of Applied Physics* **35**, 6202 (1996).
- [47] Z. Tang, J. Guan, and A. M. Guloy, *Journal of Materials Chemistry* **293**, 479 (2001).
- [48] Z. Cheng and J. Lin, *CrystEngComm* **12**, 2646 (2010).
- [49] X. Hong, T. Ishihara, and A. V. Nurmikko, *Solid state communications* **84**, 657 (1992).
- [50] Z. Cheng, H. Wang, Z. Quan, C. Lin, J. Lin, and Y. Han, *Journal of Crystal Growth* **285**, 352 (2005).
- [51] P. Audebert, G. Clavier, V. Alain-Rizzo, E. Deleporte, S. Zhang, J. J.-S. S. Lauret, G. Lanty, and C. Boissiere, *Chemistry of Materials* **21**, 210 (2009).
- [52] M. Era and S. Oka, *Thin Solid Films* **376**, 232 (2000).
- [53] K. Liang, D. D. B. D. Mitzi, and M. M. M. T. Prikas, *Chemistry of Materials* **4756**, 403 (1998).
- [54] K. Pradeesh, J. J. Baumberg, G. Vijaya Prakash, and G. V. Prakash, *Applied Physics Letters* **95**, 173305 (2009).
- [55] T. Matsui, A. Yamaguchi, Y. Takeoka, M. Rikukawa, and K. Sanui, *Chemical Communications* **3**, 1094 (2002).
- [56] M. Era and K. Maeda, *Thin Solid Films* **331**, 285 (1998).
- [57] S. Ahmad and P. Kanaujia, *ACS Applied Materials & Interfaces* (2014).
- [58] M. Era and T. Hattori, *Chemistry of Materials* **9**, 8 (1997).
- [59] D. B. Mitzi, M. T. Prikas, and K. Chondroudis, *Chemistry of Materials* **11**, 542 (1999).
- [60] K. Chondroudis, D. B. Mitzi, and P. Brock, *Chemistry of Materials* **12**, 169 (2000).
- [61] T. Kataoka, T. Kondo, R. Ito, S. Sasaki, K. Uchida, and N. Miura, *Physica B* **201**, 423 (1994).

- [62] G. Vijaya Prakash, K. Pradeesh, R. Ratnani, K. Saraswat, M. E. Light, and J. J. Baumberg, *Journal of Physics D: Applied Physics* **42**, 185405 (2009).
- [63] T. Kataoka, T. Kondo, and R. Ito, *Physical Review B* **47**, 2010 (1993).
- [64] N. Kitazawa, *Journal of Materials Science* **3**, 5 (1998).
- [65] Y. Wei, P. Audebert, L. Galmiche, J.-S. Lauret, and E. Deleporte, *Materials* **7**, 4789 (2014).
- [66] N. Kitazawa and Y. Watanabe, *Journal of Materials Science* **37**, 4845 (2002).
- [67] Z. Y. Cheng, Z. Wang, R. B. Xing, Y. C. Han, and J. Lin, *Chemical Physics Letters* **376**, 481 (2003).
- [68] T. Umebayashi, K. Asai, T. Kondo, and A. Nakao, *Physical Review B* **67**, 2 (2003).
- [69] K. Matsuishi, T. Ishihara, S. Onari, Y. H. Chang, and C. H. Park, *Physica Status Solidi (B)* **241**, 3328 (2004).
- [70] T. Kondo, M. Mizuno, S. Iwamoto, S. Hayase, K. Tanaka, J. Ishi, K. Ema, and R. Ito, *Solid State Communications* **105**, 503 (1998).
- [71] T. Goto, N. Ohshima, G. A. Mousdis, and G. C. Papavassiliou, *Solid State Communications* **117**, 13 (2001).
- [72] C. Xu, H. Sakakura, T. Kondo, S. Takeyama, N. Miura, Y. Takahashi, K. Kumata, and R. Ito, *Solid State Communications* **79**, 249 (1991).
- [73] K. Tanaka, F. Sano, T. Takahashi, T. Kondo, R. Ito, and K. Ema, *Solid State Communications* **122**, 249 (2002).
- [74] N. Kitazawa, *Materials Science and Engineering B* **49**, 233 (1997).
- [75] S. Ahmad, J. J. Baumberg, and G. Vijaya Prakash, *Journal of Applied Physics* **114**, 233511 (2013).
- [76] T. Kondo, T. Azuma, T. Yuasa, and R. Ito, *Solid State Communications* **105**, 253 (1998).
- [77] M. Shimizu, J.-i. Fujisawa, and T. Ishihara, *Physical Review B* **74** (2006).
- [78] T. Ishihara, X. Hong, J. Ding, and A. Nurmikko, *Surface Science* **267**, 323 (1992).
- [79] M. Hirasawa, T. Ishihara, and T. Goto, *Journal of the Physical Society of Japan* **63**, 3870 (1994).
- [80] M. Shinada and S. Sugano, *Journal of the Physical Society of Japan* **21**, 1936 (1966).
- [81] M. Kumagai and T. Takagahara, *Physical Review B* **40**, 12359 (1989).
- [82] E. Muljarov, S. Tikhodeev, and N. Gippius, *Physical Review B* **51**, 14370 (1995).

- [83] S. Sourisseau, N. Louvain, W. Bi, N. Mercier, D. Rondeau, F. Boucher, J.-Y. Buzaré, and C. Legein, *Chemistry of Materials* **19**, 600 (2007).
- [84] J. L. Knutson, J. D. Martin, and D. B. Mitzi, *Inorganic chemistry* **44**, 4699 (2005).
- [85] K. Matsuishi, T. Suzuki, S. Onari, E. Gregortanz, R. J. Hemley, and H. K. Mao, *Physica Status Solidi (B)* **223**, 177 (2001).
- [86] N. Mercier, S. Poiroux, A. Riou, and P. Batail, *Inorganic chemistry* **43**, 8361 (2004).
- [87] D. B. Mitzi, K. Chondroudis, and C. R. Kagan, *Inorganic chemistry* **38**, 6246 (1999).
- [88] M. Braun, *Chemical Physics Letters* **303**, 157 (1999).
- [89] J. Kasprzak, M. Richard, S. Kundermann, a. Baas, P. Jeambrun, J. M. J. Keeling, F. M. Marchetti, M. H. Szymańska, R. André, J. L. Staehli, et al., *Nature* **443**, 409 (2006).
- [90] S. Christopoulos, G. von Högersthal, a. Grundy, P. Lagoudakis, a. Kavokin, J. Baumberg, G. Christmann, R. Butté, E. Feltin, J.-F. Carlin, et al., *Physical Review Letters* **98**, 126405 (2007).
- [91] a. Amo, T. C. H. Liew, C. Adrados, R. Houdré, E. Giacobino, a. V. Kavokin, and a. Bramati, *Nature Photonics* **4**, 361 (2010).
- [92] T. Fujita, Y. Sato, T. Kuitani, and T. Ishihara, *Physical Review B* **57**, 12428 (1998).
- [93] G. Lanty, A. Bréhier, R. Parashkov, J. S. Lauret, and E. Deleporte, *New Journal of Physics* **10**, 065007 (2008).
- [94] T. Fujita and T. Ishihara, *Journal of the Physics Society Japan* **68**, 2918 (1999).
- [95] T. Fujita and H. Nakashima, *Physica Status Solidi (B)* **147**, 147 (2000).
- [96] J. Ishi-Hayase and T. Ishihara, *Semiconductor Science and Technology* **18**, S411 (2003).
- [97] A. Brehier, R. Parashkov, J. S. Lauret, and E. Deleporte, *Applied Physics Letters* **89**, 171110 (2006).
- [98] K. Sumioka, H. Nagahama, and T. Tsutsui, *Applied Physics Letters* **78**, 1328 (2001).
- [99] M. Era, S. Morimoto, T. Tsutsui, and S. Saito, *Applied Physics Letters* **65**, 676 (1994).
- [100] T. Matsushima, K. Fujita, and T. Tsutsui, *Japanese Journal of Applied Physics* **44**, 1457 (2005).
- [101] T. Hattori, T. Taira, M. Era, T. Tsutsui, and S. Saito, *Chemical Physics Letters* **254**, 103 (1996).
- [102] D. B. Mitzi, C. Feild, W. T. A. Harrison, A. Guloy, C. A. Felid, and M. Guloy, A, *Nature* **369**, 467 (1994).

- [103] D. Mitzi, C. Dimitrakopoulos, and L. Kosbar, *Device Research* **467**, 185 (2002).
- [104] D. B. Mitzi, C. D. Dimitrakopoulos, and L. L. Kosbar, *Chemistry of Materials* **13**, 3728 (2001).
- [105] C. R. Kagan, *Science* **286**, 945 (1999).
- [106] K. Shibuya, M. Koshimizu, Y. Takeoka, and K. Asai, *Nuclear Instruments and Methods in Physics Research B* **194**, 207 (2002).
- [107] S. Kengo, K. Masanori, S. Hiromi, and A. Keisuke, *Proceedings of IEEE Sensors* **1**, 552 (2002).
- [108] K. Shibuya, M. Koshimizu, H. Murakami, Y. Muroya, Y. Katsumura, and K. Asai, *Japanese Journal of Applied Physics* **43**, L1333 (2004).
- [109] E. J. Zeman and G. C. Schatz, *Journal of Physical Chemistry* **91**, 634 (1987).
- [110] S. Maier, *Plasmonics: Fundamentals and Applications* (Springer, 2007), 2007th ed.
- [111] Y. Chen, E. Koteles, R. Seymour, G. Sonek, J. Ballantyne, and J. Ballantyne, *Solid State Communications* **46**, 95 (1983).
- [112] R. Wood, *Proceedings of the Physical Society* **18**, 396 (1902).
- [113] M. Hutley, *Diffraction gratings* (Academic Press Inc. Ltd., 1982).
- [114] E. Loewen and E. Popov, *Diffraction gratings and applications* (Marcel Dekker, Inc., 1997).
- [115] U. Fano, *Journal of the Optical Society of America* **31**, 213 (1941).
- [116] A. Hessel and A. Oliner, *Applied Optics* **4**, 1275 (1965).
- [117] K. Lee and Q.-H. Park, *Physical Review Letters* **95**, 103902 (2005).
- [118] H. Lochbihler, *Physical Review B* **50**, 4795 (1994).
- [119] R. Ritchie, E. Arakawa, J. Cowan, and R. Hamm, *Physical Review Letters* **21**, 1530 (1968).
- [120] M. Treacy, *Physical Review B* **66**, 195105 (2002).
- [121] R. Watts, T. Preist, and J. Sambles, *Physical Review Letters* **79**, 3978 (1997).
- [122] M. Hutley and D. Maystre, *Optics Communications* **19**, 431 (1976).
- [123] J. Jackson, *Classical electrodynamics* (Wiley, 1999), 3rd ed.
- [124] S. Bozhevolnyi, V. Volkov, E. Devaux, and T. Ebbesen, *Physical Review Letters* **95**, 1 (2005).
- [125] T. Srivastava and A. Kumar, *Journal of Applied Physics* **106**, 043104 (2009).

- [126] S. Chattopadhyay and P. K. Saha, ISRN Optics **2012**, 1 (2012).
- [127] I. Novikov and A. Maradudin, Physical Review B **66**, 1 (2002).
- [128] M. Kuttge, F. J. G. de Abajo, and A. Polman, Optics Express **17**, 10385 (2009).
- [129] W. Rechberger, a. Hohenau, a. Leitner, J. Krenn, B. Lamprecht, and F. Aussenegg, Optics Communications **220**, 137 (2003).
- [130] B. Wiley, S. Im, and Z. Li, The Journal of Physical Chemistry B **110**, 15666 (2006).
- [131] B. J. Wiley, Y. Chen, J. M. McLellan, Y. Xiong, Z.-Y. Li, D. Ginger, and Y. Xia, Nano Letters **7**, 1032 (2007).
- [132] H. Chen, L. Shao, Q. Li, and J. Wang, Chemical Society Reviews **42**, 2679 (2013).
- [133] D. Meyerhofer, Journal of Applied Physics **49**, 3993 (1978).
- [134] R. van Hardeveld, P. Gunter, L. van IJzendoorn, W. Wieldraaijer, E. Kuipers, and J. Niemantsverdriet, Applied Surface Science **84**, 339 (1995).
- [135] C. J. Lawrence, Physics of Fluids **31**, 2786 (1988).
- [136] D. P. Birnie, S. K. Hau, D. S. Kamber, and D. M. Kaz, Journal of Materials Science: Materials in Electronics **16**, 715 (2005).
- [137] *Cleaning mechanisms*, URL <http://www.co2clean.com/clnmech.htm>.
- [138] K. S. Novoselov, A. K. Geim, S. V. Morozov, D. Jiang, Y. Zhang, S. V. Dubonos, I. V. Grigorieva, and A. A. Firsov, Science **306**, 666 (2004).
- [139] P. Blake, E. W. Hill, A. H. Castro Neto, K. S. Novoselov, D. Jiang, R. Yang, T. J. Booth, and A. K. Geim, Applied Physics Letters **91**, 063124 (2007).
- [140] Z. H. Ni, H. M. Wang, J. Kasim, H. M. Fan, T. Yu, Y. H. Wu, Y. P. Feng, and Z. X. Shen, Nano letters **7**, 2758 (2007).
- [141] A. Splendiani, L. Sun, Y. Zhang, T. Li, J. Kim, C. Y. Chim, G. Galli, and F. Wang, Nano Letters **10**, 1271 (2010).
- [142] A. Castellanos-Gomez, N. Agrait, and G. Rubio-Bollinger, Applied Physics Letters **96**, 213116 (2010).
- [143] P. Tonndorf, R. Schmidt, P. Bottger, X. Zhang, J. Borner, A. Liebig, M. Albrecht, C. Kloc, O. Gordan, D. Zahn, et al., Optics Express **21**, 4908 (2013).
- [144] I. Saikumar, S. Ahmad, J. J. Baumberg, and G. Vijaya Prakash, Scripta Materialia **67**, 834 (2012).
- [145] D. G. Billing and A. Lemmerer, Acta crystallographica. Section C, Crystal structure communications **62**, m269 (2006).
- [146] M. Born and E. Wolf, *Principles of Optics: Electromagnetic theory of propagation, interference and diffraction of light* (Cambridge University Press, 1999), 7th ed.

- [147] J.-i. Fujisawa and N. Tajima, *Physical Review B* **72**, 125201 (2005).
- [148] J.-i. Fujisawa, N. Tajima, K. Tamaki, M. Shimomura, and T. Ishihara, *Journal of Physical Chemistry C* **111**, 1146 (2007).
- [149] S. Zhang, P. Audebert, Y. Wei, A. Al Choueiry, G. Lanty, A. Bréhier, L. Galmiche, G. Clavier, C. Boissière, J.-S. S. Lauret, et al., *Materials* **3**, 3385 (2010).
- [150] S. Baranovskii, U. Doerr, and P. Thomas, *Physical Review B* **48**, 17149 (1993).
- [151] L. Andreani and G. Panzarini, *Physical Review B* **57**, 4670 (1998).
- [152] I. Kuznetsova, N. Gogh, J. Förstner, T. Meier, S. T. Cundiff, I. Varga, and P. Thomas, *Physical Review B* **81**, 075307 (2010).
- [153] T. Iwasaki, T. Goto, and Y. Nishina, *Physica Status Solidi (B)* **88**, 289 (1978).
- [154] T. Goto and J. Maeda, *Journal of the Physical Society of Japan* **56**, 3710 (1987).
- [155] T. Jensen, M. Malinsky, C. Haynes, and R. Van Duyne, *The Journal of Physical Chemistry B* **104**, 10549 (2000).
- [156] G. Xu, M. Tazawa, P. Jin, and S. Nakao, *Applied Physics A* **80**, 1535 (2004).
- [157] M. Malinsky, K. Kelly, G. Schatz, and R. Van Duyne, *The Journal of Physical Chemistry B* **105**, 2343 (2001).
- [158] P. Royer, J. Goudonnet, R. Warmack, and T. Ferrell, *Physical Review B* **35**, 3753 (1987).
- [159] N. Cade, T. Ritman-Meer, and D. Richards, *Physical Review B* **79**, 241404 (2009).
- [160] L. G. Olson, Y. S. Lo, T. P. Beebe, and J. M. Harris, *Analytical chemistry* **73**, 4268 (2001).
- [161] C. E. Talley, J. B. Jackson, C. Oubre, N. K. Grady, C. W. Hollars, S. M. Lane, T. R. Huser, P. Nordlander, and N. J. Halas, *Nano letters* **5**, 1569 (2005).
- [162] R. Toftegaard, J. Arnbjerg, H. Cong, H. Agheli, D. S. Sutherland, and P. R. Ogilby, *Pure and Applied Chemistry* **83**, 885 (2011).
- [163] C.-Y. Cho, M.-K. Kwon, S.-J. Lee, S.-H. Han, J.-W. Kang, S.-E. Kang, D.-Y. Lee, and S.-J. Park, *Nanotechnology* **21**, 205201 (2010).
- [164] V. Reboud, G. Lévêque, M. Striccoli, T. Placido, a. Panniello, M. L. Curri, J. a. Alducin, T. Kehoe, N. Kehagias, D. Mecerreyes, et al., *Nanoscale* **5**, 239 (2013).
- [165] L. Blanco and F. García de Abajo, *Journal of Quantitative Spectroscopy and Radiative Transfer* **89**, 37 (2004).
- [166] N. Kaiser, *Applied optics* **41**, 3053 (2002).
- [167] H. Walter, G. Bauer, R. Domnick, G. Jakopic, and A. Leitner, *Optical Engineering* **45**, 103801 (2006).

- [168] R. S. Sennett and G. D. Scott, *Journal of the Optical Society of America* **40**, 203 (1950).
- [169] R. Gupta, M. J. Dyer, and W. a. Weimer, *Journal of Applied Physics* **92**, 5264 (2002).
- [170] P. Gadenne and J. C. Rivoal, *Topics in Applied Physics* **82**, 185 (2002).
- [171] M. M. Lee, P. P. Dobson, and B. Cantor, *Thin Solid Films* **219**, 199 (1992).
- [172] S. Yamaguchi, *Journal of the Physical Society of Japan* **15**, 1577 (1960).
- [173] T. Yamaguchi, S. Yoshida, and A. Kinbara, *Thin Solid Films* **13**, 261 (1972).
- [174] T. Yamaguchi, S. Yoshida, and A. Kinbara, *Thin Solid Films* **18**, 63 (1973).
- [175] R. H. Doremus, *Journal of Applied Physics* **37**, 2775 (1966).
- [176] C. Haynes and R. V. Duyne, *The Journal of Physical Chemistry B* **105**, 5599 (2001).
- [177] J. Hulteen and R. V. Duyne, *Journal of Vacuum Science & Technology A* **13**, 1553 (1995).
- [178] J. C. Hulteen, D. a. Treichel, M. T. Smith, M. L. Duval, T. R. Jensen, and R. P. Van Duyne, *The Journal of Physical Chemistry B* **103**, 3854 (1999).
- [179] C. L. Haynes, A. D. McFarland, M. T. Smith, J. C. Hulteen, and R. P. Van Duyne, *The Journal of Physical Chemistry B* **106**, 1898 (2002).
- [180] T. Jensen, G. Schatz, and R. Van Duyne, *The Journal of Physical Chemistry B* **103**, 2394 (1999).
- [181] N. Alemu and F. Chen, *Physica Status Solidi (a)* **211**, 213 (2014).
- [182] Y. Zheng, B. Kiraly, and S. Cheunkar, *Nano Letters* **11**, 2061 (2011).
- [183] Q. Xu, F. Liu, Y. Liu, K. Cui, X. Feng, W. Zhang, and Y. Huang, *Scientific Reportse-ports* **3**, 2112 (2013).
- [184] P. Spinelli and A. Polman, *Optics Express* **20**, 205 (2012).
- [185] R. French, J. Rodríguez-Parada, M. Yang, R. Derryberry, and N. Pfeiffenberger, *Solar Energy Materials and Solar Cells* **95**, 2077 (2011).
- [186] H. Morawitz, *Physical Review* **187**, 1792 (1969).
- [187] H. Morawitz and M. Philpott, *Physical Review B* **10**, 4863 (1974).
- [188] R. R. Chance, A. Prock, and R. Silbey, *The Journal of Chemical Physics* **60**, 2184 (1974).
- [189] R. R. Chance, A. Prock, and R. Silbey, *Physical Review A* **12**, 1448 (1975).
- [190] R. R. Chance, A. Prock, and R. Silbey, *The Journal of Chemical Physics* **62**, 2245 (1975).

- [191] G. Ford and W. Weber, Physics Reports **113**, 195 (1984).
- [192] J. Frischeisen, Q. Niu, A. Abdellah, J. B. Kinzel, R. Gehlhaar, G. Scarpa, C. Adachi, P. Lugli, and W. Brütting, Optics Express **S1**, A7 (19).
- [193] A. Kumar, R. Srivastava, P. Tyagi, D. Mehta, and M. Kamalasan, Organic Electronics **13**, 159 (2012).
- [194] R. Tamaki, Y. Arai, D. Ichikawa, M. Inoue, H. Kunugita, and K. Ema, Journal of Luminescence **128**, 842 (2008).
- [195] J. Baumberg, a. Heberle, a. Kavokin, M. Vladimirova, and K. Köhler, Physical Review Letters **80**, 3567 (1998).
- [196] A. Kavokin and J. Baumberg, Physical Review B **57**, 12697 (1998).
- [197] M. Vladimirova, E. Ivchenko, and A. Kavokin, Semiconductors **32**, 90 (1998).
- [198] P. Vasa, R. Pomraenke, G. Cirmi, E. De Re, W. Wang, S. Schwieger, D. Leipold, E. Runge, G. Cerullo, and C. Lienau, ACS Nano **4**, 7559 (2010).
- [199] P. Vasa, R. Pomraenke, S. Schwieger, Y. Y. I. Mazur, V. Kunets, P. Srinivasan, E. Johnson, J. Kihm, D. Kim, E. Runge, et al., Physical Review Letters **101**, 116801 (2008).